



UNIVERSITAT
POLITÈCNICA
DE VALÈNCIA

Universitat Politècnica València

Departamento de comunicaciones

Development of new photonic devices based on barium titanate in silicon

Pau Casterà Molada

Supervisors: Dr. Pablo Sanchis Kilders

Dr. Ana María Gutiérrez Campo

Tesis presentada para la obtención del grado de Doctor en Telecomunicaciones de la Universitat Politècnica de València.

Thesis submitted to the Universitat Politècnica de València in partial fulfillment of the requirements for the degree of Doctor of Philosophy in Telecommunications engineering.

April 2017

Al meu avi Gaspar

Acknowledgements

First and foremost, I would like to start this section by acknowledging my supervisors. Thank you Pablo, for your extraordinary guidance and your exquisite treatment. It has been more than 4 years since I contacted you to be my MSc thesis supervisor and I am still grateful for taking the wisest decision in my academic and professional life so far. I literally cannot express all my gratitude for all these years, so I hope the work done during this thesis helps. Thank you Ana, for everything. Since the beginnings aligning in butt-coupling until characterizing eye diagrams; since the simplest simulation work until the most complicate 3Dmax figure. Thank you for helping me in any problem, revising all my work and thank you for spending your time in showing me everything I was capable of and making me a better version of myself. I am beyond grateful. And above everything, thank you for your friendship.

I would also like to thank the director of NTC for allowing me to realize my thesis there. Special thanks to the fabrication team: Amadeu, Dora, Laurent and Juan. Thank you for all your work, constant feedback, your help and interest. Thanks to Jose Ayúcar for all SEM images and for all his time. Thank you David Zurita for the labview programs, for your helping hand and for the good atmosphere in the never-ending days at the lab. Thank you Antoine for always being ready to help in everything I needed with a smile on your face and thanks to Domenico for the COMSOL files at the beginning.

Another key point of this thesis has been all friends in the open room. Specially, I would like to thank Álvaro and Luis, with whom I have more closely worked during these 3 years. Together we formed the *pabsanki* team, and whether you needed a helping hand, a moment to talk or relax, you have always been there offering your support. I am really proud of you. I would also like to thank my Italians Marghe and Raffaele for all good moments we shared and for those still to come. Thank you for always being there.

Outside of the workplace, I am incredibly grateful for my family. I want to thank my mother for being the cornerstone of our small family, for her extraordinary heart, and for breaking her back to provide me the best affective, cultural and economic environment to reach further. Special thanks to my sisters for being an example to me.

I would also like to thank my beloved Monika for being the best partner in life I could have ever imagined. You make me want to be a better person.

Resumen

La integración de funcionalidades ópticas con alto rendimiento llevará a un gran desarrollo en el campo de la nanofotónica para un amplio abanico de aplicaciones. Actualmente, la fotónica de silicio es la tecnología líder para la implementación de dispositivos fotónicos integrados a bajo coste. El gran potencial de esta tecnología reside en su compatibilidad con las maduras técnicas de fabricación de circuitos integrados de silicio basadas en los procesos “complementary metal-oxide semiconductor” (CMOS) ampliamente utilizados en la industria microelectrónica y la disponibilidad de disponer de obleas de silicio sobre aislante de alta calidad, una plataforma ideal para crear circuitos de guía de ondas planas que ofrecen un fuerte confinamiento óptico debido al alto contraste índices entre el silicio ($n=3,45$) y el dióxido de silicio ($n=1,45$). Para poder mejorar el rendimiento de dispositivos fotónicos en silicio, la integración de materiales con propiedades excepcionales y compatibles con los procesos de fabricación CMOS surge como una excelente oportunidad para superar las actuales limitaciones de la tecnología de silicio al mismo tiempo que ofrece oportunidades novedosas y sin precedentes en la plataforma de silicio. En este sentido, el material titanato de bario (BaTiO_3) se postula como uno de los candidatos más prometedores. El trabajo desarrollado en esta tesis está esencialmente enfocado en el diseño, fabricación y caracterización de un modulador electro-óptico basado en una estructura híbrida de BaTiO_3 en silicio para la implementación de funcionalidades electro-ópticas de alto rendimiento más allá del estado del arte de las que no se puede disponer actualmente en la tecnología de fotónica de silicio.

Resum

La integració de funcionalitats òptiques amb alt rendiment portarà a un gran desenvolupament en el camp de la nanofotònica per a un ampli ventall d'aplicacions. Actualment, la fotònica de silici és la tecnologia capdavantera per a la implementació de dispositius fotònics integrats a baix cost. El gran potencial d'aquesta tecnologia resideix en la seva compatibilitat amb les madures tècniques de fabricació de circuits integrats de silici basades en els processos “complementary metal-oxide semiconductor” (CMOS) amplament utilitzats en la indústria microelectrònica i la disponibilitat de disposar d'hòsties de silici sobre aïllant d'alta qualitat, una plataforma ideal per crear circuits de guia d'ones planes que ofereixen un fort confinament òptic a causa de l'alt contrast d'índexs entre el silici ($n=3,45$) i el diòxid de silici ($n=1,45$). Per poder millorar el rendiment de dispositius fotònics en silici, la integració de materials amb propietats excepcionals i compatibles amb els processos de fabricació CMOS sorgeix com una excel·lent oportunitat per superar les actuals limitacions de la tecnologia de silici al mateix temps que ofereix oportunitats noves i sense precedents en la plataforma de silici. En aquest sentit, el material titanat de bari (BaTiO_3) es postula com un dels candidats més prometedors. El treball desenvolupat en aquesta tesi està essencialment enfocat en el disseny, fabricació i caracterització d'un modulador electro-òptic basat en una estructura híbrida de BaTiO_3 en silici per a la implementació de funcionalitats electro-òptiques d'alt rendiment més enllà de l'estat de l'art de les quals no es pot disposar actualment a la tecnologia de fotònica de silici.

Abstract

Integration of complex optical functionalities with high performance will lead to a huge development in the field of nanophotonics for a broad range of applications. Silicon photonics is currently the leading technology for the implementation of low-cost photonic integrated devices. The great potential of this technology relies on its compatibility with the mature silicon integrated circuits manufacturing based on complementary metal-oxide semiconductor (CMOS) processes widely used in microelectronic industry and the availability of high quality silicon-on-insulator wafers, an ideal platform for creating planar waveguide circuits that offers strong optical confinement due to the high index contrast between silicon ($n=3.45$) and silicon dioxide ($n=1.45$). In order to keep improving the performance of photonic devices on silicon, the integration of CMOS compatible materials with unique properties shows up as an excellent opportunity to overcome the current limitations in silicon while offering unprecedented and novel capabilities to the silicon platform. In this way, barium titanate (BaTiO_3) stands out as one of the most disruptive candidates. The work developed in this thesis is essentially focused on the design, fabrication and characterization of an electro-optic modulator based on a hybrid BaTiO_3 on silicon structure for the implementation of high performance electro-optic functionalities with beyond state-of-the art performance that currently cannot be afforded in silicon photonics technology.

Contents

Acknowledgements	
Resumen	i
Resum	iii
Abstract	v
Contents.....	vii
1. Introduction	1
1.1. Silicon photonics	1
1.2. Electro-optic modulation in silicon	5
1.2.1. Optical modulators	5
1.2.2. Different mechanisms for electro-optic modulation in silicon.....	6
1.2.3. Structures for modulation.....	8
1.2.3.1. MZIs.....	8
1.2.3.2. Ring resonators	9
1.2.3.3. Amplitude modulation principle	10
1.3. Barium titanate	11
1.3.1. Ferroelectricity and domain structure	11
1.3.2. Anisotropy	13
1.3.3. Pockels effect	14
1.3.4. Barium titanate on SOI.....	15
1.3.5. State-of-the-art of BTO based modulators	16
1.4. Objectives and outline of the thesis.....	18
2. Design of electro-optic modulators based on BTO in silicon.....	21
2.1. Optical design.....	21
2.1.1. Slot waveguide structure	21
2.1.2. Design of the slot waveguide.....	22
2.1.2.1. Fully etched waveguide	23
2.1.2.2. Half etched waveguide.....	26
2.1.2.3. Final waveguide structure	28
2.2. Electro-optical design.....	29
2.2.1. Electrode design in DC regime.....	29
2.2.2. Influence of BaTiO ₃ ferroelectric orientation.....	30
2.2.2.1. EO performance for a-axis oriented BaTiO ₃	30

2.2.2.2. EO performance for c-axis oriented BaTiO ₃	34
2.2.3. Influence of multi-domain BaTiO ₃ structure.....	37
2.3. RF design.....	41
3. Fabrication and characterization of electro-optic modulators based on BTO in silicon.....	45
3.1. General approach to develop photonics structures.....	45
3.2. BTO fabrication techniques.....	46
3.2.1. RF sputtering	47
3.2.2. Molecular Beam Epitaxy	47
3.3. Low loss amorphous silicon	48
3.4. Fabrication of BTO based modulators	53
3.5. Electrode fabrication process	55
3.6. Optical characterization.....	56
3.6.1. Fabricated devices	57
3.6.2. Experimental set-up.....	57
3.6.3. Samples with RF sputtered BTO	58
3.6.4. Sample with MBE BTO	69
3.7. Electro-optical characterization.....	70
3.7.1. DC regime	71
3.7.1.1. Experimental set-up	71
3.7.1.2. DC electro-optic results	71
3.7.2. RF regime	82
3.7.2.1. Experimental set-ups.....	82
3.7.2.2. RF electro-optic analogic results.....	84
3.7.2.3. RF electro-optic digital results	88
4. Conclusions and future outlook.....	91
List of publications	95
Bibliography.....	99

Chapter 1

Introduction

1.1. Silicon photonics

Photonics involves the use of optics, fibre-optics, lasers and electro-optical (EO) devices in numerous and diverse fields of technology for generating, amplifying, transmitting, modulating and detecting light. Its increasing importance in modern technology has indeed been determined by the invention of the laser, the introduction of semiconductor optical devices and the fabrication of low-loss optical fibres. It thus builds heavily on optical technology but reflects the growing tie between optics and electronics forged by the increasing role that semiconductor materials and devices play in optical systems. It supplements electronics in the form of optoelectronics and exhibits a strong market growth, which is expected to continue for the upcoming future.

The enormous importance of photonics is emphasized by the significant number of Nobel Prizes awarded in recent years:

- 2009: Nobel Prize in Physics to Charles Kuen Kao “for ground-breaking achievements concerning the transmission of light in fibres for optical communication” and to Willard S. Boyle and George E. Smith “for the invention of an imaging semiconductor circuit – the CCD sensor”
- 2010: Nobel Prize in Physics to Andre Geim and Konstantin Novoselov “for ground-breaking experiments regarding the two-dimensional material graphene” (with interesting implications in photonics)
- 2012: Nobel Prize in Physics to Serge Haroche and David J. Wineland “for ground-breaking experimental methods that enable measuring and manipulation of individual quantum systems”

Chapter 1: Introduction

- 2014: Nobel Prize in Chemistry awarded to Eric Betzig, Stefan W. Hell and William E. Moerner “for the development of super-resolved fluorescence microscopy”
- 2014: Nobel Prize in Physics awarded to Isamu Akasaki, Hiroshi Amano and Shuji Nakamura “for the invention of efficient blue light-emitting diodes which has enabled bright and energy-saving white light sources”

Photonics has also achieved a deep penetration in areas like Information and Communication Technologies (ICTs), health care and life sciences, sensing, defence and space technology. Especially the ICTs is witnessing a development speed without equal in the history of humankind. Internet traffic grows at a high level every year and therefore traffic demands [1]. Hence, there is need to search for different ways to carry data in a more efficient way. Using light beams to replace cables in all long distance communication has dominated during last years.

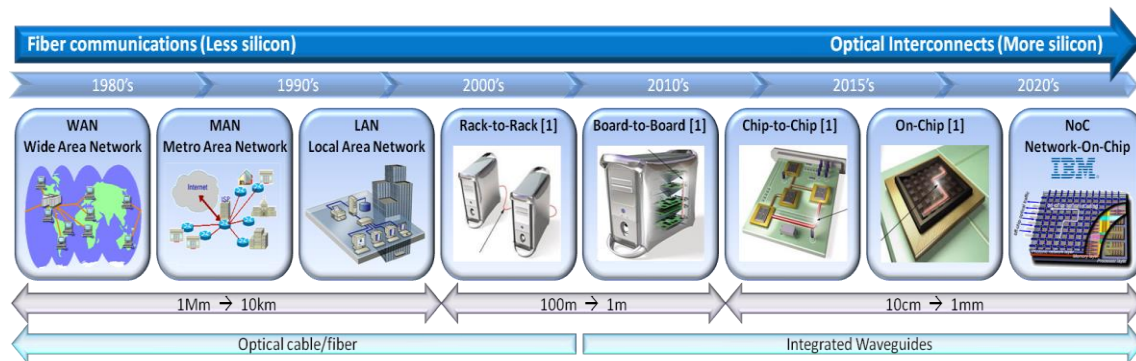


Figure 1.1: Trend from optical fibre communications to optical interconnect computing.

However, nowadays the general trend goes from optical fibre communications (long distances) to optical interconnect computing (very short distances), an evolution shown in Figure 1.1; and silicon photonics seems to be the most effective technology for such purpose. In this way, nanophotonic Integrated Circuits (ICs) have the potential to replicate the microelectronic revolution of the past decades. While there are several existing technologies to design and build networks and systems, the introduction of a viable photonic IC technology capable of creating a broad range of optical functions out of a single fabrication process is the fundamental breakthrough required to reduce costs dramatically.

Silicon photonics is currently the leading technology for enabling automated and low-cost volume manufacturing of highly integrated and complex photonic circuits. The main arguments in favour of this technology is its compatibility with CMOS (Complementary Metal Oxide Semiconductor) fabrication already used in microelectronic industry and the availability of high quality Silicon-On-Insulator (SOI) wafers, an ideal platform for creating planar waveguide circuits [2]. The development of individual components has been the subject of intense research during the last decade. More recently, significant efforts have also been devoted towards photonic integration of a high number of components. In this way, several breakthrough results have been achieved in last years.

1.1. Silicon photonics

In 2010, Intel demonstrated a 50Gb/s photonic link based on silicon based integrated transmitter and receiver chips [3]. One year later, Luxtera announced a 100-Gb/s silicon photonic transceiver based on four fully integrated 28Gb/s transmit and receive modules powered from a single laser [4]. In Japan, a 12.5 Gb/s photonic transceiver integrating an arrayed laser diode, an optical splitter, silicon modulators and germanium photodetectors on a single silicon substrate was demonstrated [5, 6] .

In Europe, several complex silicon photonics devices have been demonstrated. It must be highlighted a silicon modulator monolithically integrated with a SiGe CMOS RF driver. Furthermore, a single channel 10Gb/s photonic transmitter integrating a hybrid III-V/silicon laser with a silicon modulator was achieved. Then, a 5Gb/s DQPSK receiver and transmitter integrating germanium photodetectors and silicon modulators with passive circuitry has also been demonstrated [7].

All these breakthrough results have highlighted the potential of silicon CMOS photonics for a wide range of applications but especially those requiring high-volume manufacturing such as telecom, datacom or sensing.

However, despite the huge potential of silicon photonics, several challenges need still to be addressed for enabling the full development of commercial products. One of the main challenges is still related to improve the key active photonic components. Silicon itself imposes barriers to the ultimate active performance that can be achieved and therefore the integration of new materials on silicon is emerging as an active field in silicon photonics to overcome its limitations with the potential to generate technology breakthroughs leading to novel markets and applications. Clear examples of that are:

- III-V compounds have been widely investigated for solving the lack of an on-chip light source in silicon due to their well-proven lasing properties. Hybrid III-V/silicon lasers have been demonstrated using both bonding and epitaxial growth to transfer the III-V materials to the silicon wafer [8, 9]. However, there are still remaining challenges facing with the difficulties associated by the incompatibility of III-V materials with the standard CMOS process.
- Silicon is transparent at wavelengths longer than $1,1\mu\text{m}$ and therefore cannot be employed as a photodetector at $1,5\mu\text{m}$. Germanium is currently accepted as the best approach for enabling photodetection in silicon at 1550 nm optical wavelengths due to its excellent properties for light absorption in the near infrared and CMOS compatibility. High performance has been achieved thanks to the efforts devoted on improving the epitaxial growth technique for overcoming the difficulties inherent to the lattice mismatch between these two materials [10]. Hence, a very high bandwidth of 120 GHz with a responsivity of 0.8 A/W and zero-bias operation (minimizing power consumption) was demonstrated [11].
- Another known drawback in silicon is the lack of Pockels effect due to its centrosymmetric nature. Among other options, that later will be analysed, transition metal oxides (TMO) stand out as promising solutions to achieve EO

Chapter 1: Introduction

modulation in silicon. TMO materials comprise a very diverse and fascinating class of compounds with properties that can be tailored for a wide variety of applications. More concretely, they have unique EO properties that will offer unprecedented and novel capabilities to the silicon platform (Figure 1.2). Many transition metal oxides have been prepared in bulk form or in thin films in the past several decades. However, obtaining single crystalline and high quality photonic waveguides has been a long-standing issue. The difficulty is largely related to the complex composition of TMOs, and most synthetic techniques developed in the past for nanophotonic waveguides cannot be simply applied. In fact, the benefit of using such materials is directly related to the structural quality of the crystal, so that a high quality fabrication process is a must for producing single crystal thin films. Recent significant progress in deposition tools and methods has enabled the growth of single crystal oxide layers onto low-cost large-size silicon substrates [12]. These recent developments in the epitaxy of transition metal oxides have substantially lowered the barrier to integrate high quality photonic waveguiding structures on silicon.

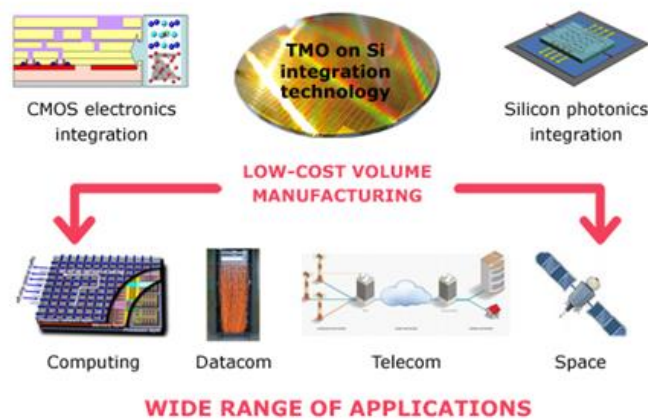


Figure 1.2: The combination of the TMOs with the Silicon platform mix the characteristics of both technologies allowing for new applications in a wide range of fields.

The last point is in which this thesis is focused. More concretely, among TMO materials, barium titanate (BaTiO_3 or BTO) stands out as one of the most disruptive candidates. The integration of BaTiO_3 in silicon is one of the most promising options for the implementation of EO functionalities, especially EO modulation, with beyond state-of-the-art performance which cannot be afforded currently in silicon photonics technology itself.

This thesis has been developed in the framework of the European project SITOGA (Silicon CMOS compatible transition metal oxide technology for boosting highly integrated photonic devices with disruptive performance), included in the seventh framework programme (FP7-ICT-2013-11-619456). SITOGA project addresses for the integration of TMO materials in the silicon photonics platform for offering breakthrough EO functionalities due to their unique properties not present in pure silicon. Such integration combined with the development of beyond state-of-the-art photonic devices

1.2. Electro-optic modulation in silicon

paves the way towards a wide range of photonic applications. The SITOGA consortium has been formed by the following partners: Centre National de la Recherche Scientifique (CNRS, France), Katholieke Universiteit Leuven (KU Leuven, Belgium), Innovations for High Performance microelectronics (IHP GMBH, Germany), IBM Research GMBH (IBM, Switzerland), DAS Photonics (DAS, Spain) and Universitat Politècnica de Valencia (UPV, Spain), being the later the project coordinator.

The main objectives of the SITOGA project are listed below:

- Develop the technology (deposition pathways and processing) of two innovative TMO materials, BaTiO₃ and VO₂, with unique properties for boosting photonic integration in silicon CMOS.
- Demonstrate beyond state-of-the art EO modulation and switching photonic components.
- Integrate the developed material technology on the silicon CMOS platform for large-scale manufacturing of highly integrated and complex photonic devices.
- Validate the enhanced capabilities provided to the silicon platform by means of two functional demonstrators and define the roadmap for the exploitation of the developed technology.

1.2. Electro-optic modulation in silicon

Optical modulators are key building-blocks in communication systems because they link optical and electrical domains [13]. The work developed in this thesis is essentially focused on the design, fabrication and characterization of compact and efficient modulators based on BaTiO₃ integrated in silicon. In this section we summarize its main characteristics and the different existing mechanisms to develop EO modulators in silicon.

1.2.1. Optical modulators

An optical modulator is a device which can be used for modulating (i.e. changing the properties of) an optical beam. In the context of telecommunications, modulation is the process of transporting a message signal inside another signal that can be physically transmitted. There are many different kinds of modulators, which can be classified regarding to the physical property of light which is manipulated. In this way, we can find phase modulators, intensity modulators, polarization modulators or spatial light modulators. Another way of classifying modulators is depending on the physical effect. Thus, we can find acousto-optic modulators, electro-optic modulators or electro-absorption modulators. Likewise, another main way of classifying modulators is by the signal type of the modulating signal. If the optical carrier is modulated by means of a continuous electrical signal we have analog optical modulation. In contrast, if the optical

Chapter 1: Introduction

carrier is modulated by a discontinuous signal that carries information in binary form (i.e. '0's and '1's), we have digital optical modulation. In Figure 1.3 it can be seen illustrated the example of analog and digital modulation.

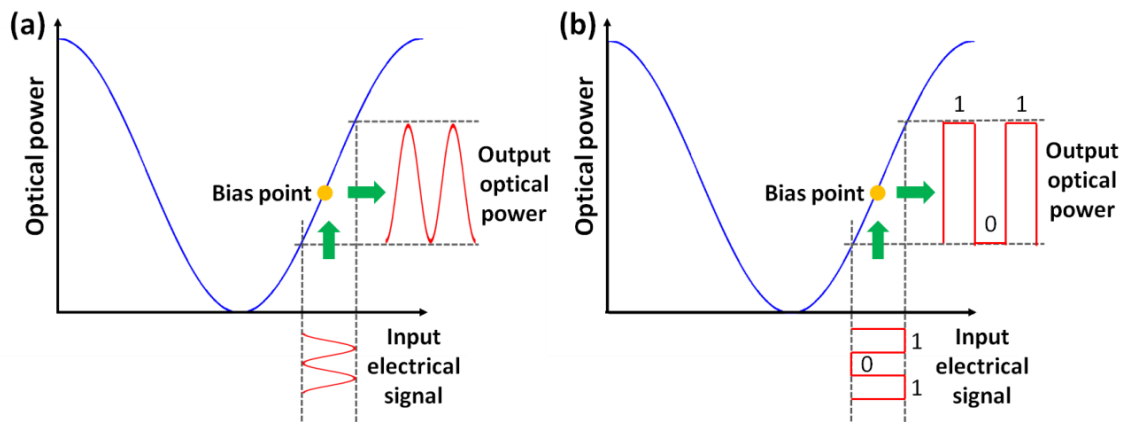


Figure 1.3: (a) Analog and (b) digital modulation [14].

1.2.2. Different mechanisms for electro-optic modulation in silicon

As aforementioned, an optical modulator is a device that is used to modulate a light beam that propagates either in free space or in an optical waveguide. Besides the classification mentioned in previous subsection referring to the different parameters of the beam which that can be altered, modulators can be also classified into two operational categories: electro-optical and electro-absorption.

The application of an electric field to a material can result in a change in the real and imaginary part of refractive indices. A change in real part of refractive index, Δn , due to the applied electric field is known as EO effect, and a change in the imaginary part of refractive index, $\Delta\alpha$, due to the applied electric field is known as electro-absorption effect. The dependence of the refractive index on the applied electric field usually takes one of these forms:

- The refractive index change is proportional to the applied electric field, in which the effect is known as the linear EO effect or Pockels effect.
- The refractive index change is proportional to the square of the applied electric field, in which the effect is known as the quadratic EO effect or the Kerr effect.

In this thesis, we will focus on EO modulators and more specifically, in the linear EO Pockels effect as the most effective mechanism to achieve high modulation efficiency at very high speed modulation. However, this kind of EO modulation is not a trivial solution in silicon photonics platform. As mentioned in the previous section, despite the huge potential of silicon photonics, there are fundamental constraints arising from material properties itself, which limit the complete development of commercial devices. One of them is the lack of linear EO coefficient due to the centrosymmetric crystallographic nature of silicon. Hence, Pockels effect is not directly possible to implement in pure

1.2. Electro-optic modulation in silicon

silicon at the communications wavelengths of 1.3 μm and 1.55 μm [15, 16]. Therefore alternative modulation means have to be found for silicon.

One option is to use thermal modulation, as silicon exhibits a large thermo-optic coefficient, although this is too slow for the high frequencies required in modern communications applications [17]. To date, the most common modulation mechanism used in silicon devices is the plasma dispersion effect. This physical effect consists in varying the free carrier concentration of a semiconductor, which in consequence changes both the real and imaginary parts of its refractive index [18]. Soref and Bennett studied results in the scientific literature to evaluate the change in refractive index, Δn , due to experimentally produced absorption curves for a wide range of electron and hole densities, over a broad range of wavelengths. They also quantified the changes for both changes in refractive index besides in absorption, and finally they produced a well-known expression to evaluate changes in the density of carriers in silicon [19]. However, this approach makes currently not possible to reach the requirements of low power consumption at high speed operations simultaneously [15]. The employment of small voltage values (under 2V) is necessary for reducing the power consumption as much as possible for allowing CMOS integration. Moreover, complex doping steps are required, which may give rise to high loss levels.

EO modulation by means of the Pockels effect has been demonstrated by breaking the crystal symmetry of silicon [20]. Thereby, promising results have been achieved by exploiting the strain induced by silicon nitride (SiN) on top of narrow silicon waveguides [21]. Nevertheless, recent studies have shown that free carriers have a prominent role and one order of magnitude lower effective Pockels coefficient has been measured at high frequencies [22].

The integration of materials compatible with silicon CMOS photonics has therefore become a promising way to achieve EO modulation via Pockels effect with the best performance. Polymers with a high second-order nonlinearity coefficient have been used as cladding [23] or in silicon based slot waveguides [24]. However, high temperature processes are usually required which makes more difficult the integration with standard CMOS steps. More recently, ferroelectric oxides have been attracting an increasing interest due to their high EO coefficients. The most known ferroelectric oxide is lithium niobate (LiNbO₃), which is currently used in commercial EO modulators. The main strength of this material is that presents a high Pockels EO effect, which let us afford high velocity modulation and low voltage values and insertion losses. However, although different attempts have been investigated, the integration of high-quality films on silicon has only been achieved via layer-bonding approaches [25, 26].

1.2.3. Structures for modulation

In previous section different modulation mechanisms have been introduced. As already discussed, the EO Pockels effect alters the refractive index of the waveguiding structure

Chapter 1: Introduction

which integrates the EO material by applying an electric field. This variation in the refractive index implies an optical phase change of the light passing through it, hence acting as a phase modulator. This optical phase modulation must be converted into an amplitude modulation by integrating this phase shifter structure in a Mach-Zehnder Interferometer (MZI) or a ring resonator. Below, the basic principles of these structures are presented.

1.2.3.1. MZIs

In brief, the MZI mechanism consists in splitting the light from a single source into the two arms of this interferometric structure. When these two beams are recombined, the different phase shift between them induced by the application of an external electric field can be converted into an amplitude modulation.

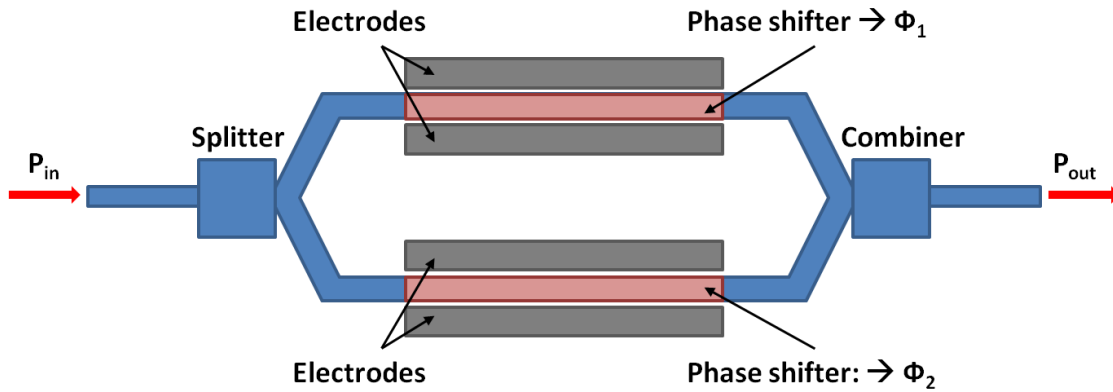


Figure 1.4: Basic schematic of a MZI modulator [14].

The device is schematically depicted in Figure 1.4. The main advantages of an MZI lie in its simplicity and its large optical bandwidth. Furthermore, these devices are temperature independent. In contrast, the main drawback is the relatively large phase shifter length required. If an electric field is applied to one arm, due to the EO effect, it induces a change in the refractive index of this arm and therefore a change in the phase of the light propagating into that arm (Φ_1 or Φ_2). When both beams are combined with different phase, this phase modulation is converted into an intensity (amplitude) modulation. The transfer function of the MZI is a sinusoidal function and is defined as follows:

$$\frac{P_{out}}{P_{in}} = \cos^2\left(\frac{\Delta\Phi}{2}\right) \quad (1.1)$$

where P_{in} is the power input, P_{out} is the output power and $\Delta\Phi = \Phi_2 - \Phi_1$ is the phase difference between both arms.

1.2. Electro-optic modulation in silicon

For our purposes, we used asymmetric MZI. The main characteristic is the fact that there is a difference of length between both arms.

1.2.3.2. Ring resonators

A ring resonator basically consists of a ring waveguide and a straight waveguide placed close to each other, coupling the light between both structures (Figure 1.5).

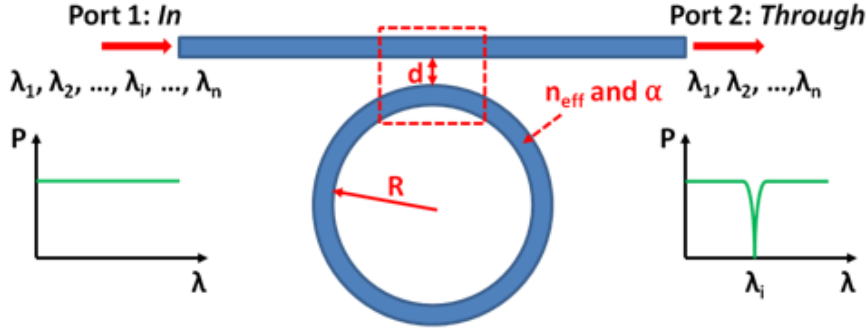


Figure 1.5: Ring resonator configuration and the most important design parameters [14].

In this way, a resonance takes place when the propagation length of the resonator is exactly a whole number of wavelengths:

$$n_{eff}L = M\lambda_i \quad (1.2)$$

where n_{eff} is the effective index, L is the length of the ring, M is a whole number and λ is the wavelength.

Hence, a continuous wave of a certain wavelength is injected into the ring resonator. Minimum transmission is achieved when the wavelength is located at a resonance. Furthermore, this transmission is ideally zero when the ring operates at critical coupling, i.e. when the coupled power is equal to the power lost in the ring (critical coupling condition). Therefore, ring resonators support multiple resonances.

An important parameter is the width at half maximum ($FWHM$), known as the width of the resonance at 3dB, while quality factor (Q) is a measure of the sharpness of the resonance:

$$Q = \frac{\lambda_{res}}{\Delta\lambda_{FWHM}} \approx \frac{2\pi n_g}{\alpha \lambda} \quad (1.3)$$

where λ_{res} is the resonance wavelength, n_g is the group index and α is the loss per unit length.

Chapter 1: Introduction

1.2.3.3. Amplitude modulation principle

Basic performance of an intensity modulator is shown in Figure 1.6. If an electric field is applied to the electrodes of an amplitude modulator due to the EO effect, it induces a change in the refractive index and a shift in the resonance. Hence, the spectral response of the ring resonator or the MZI is shifted when the effective index is modified consequently changing the output power.

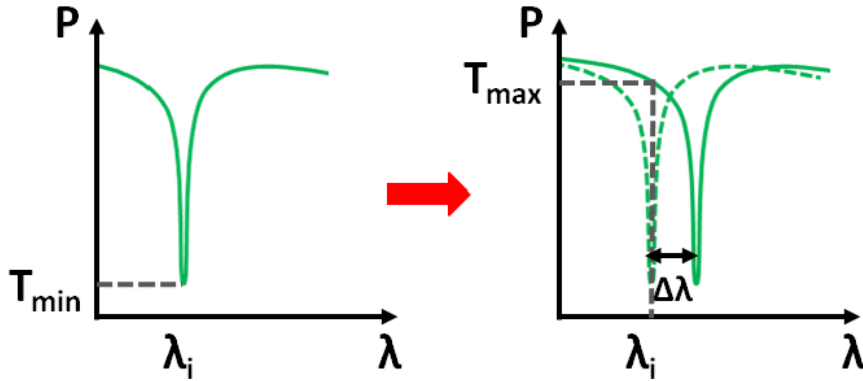


Figure 1.6: Basic performance of an intensity modulator based on an amplitude modulator [14].

The effective index change can be obtained from such resonance shift by next equation:

$$\Delta n_{eff} = \frac{\Delta \lambda}{FSR} \frac{\lambda}{L_{active}} \quad (1.4)$$

where the FSR (Free Spectral Range) is defined as the spacing between the resonances and can be obtained by the following equation:

$$FSR = \frac{\lambda^2}{n_g L} \quad (1.5)$$

where λ is the wavelength, n_g is the group index and L is the length.

Then, particularly for each kind of above mentioned modulator, the effective index change from the resonance shift is defined as:

$$\begin{aligned} MZI &\rightarrow \Delta n_{eff} = \frac{\Delta \lambda}{\lambda} n_g \frac{\Delta L}{L_{active}} \\ Ring &\rightarrow \Delta n_{eff} = \frac{\Delta \lambda}{\lambda} n_g \frac{L_{ring}}{L_{active}} \end{aligned} \quad (1.6)$$

where L_{active} is the length corresponding to the waveguide structure in contact with the electrodes and the active EO material. ΔL represents the difference of length between both arms of the MZI while $L_{ring}=2\pi R$, being R the radius of the ring.

Finally, from this effective index change, the induced phase shift is defined as:

$$\Delta\Phi = \frac{2\pi}{\lambda} L \Delta n_{eff} \quad (1.7)$$

Therefore, to optimize the performance of an intensity modulator, we are interested in the lowest transmission at resonance to maximize the extinction ration and the narrowest spectrum to minimize the required frequency shift, i.e. the required external voltage and therefore minimize the power consumption.

The voltage required to obtain a phase shift of π , and also the most used figure of merit to quantify the efficiency of a modulator, is known as the half-way voltage (V_π). The relation between the V_π and the phase shift is:

$$\Delta\Phi = \frac{2\pi}{\lambda} \Delta n_{eff}(V_\pi) L = \pi \rightarrow \Delta n_{eff}(V_\pi) = \frac{\lambda}{2L} \quad (1.8)$$

1.3. Barium titanate

BaTiO₃ has been one of the first ferroelectric materials ever discovered, and one of the most thoroughly investigated so far. Firstly used in ceramics [27], this material has drawn attention because of its enticing ferroelectric, piezoelectric and dielectric properties among others [28-42]. Here we realize a review of its most important properties, like its ferroelectricity or anisotropy, and a brief presentation of the state-of-the-art of modulators based on BTO.

1.3.1. Ferroelectricity and domain structure

BaTiO₃ is a well-known ferroelectric oxide. The phenomenon of ferroelectricity was firstly discovered in Rochelle salt in 1921 [43]. The main characteristics that all ferroelectric materials share are the existence of spontaneous polarization and the fact that the polarization can be reoriented [44]. When a spontaneously polarized region possesses a single direction of polarization, it is called domain. In the tetragonal phase of the BTO, which is later explained, we can find two types of domain walls.

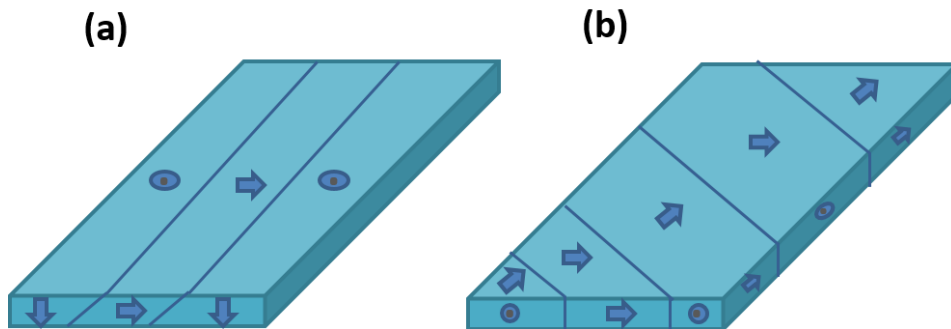


Figure 1.7: (a) An “a” domain between two “c” domains and (b) only “a” domains.

Chapter 1: Introduction

The first kind are called 90° domains and separates ferroelectric domains which are polarized perpendicularly to each other. The second type of domain walls is called 180° domain and separates ferroelectric domains which are polarized antiparallel to each other. More specifically, when the polarization vector is in the surface plane, the domain is called “a” domain. On the contrary, when it is perpendicular to the surface plane it is called a “c” domain [45]. Both “a” and “c” domains are shown in Figure 1.7. Probably the most interesting feature of a ferroelectric oxide is the hysteresis loop, depicted in Figure 1.8.

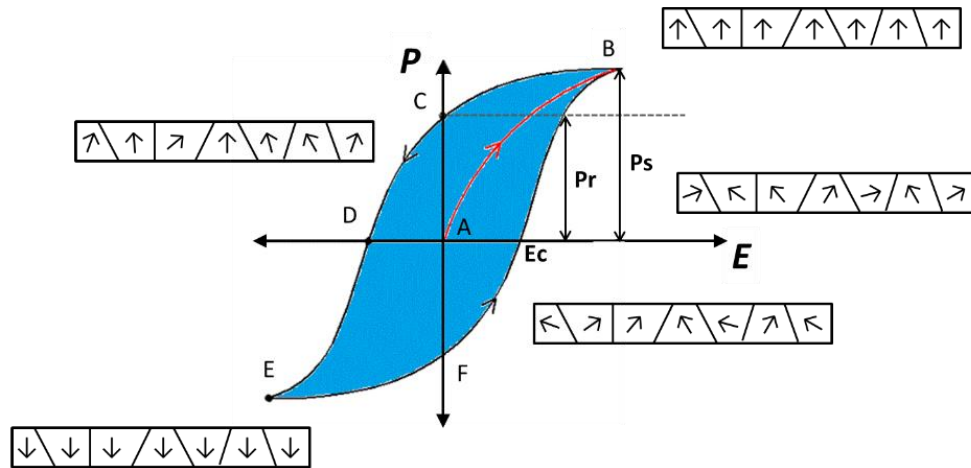


Figure 1.8: Characteristic P-E hysteresis loops of ferroelectric materials [45].

Before applying an electric field, the domains will be randomly aligned. Therefore, when an electric field is applied, those domains which are already oriented in the same direction of the field will remain aligned. However, those which are aligned in another direction, will experience a tendency to change their orientation towards the direction in which the electric field is applied. When the electric field is increased to a given value to switch the domains, known as the coercive field, the polarization changes rapidly and is saturated at higher electric fields. If now the electric field is decreased to zero, a permanent polarization net remains, known as remanent polarization. When reversing the electric field to negative values, the polarization is reduced to zero and then the sign is changed due to the saturation polarization that the field produces in the opposite direction. Therefore, the hysteresis loop is completed, as shown in Figure 1.8.

This ferroelectric nature is inherent to the crystal structure. Above Curie temperature ($T_C=120^\circ\text{C}$ for BTO), this member of the perovskites has a centrosymmetric cubic structure and thus behaves like a dielectric without spontaneous polarization. On the contrary, below Curie temperature (at room temperature) its crystal structure changes to tetragonal phase, which is illustrated in Figure 1.9, thus yielding to a stretching of the ‘c’ lattice parameter and a corresponding shrinking of ‘a’ and ‘b’ parameters ($a=b$). In this situation, the material is non-centrosymmetric and presents a spontaneous polarization parallel to the crystallographic “c” axis. In fact, during the cubic to tetragonal phase transformation at Curie temperature, the domain structure is formed.

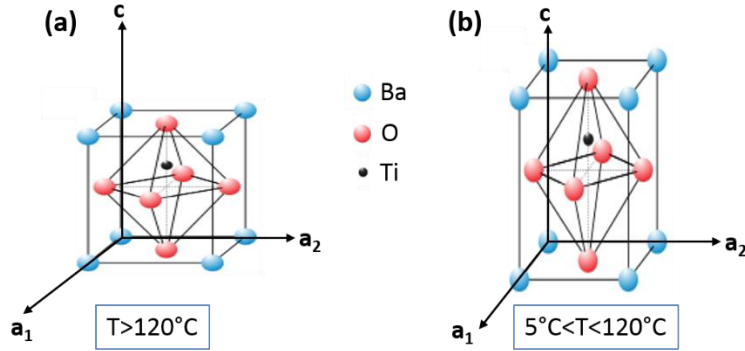


Figure 1.9: BaTiO₃ crystal structure in (a) cubic phase and (b) tetragonal phase.

Specifically, the tetragonal form of the crystal structure implies that the material can be grown with two different orientations depending on the process conditions: an in-plane polarization of tetragonal BTO films implies that the “c” axis is along the growth plane (usually defined as a-axis orientation). Oppositely, an out-of-plane polarization indicates a BTO film with its “c” axis perpendicular to the growth plane (usually defined as c-axis orientation). Furthermore, the resulting orientation of BTO film can vary from purely a-axis to c-axis orientations, through a mixture of a and c-axes oriented configurations [46]. Epitaxial growth of BTO films offers the possibility to select the direction in which the spontaneous polarization can appear depending on the desired application [47].

1.3.2. Anisotropy

BaTiO₃ is a negative uniaxial anisotropic crystal. Anisotropy means that the properties of this material vary through different directions in a different way. Its permittivity and refractive index depends on the direction of the crystal axes. Anisotropic crystals can be divided regarding to its symmetry in uniaxial or biaxial, if they possess either one or two optical axes. In the case of BTO, as a uniaxial crystal, it presents birefringence, being the refractive index of one crystal axis different from the other crystal axes. Concretely, BTO presents an ordinary index ($n_o = 2.444$) larger than the extraordinary index ($n_e = 2.383$) [51]. Due to the lower n_e compared to n_o , BaTiO₃ is defined as a negative uniaxial crystal.

As above mentioned, anisotropic media present different optical properties depending on the direction of the incident light. Therefore, as the refractive index changes with the direction of the light waves, it is interesting to know the refractive indexes in any direction of the light passing through the material. In this way, the refractive index ellipsoid depicts the relative magnitude and orientation of refractive indices in a crystal. Specifically, the refractive index ellipsoid for uniaxial anisotropic crystals in the absence of an electric field can be expressed as:

$$\frac{x^2}{n_o^2} + \frac{y^2}{n_o^2} + \frac{z^2}{n_e^2} = 1 \quad (1.9)$$

1.3.3. Pockels effect

The Pockels effect is a well-known and highly developed EO mechanism. This effect takes part when an electric field is applied to a crystal which lacks inversion symmetry. In one dimension, the electric field changes linearly the refractive index as follows:

$$\Delta n(E) \approx -\frac{1}{2}n_0^3 r_{\text{eff}} E \quad (1.10)$$

where Δn is the refractive index change, n_0 is the unperturbed refractive index, r_{eff} is the effective Pockels coefficient and E the applied electric field.

Pockels coefficients form a tensor, which can be expressed by this reduced matrix:

$$\begin{pmatrix} \Delta\left(\frac{1}{n^2}\right)_1 \\ \Delta\left(\frac{1}{n^2}\right)_2 \\ \Delta\left(\frac{1}{n^2}\right)_3 \\ \Delta\left(\frac{1}{n^2}\right)_4 \\ \Delta\left(\frac{1}{n^2}\right)_5 \\ \Delta\left(\frac{1}{n^2}\right)_6 \end{pmatrix} = \begin{pmatrix} r_{11} & r_{12} & r_{13} \\ r_{21} & r_{22} & r_{23} \\ r_{31} & r_{32} & r_{33} \\ r_{41} & r_{42} & r_{43} \\ r_{51} & r_{52} & r_{53} \\ r_{61} & r_{62} & r_{63} \end{pmatrix} \begin{pmatrix} E_x \\ E_y \\ E_z \end{pmatrix} \quad (1.11)$$

More concretely, in the case of BaTiO₃, this tensor can be written as:

$$\begin{pmatrix} \Delta\left(\frac{1}{n^2}\right)_1 \\ \Delta\left(\frac{1}{n^2}\right)_2 \\ \Delta\left(\frac{1}{n^2}\right)_3 \\ \Delta\left(\frac{1}{n^2}\right)_4 \\ \Delta\left(\frac{1}{n^2}\right)_5 \\ \Delta\left(\frac{1}{n^2}\right)_6 \end{pmatrix} = \begin{pmatrix} 0 & 0 & r_{13} \\ 0 & 0 & r_{13} \\ 0 & 0 & r_{33} \\ 0 & r_{51} & 0 \\ r_{51} & 0 & 0 \\ 0 & 0 & 0 \end{pmatrix} \begin{pmatrix} E_x \\ E_y \\ E_z \end{pmatrix} \quad (1.12)$$

where the EO coefficients values (r_{ij}) in its bulk form have been measured to be $r_{13}=8\text{pm/V}$, $r_{33}=28\text{pm/V}$ and $r_{51}=800\text{pm/V}$ [28].

Since the ferroelectric polarization and the EO properties are tensorial quantity, the orientation of the BTO layer will largely impact the performance of the EO devices.

Orientation is crucial to the implementation of EO activity. Hence, the study of the crystalline orientation of the BTO becomes an essential issue.

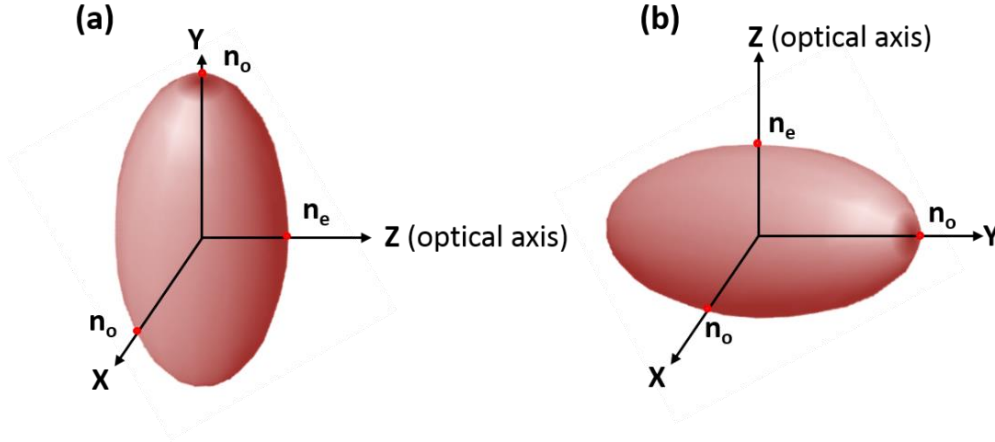


Figure 1.10: Crystallographic axes, a_1 , a_2 and c , are aligned along the coordinate system with axes x , y and z , respectively for (a) a -axis and (b) c -axis BTO respectively.

In this way, the EO effect can be modelled by using the index ellipsoid, which is sketched in Figure 1.10. The index ellipsoid in the presence of an electric field (E_x , E_y , E_z) is given by next equation:

$$\left(\frac{1}{n_o^2} + r_{13}E_z\right)x^2 + \left(\frac{1}{n_o^2} + r_{13}E_z\right)y^2 + \left(\frac{1}{n_e^2} + r_{33}E_z\right)z^2 + (r_{51}E_y)2yz + (r_{51}E_x)2zx = 1 \quad (1.13)$$

The coordinate system with axes x , y , and z of the index ellipsoid is aligned along the crystallographic axes a_1 , a_2 and c , respectively, of the BaTiO_3 crystal structure.

Therefore, the EO performance will depend on how the BaTiO_3 is grown to fabricate the waveguide structure. As aforementioned, the so-called a -axis or c -axis orientations will depend on if the optical axis (“ z ” axis) is in-plane or out-of-plane in the BaTiO_3 layer.

Because of its ultra-large linear EO coefficients, BaTiO_3 has been the subject of intense research in the last decade. Indeed, BTO bulk single crystals exhibit a Pockels coefficient more than 20 times higher than LiNbO_3 single crystals [28], which makes BTO an excellent active material for the fabrication of a large variety of EO devices such as switches, tuning elements and optical modulators with low drive voltage, large bandwidth, compact size and thermal stability.

1.3.4. Barium titanate on SOI

Due to the fact that is chemically and mechanically very stable and it shows ferroelectric properties, BTO is suitable for practical applications. Besides, BaTiO_3 is very interesting because of its high optical transparency and its favourable growth characteristics, as previously commented.

Chapter 1: Introduction

Material unique properties at 1550nm optical wavelength	Key enhanced capabilities offered to the silicon platform
<ul style="list-style-type: none">• Ultra-high Pockels coefficient• Very low optical losses• High refractive index• Bistable performance via ferroelectric domain switching	<ul style="list-style-type: none">• Ultra-fast and linear optical phase modulation• CMOS compatible drive voltages with low insertion losses• Electro-optical bistable performance for non-volatile photonic devices

Table 1.1: BTO has disruptive properties at optical wavelengths which provide enhanced capabilities like ultra-small footprint and ultra-low power consumption to the silicon platform.

Furthermore, the potential of growing high-quality thin film crystalline layers of BTO on strontium titanate (SrTiO_3) templated silicon and silicon on insulator (SOI) substrates [12, 49, 50] has recently opened a path towards the development of hybrid BTO silicon EO modulators with disruptive performance [51-56]. Table 1.1 summarizes the BaTiO_3 properties at 1550nm optical wavelength and the enhanced capabilities offered to the silicon platform.

1.3.5. State-of-the-art of BTO based modulators

BaTiO_3 modulators have been mainly investigated so far on top of magnesium oxide (MgO) substrates [57-60]. Among the research groups that have been recently working on the integration of BTO for photonic applications, Wessels team at Northwestern University (USA) is one of the most relevant and photonic devices with promising performance have been demonstrated by integrating BTO thin films on magnesium oxide (MgO) substrates, demonstrating BTO optical waveguides with losses below 0.5 dB/cm at 1550 nm wavelengths [61]. In addition, BTO electro-optical modulators have been fabricated with poly-domain tetragonal BTO on a (100) MgO substrate, using a Si_3N_4 strip-loaded wave guide, a SiO_2 buffer layer and Cr/Au metal electrode layers. The waveguides are characterized by low propagation losses (1dB/cm at 1.55 μm) and the modulator has a $V_\pi \cdot L$ product as low as 0.5 V·cm at 1561 nm from which an effective Pockels coefficients r_{eff} as high as 360 pm/V was extracted [62]. Experimental results and numerical calculations also showed the potential for a modulation bandwidth in excess of 40GHz [63]. On the other hand, the demonstration of nonlinear photonic crystal waveguide structures showed the feasibility of fabricating nano-sized optical structures with BTO as an active material using lithography techniques [64, 65]. To overcome the difficulties in patterning and etching BTO especially at nanoscale dimensions, a strip waveguide was used consisting of BTO as the active layer and Si_3N_4 slab layer to define the strip of the Bragg grating.

Chapter 1: Introduction

Recently, IBM has demonstrated the integration of a ferroelectric BTO film on silicon exhibiting a strong linear EO effect with an effective Pockels coefficient of $r_{\text{eff}} = 148$ pm/V [47]. This value exceeds previous data reported for integrated LiNbO₃ by at least a factor of five, and for strained Si by a factor of 100. Furthermore, they also demonstrate the presence of ferroelectricity in the BTO film opening the way for enabling breakthrough photonic functionalities by exploiting the EO bistable effect. Another group of Yale university (USA) has been able to integrate BaTiO₃ based Mach-Zehnder and ring modulators on SOI using a slot waveguide structure [49]. They extracted an effective Pockels coefficient of 213 ± 49 pm/V, and demonstrated 4.9 GHz operation with a $V_{\pi} \cdot L$ of 1 V.cm. Table 1.2 summarizes the state-of-the-art of EO modulators based on BTO.

1.4. Objectives and outline of the thesis

The aim of this work has been to demonstrate EO modulation at high speed based on the integration of barium titanate on silicon. It must be pointed out that, for this purpose, strong collaboration has been realized with the Centre National de la Recherche Scientifique in Lyon, France and IBM Research GMBH at IBM, in Switzerland. In this context, cooperation in the optimization of the needed fabrication processes for the implementation of nanophotonic structures based on the integration of barium titanate in silicon photonics technology has been pursued. The study and implementation of the most suitable waveguide structures to exploit the unique EO properties of BaTiO₃ on silicon has been essential towards the development of new structures based on the developed technology that allowed the implementation of EO modulation devices with disruptive performance.

The contents of this work are structured in four chapters. This first chapter aims to provide the fundamentals of silicon photonics. After a brief review of this technology, its benefits and opportunities have been shown as well as its challenges. The concept of an optical modulator has been given, besides different ways of classifying them. Special emphasis has been made on the main physical mechanisms used for EO modulation in silicon. TMOs materials have been introduced, highlighting barium titanate. Its main properties, like anisotropy and ferroelectricity have been presented as well as the discussion about the types of ferroelectric domains. Finally the state-of-the-art of EO modulators based on BTO has been analysed.

Chapter 2 contains all the design work that has been done. It starts with the simulations carried out in order to choose the kind of waveguide structure for modulating. Hence, the optical design is focused on seeking all parameters of the chosen structure in order to provide optical confinement and low propagation losses. Special emphasis is made on analysing the best performance for both a-axis and c-axis configuration. Later then, the process of the election of the electrodes placement and the RF design have been investigated to obtain the best EO performance.

1.4. Objectives and outline of the thesis

Chapter 3 is dedicated to fabrication processes and experimental results. The main technics of barium titanate deposition are described. The optimization of the amorphous silicon deposition is also explained, showing the experimental results that have allowed us to achieve a-Si waveguides with good quality and low losses. The a-Si/BTO/Si stack fabrication process besides the electrode fabrication steps followed during this work are detailed. Afterwards, the main experimental results are shown. Firstly, the optical results are explained for all processed samples. Then, modulating structures such as ring resonators and MZIs are characterized at DC performance. Henceforth, the devices that presented EO behaviour were characterized at RF frequencies. At the end, modulation results at high frequency are shown.

Finally, in chapter 4 the conclusions and future work are discussed.

Chapter 2

Design of electro-optic modulators based on BaTiO₃ in silicon

2.1. Optical design

The starting point towards developing an electro-optic (EO) modulator is the optical design. In this stage, passive waveguides must be designed with the aim of obtaining low propagation losses when the light is guided. Furthermore, for our purpose, the structure must be optimized with the objective of ensuring single mode operation and strong light confinement in the slot region, being the latter evaluated by optically estimating the upper bound of the overlap integral (Γ_{\max}) between the electric field and optical mode. In this way, a thoroughly study is carried out to accomplish the three main objectives above commented by properly designing all the parameters involved in the waveguiding structure as thicknesses and widths of the layers.

2.1.1. Slot waveguide structure

In order to exploit the EO effect in the barium titanate (BTO) layer, we have used a slot-waveguide configuration, with the BTO material located in the slot region (Figure 2.11). Firstly introduced at the beginning of this century by V. R. Almeida at Cornell University [70], the slot waveguide basically consists of a narrow low index region sandwiched between two high index slabs.

The operating principle relies on the discontinuity of the electric field at the high refractive index contrast interface. For this kind of structure, Maxwell's equations state

Chapter 2: Design of electro-optic modulators based on BaTiO₃ in silicon

that to satisfy the continuity of electric flux density D , the corresponding electric field E must experience a large discontinuity. This discontinuity causes a much more intense electric field in the low index horizontal slot region. Therefore, the field in the slot is much higher than that in the high-index regions for TM polarization.

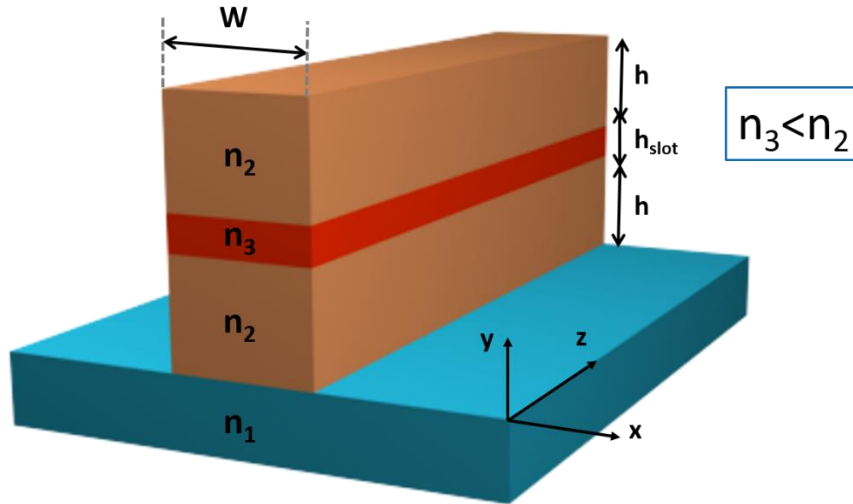


Figure 2.11: Cross-section of the slot waveguide structure

2.1.2. Design of the slot waveguide

As before mentioned, our waveguide structure is based on a horizontal slot waveguide design enabling strong light confinement in the waveguide core. In this structure, the active BTO core is cladded between the Si layer of the SOI substrate and a deposited amorphous silicon (a-Si) layer. In the first place, two waveguiding structures were envisaged (Figure 2.12).

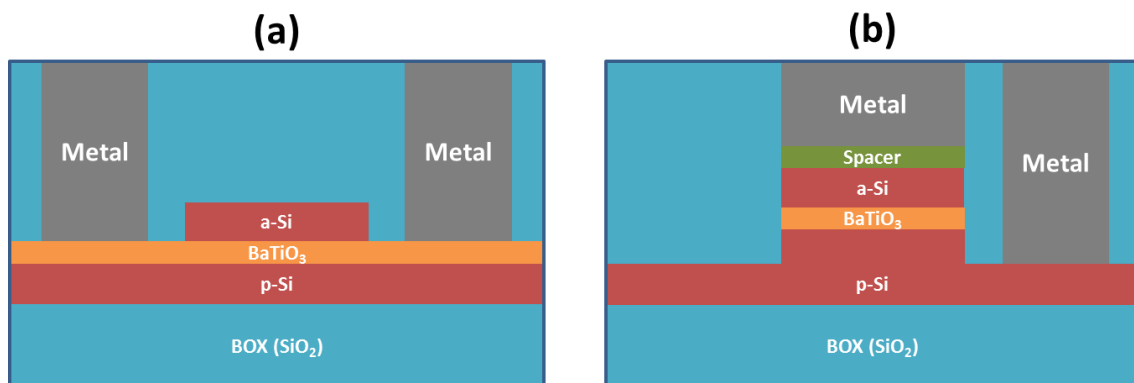


Figure 2.12: Schematics of the two waveguiding architectures: (a) halfway etched waveguide with lateral contacting scheme and (b) fully etched waveguide with vertical contacting scheme.

In the halfway etched (HE) structure (Figure 2.12(a)), only the a-Si layer is etched, which eases the fabrication process since BTO etching is not necessary to be developed.

In this case, the BTO is polarized using lateral contacts. The main problem here is the large distance between the electrodes in order to limit absorption losses. On the other hand, the fully etched (FE) design (Figure 2.12(b)) is expected to provide larger optical confinement in the BTO layer. Now, the structure is etched down to the Si layer of the SOI substrate (etching is stopped somewhere in this layer) which requires to control the BTO etching and using vertical contacts to apply the electric field. Nevertheless, a spacer has to be placed between the waveguide and the top electrode to reduce absorption losses down to reasonable values.

To reduce the voltage drop and effectively polarize the BTO layer, this spacer must have an elevated permittivity and the Si layer of the SOI substrate as well as the a-Si layer must be sufficiently doped. The main advantages and drawbacks of both configuration are summarized in Table 2.1.

Waveguide Structure	Advantages	Drawbacks
Fully Etched	<ul style="list-style-type: none"> High optical confinement in waveguide core (small bending radii possible) 	<ul style="list-style-type: none"> Good BTO etching required (potentially high propagation losses) Low horizontal electric field in BTO slot due to high BTO permittivity
Halfway Etched	<ul style="list-style-type: none"> No BTO etching required Lower propagation losses Strong horizontal electric field 	<ul style="list-style-type: none"> Lower confinement in waveguide core (larger bending losses)

Table 2.1: Benefits and disadvantages of fully etch and halfway etched configuration.

Furthermore, the choice between FE and HE configuration also depends on the orientation of the ferroelectric polarization in the BTO material. A more detailed description of each structure is presented beneath besides simulation results which will be used to determine the final waveguide structure choice.

2.1.2.1. Half etched waveguide

An important issue set at the beginning of this work was to develop a waveguide structure which could support both TE and TM modes simultaneously. Due to the different optical confinement of TE and TM modes in the waveguide, one must be aware of optical losses in both of them. In our case, the latter will be more affected from absorption losses due to its mainly horizontal confinement in the BTO region. Despite both modes have been taken into account at the same level of importance, the results regarding to losses presented here have been focused more on TM since it limits the choice of the waveguide

Chapter 2: Design of electro-optic modulators based on BaTiO₃ in silicon

parameters mostly than TE. Initially, the influence of silicon layer thickness (t_{Si}) on the waveguide performance has been evaluated.

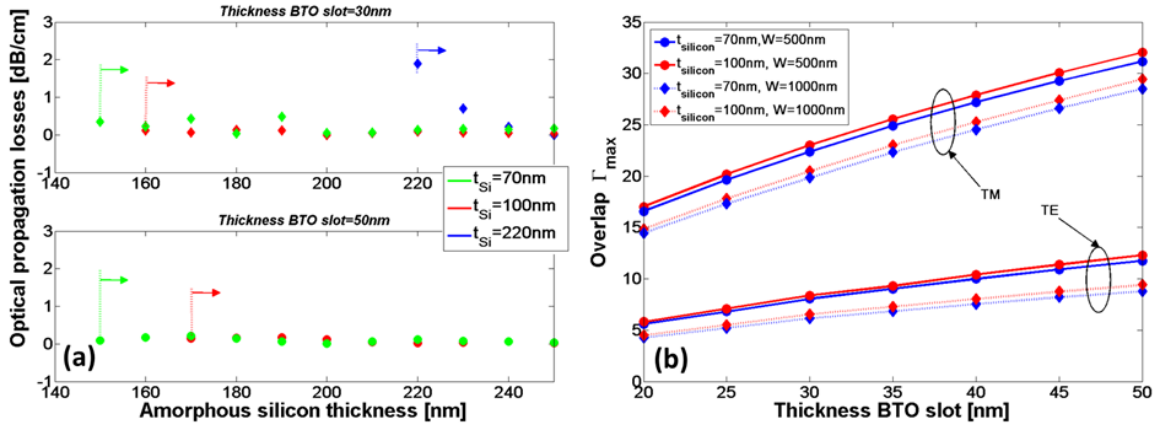


Figure 2.13: (a) Optical propagation losses as a function of a-Si thickness for different Si and BTO thicknesses (TM polarization, waveguide width of 1000 nm). Arrows represent the lowest a-Si thickness for which below 3dB/cm losses are achieved. (b) Estimation of the maximum value of overlap integral as a function of the BTO slot thickness for two different silicon thicknesses and two waveguide widths.

For this purpose, the optical propagation losses for TM polarization as a function of the a-Si layer thickness ($t_{\text{a-Si}}$) has been calculated as a function of t_{Si} for two different BTO thicknesses, namely $t_{\text{slot}}=30\text{ nm}$ and $t_{\text{slot}}=50\text{ nm}$, as shown in Figure 2.13(a). Almost negligible losses are obtained in a wide $t_{\text{a-Si}}$ range for low t_{Si} (similarly, very low losses were also obtained for TE polarization in all cases).

It must be highlighted that only the points corresponding to losses below 3dB/cm are plotted in Figure 2.13(a). When $t_{\text{Si}}=220\text{nm}$, losses below 3dB/cm can only be achieved for the thinnest BTO slot (30nm) with sufficiently thick a-Si thicknesses ($t_{\text{a-Si}}>220\text{nm}$). Figure 2.13(a) also shows that low t_{Si} values (70 or 100 nm) provides robustness of low losses operation against deviations of the a-Si thickness with respect to the nominal value, reducing the constraint on the deposition process control.

Light confinement of the fundamental mode has been analyzed by simulating the effective index change due to a uniform change of the BTO refractive index. In such a way, an upper bound of the EO overlap integral between the electric field and optical mode can be estimated. In this way, optical power confinement in the BTO layer has also been calculated, for $t_{\text{Si}}=70\text{nm}$ and 100nm and for two waveguide widths ($W=500\text{nm}$ and $W=1000\text{nm}$) as a function of the BTO thickness t_{slot} (Figure 2.13(b)). The estimated overlap integral is higher for the TM fundamental mode as expected in a horizontal slot configuration [71]. Furthermore, light confinement increases as t_{slot} increases and W becomes smaller. The halfway etched waveguide structure with a silicon (Si) thickness of 100nm and a BTO thickness of 50nm have been chosen to ensure low losses, high optical confinement and single-mode transmission.

2.1. Optical design

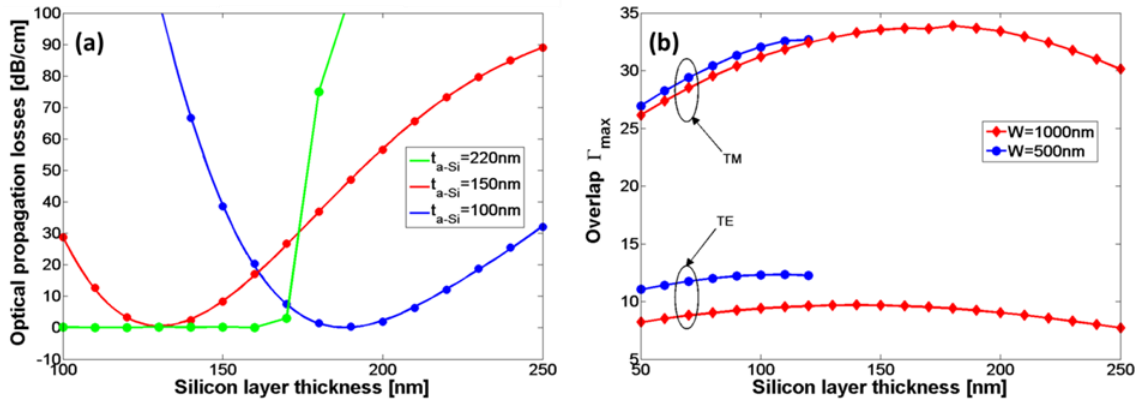


Figure 2.14: (a) Optical propagation losses as a function of silicon thickness for different amorphous silicon thicknesses, for TM polarization, $t_{\text{slot}}=50\text{nm}$ and $W=1000\text{ nm}$, (b) Estimation of the maximum value of overlap integral versus silicon layer thickness for $t_{a-Si}=220\text{nm}$, $t_{\text{slot}}=50\text{nm}$ and different waveguide widths.

Figure 2.14(a) shows the optical losses versus t_{Si} for different t_{a-Si} values for TM polarization. Negligible losses are obtained for a 220nm thick a-Si layer in a wide range of Si thicknesses. Therefore, this value has been chosen for the final HE waveguide structure. Furthermore, when plotting the overlap integral for such value of $t_{a-Si}=220\text{nm}$ versus silicon layer thickness (Figure 2.14(b)), it can be confirmed again that $t_{Si}=100\text{nm}$ is an optimum value to obtain a high light confinement in the BTO layer with negligible losses.

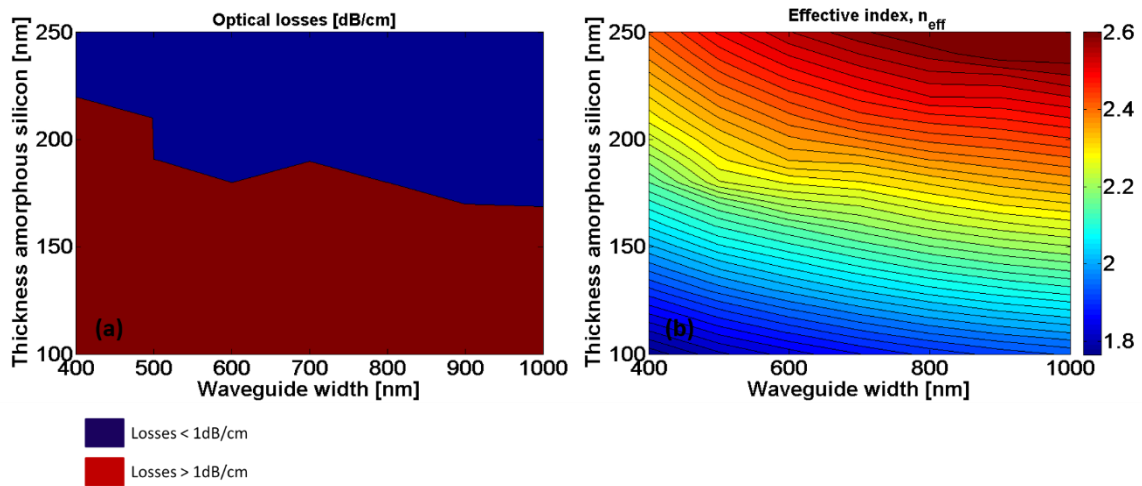


Figure 2.15: Contour of (a) optical propagation losses and (b) effective index versus amorphous silicon thickness and waveguide width, for TM polarization, $t_{Si}=100\text{nm}$ and $t_{\text{slot}}=50\text{nm}$.

The waveguide width has also been optimized to ensure single mode condition for both TM and TE polarization. Figure 2.15(a) shows the evolution of the optical losses as a function of the waveguide width and a-Si thickness for TM polarization. Single mode transmission and low losses are achieved for waveguide widths ranging from 400nm to 700nm and a-Si thicknesses ranging from 200nm to 250nm. This result confirms the suitability of 220nm amorphous silicon thickness. Low losses and single mode operation

Chapter 2: Design of electro-optic modulators based on BaTiO₃ in silicon

are achieved when the effective index of fundamental TM mode increases (Figure 2.15(b)). These results agree with those obtained for TE polarization.

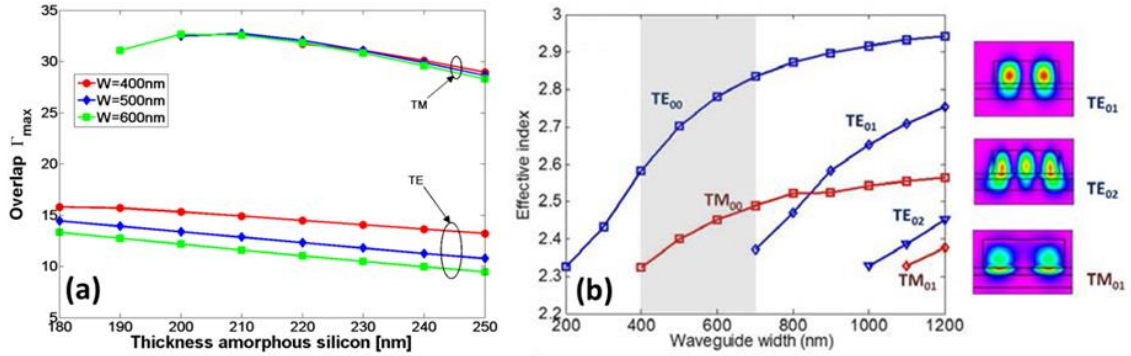


Figure 2.16: For the halfway etched structure with $t_{\text{Si}}=100\text{nm}$ and $t_{\text{slot}}=50\text{nm}$: (a) Estimation of the maximum value of overlap integral as a function of amorphous silicon thickness for waveguide widths $W=400\text{nm}$, 500nm and $W=600\text{nm}$, for which single mode operation is achieved, (b) Effective index as a function of waveguide width.

Finally, simulations have been carried out to assess the dependence of light confinement on the waveguide width. Figure 2.16(a) confirms that, for TM, a high confinement of about 32% is achieved for $t_{\text{a-Si}}=220\text{nm}$, and that the confinement does almost not depend on the waveguide width. In the case of TE polarization, the confinement increases when the waveguide width is reduced and a value between 12% and 15% is obtained for a $t_{\text{a-Si}}=220\text{nm}$ and $W=400\text{-}600\text{nm}$. Figure 2.16(b) shows the evolution of the effective index as a function of the waveguide width for the different modes of both TE and TM polarizations. The inset shows the mode profile of higher-order modes. The effective index of TM polarization is lower than that of TE polarization indicating that the mode is more confined in the BTO layer.

2.1.2.2. Fully etched waveguide

In the FE case, we conceived a symmetric structure (device with same values of Si layer thickness and a-Si layer thickness) in which the optical mode is confined in the BTO slot region. Doubtlessly, the confinement increases when the BTO thickness increases. The BTO thickness also impacts the orientation of the ferroelectric polarization in the oxide, and it must also be chosen regarding this issue. A vertical electrode configuration is used for this geometry (Figure 2.17(a)). The main drawback of the FE design is related to the fact that the top electrode placed above the a-Si layer causes high absorption losses. The challenge here is thus to conveniently design the top contact to minimize these absorption losses. However, even a semiconductor with low refractive index imaginary part like indium tin oxide, ITO ($n_{\text{ITO}}=1.6761+j0.11$), is too lossy to be placed directly on top of the a-Si. Therefore, in order to avoid high losses, a convenient spacer should be placed between a-Si and the electrode to minimize the overlap between the electro-optical field and the contact. For this purpose, we envisaged using an amorphous strontium titanate (STO) spacer, grown on top of the a-Si layer. We simulated 400 nm-wide single mode

2.1. Optical design

waveguides with silicon and a-Si both 220 nm thick, 50 nm of BTO and ITO electrodes. The lateral electrode was placed far enough (1 μm) from the waveguide edge and the ITO bottom electrode was chosen thin enough (50 nm) to minimize absorption losses.

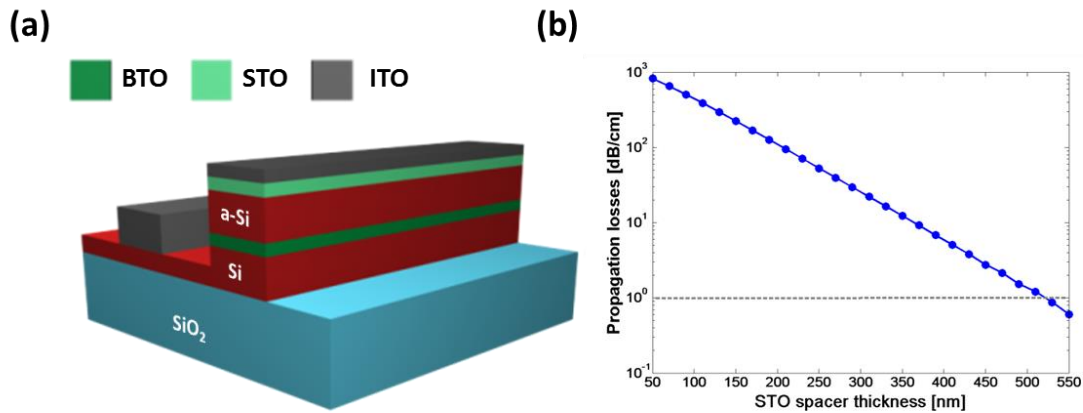


Figure 2.17: (a) Simulated FE waveguide structure. The BTO thickness is 50 nm, and the waveguide width 400 nm. The lateral ITO electrode (thickness 200 nm) is placed 1 μm away from the waveguide edge. (b) Propagation losses as a function of STO spacer thickness.

In this geometry, we calculated the optical losses as a function of the thickness of the STO spacer (with $n_{\text{STO}}=2.284$). Results are plotted in Figure 2.17(b). Acceptable propagation losses (<1dB/cm) require STO spacer thicknesses larger than 550 nm, i.e. much larger than the BTO slot thickness, which will cause significant voltage drop in the spacer layer.

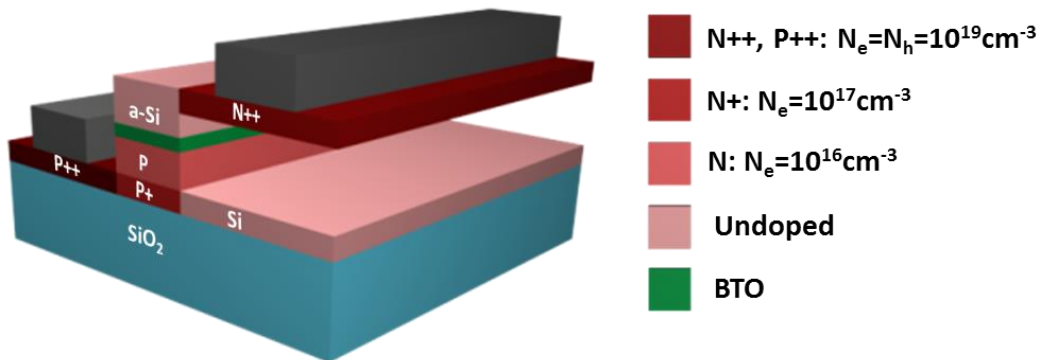


Figure 2.18: Alternative FE waveguide considered. BTO thickness is 50nm and 400nm waveguide width.

After realizing the incompatibility of this configuration, we conceived an alternative FE design consisting in an asymmetric geometry with doped silicon to minimize the mode overlap with the top electrode and thus reduce the absorption losses (Figure 2.18). In this design, the top electrode is made of N₊₊ (phosphorous implanted) polysilicon and the bottom electrode P₊₊ (boron implanted) polysilicon.

Chapter 2: Design of electro-optic modulators based on BaTiO₃ in silicon

The lower slab in the waveguide (Si-pedestal) and the bottom electrode wings could be then formed through partial silicon etching at the sides of the waveguide structure, starting from the top polysilicon, and etching through the active layer and the bottom polysilicon. Moreover, the Si-pedestal has a graded p-type doping to reduce the free carrier density in the optical mode region and therefore the losses. A 50nm Si-pedestal thickness (bottom electrode), 50 nm top polysilicon electrode and 250nm a-Si layer thickness have been optimized by simulation to obtain minimal losses. The optimized doping levels are shown in Figure 2.18. Depending on the waveguide width election, we can achieve an overlap integral (optical confinement estimation) of 28% for TM and 11.7% for TE polarization with low losses.

At the end, the FE design was discarded due to the following reasons:

- There is no enhancement in terms of optical confinement and propagation losses compared to the HE design.
- The modulator efficiency is expected to be seriously penalized due to the potential high voltage drop across the structure, caused by limitations on the maximum doping levels that can be used to enable low propagation losses.
- It is technologically more complex, especially because several ion implantation steps are required to define the doped regions.

2.1.2.3. Final waveguide structure

After the simulation work above presented, the chosen structure was the HE consisting of a thickness of 50nm combined with a-Si layer thickness of 220nm and Si layer thickness of 100nm.

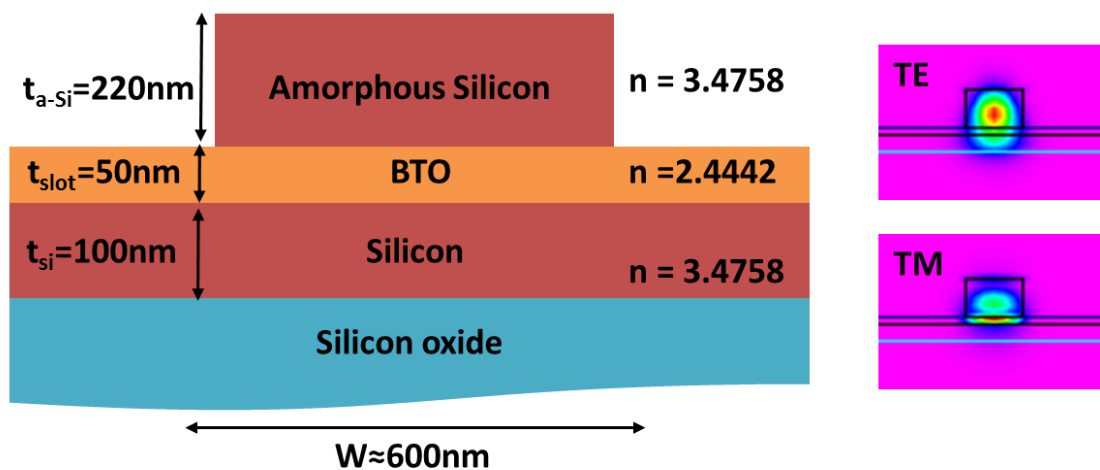


Figure 2.19: Schematic of the halfway etched waveguide with the final design parameters and the TE and TM mode profiles.

The election of these parameters allows obtaining single mode operation at $1.5\mu\text{m}$ wavelength with near 0dB/cm propagation losses (assuming that there is no sidewall roughness) and a high optical confinement of 32% for the TM mode and around 15% for

the TE mode. The optimal structure, with the final design parameters, is sketched in Figure 2.19.

2.2. Electro-Optical design

Electro-optics concerns the interaction between the electromagnetic and the electrical states of materials. In our case, the electromagnetic field of the optical mode and the electrical field applied through the electrodes by a voltage difference. As explained in chapter 1, due to the non-centrosymmetric nature of BTO, the electric field originated by the applied voltage will proportionally change its refractive index.

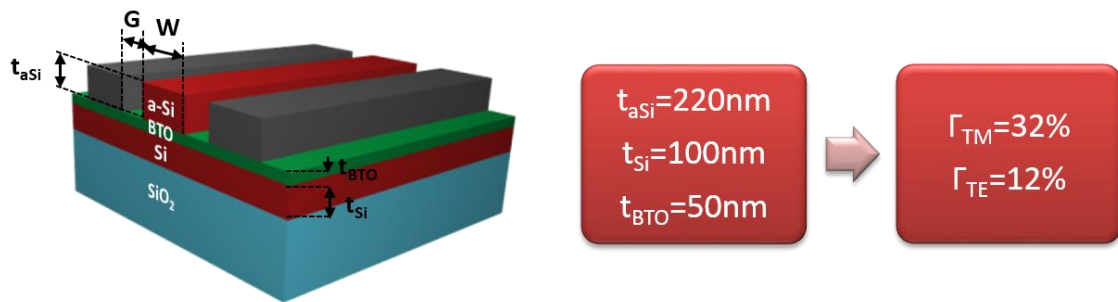


Figure 2.20: Schematic of the halfway etched waveguide with the final design parameters.

In order to apply the electric field, two electrodes placed horizontally on top of the BTO layer are envisaged (Figure 2.20). The electrode characteristics will be intrinsically connected with the DC and radio frequency (RF) performance of the modulator. In this way, the design of proper electrodes is crucial towards achieving modulation at high speed. To begin with, we studied the EO performance in DC regime.

2.2.1. Electrode design in DC regime

The electrode placing is a crucial point since it has to be far enough from the waveguide to limit absorption losses and close enough to enhance the modulation efficiency. Firstly, the effect of electrode spacing on the propagation losses was simulated. Figure 2.21 shows the propagation losses induced by the electrodes as a function of the waveguide width (W) and the waveguide-to-electrode separation (G). CMOS compatible aluminium (Al) electrodes ($n_{Al}=1.5137+j15.234$) have been utilized. It can be seen that despite having higher confinement factor than TE, TM polarization presents higher losses due to the stronger interaction between the horizontal metallic contacts and the vertically oriented electric field component of the optical mode.

Furthermore, higher losses are experienced by both polarizations when the waveguide width decreases due to lateral expansion of the optical mode. A waveguide width of

$W=600\text{nm}$ (the waveguide becomes multimode for widths above 700nm for TE polarization and 1100nm for TM polarization) and a waveguide/electrode spacing of $G=1\mu\text{m}$ lead to negligible losses for both polarizations.

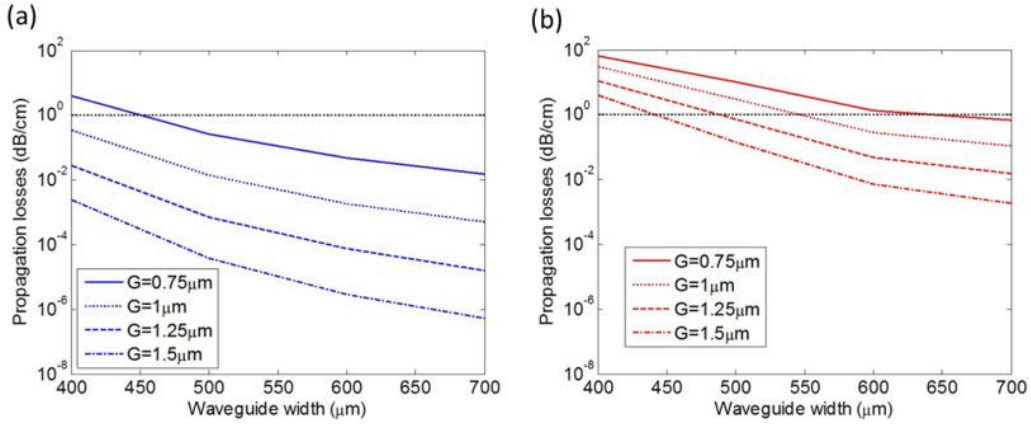


Figure 2.21: Propagation losses due to electrodes for (a) TE and (b) TM and different waveguide/electrode spacing, G . The horizontal dashed line is for 1dB/cm propagation losses.

2.2.2. Influence of single domain BaTiO₃ ferroelectric orientation

As it was introduced in chapter 1, the EO performance of the device will depend on the BTO crystal orientation with respect to the light propagation direction and electric field orientation. A BTO crystal can have its “a” axis or its “c” axis lying along the substrate and this orientation can be somehow tuned by varying the growth conditions. The simulations presented in the following assess the effect of BTO crystal orientation on the device EO performance. They are performed assuming in this section that the BTO is single domain and the design has been carried out with a commercial finite-element based mode solver [72].

2.2.2.1. EO performance for a-axis oriented BaTiO₃

Figure 2.22 shows the possible waveguide orientations with respect to the coordinate system defined by a-axis oriented BTO. The x-axis is perpendicular to the horizontal plane but the same performance would be achieved by considering the y-axis perpendicular. Two extreme cases can be initially distinguished: on one hand when the electric field is parallel to the optical axis, Figure 2.22(a), and on the other hand when the electric field is perpendicular to the optical axis, Figure 2.22(b). In the former case, it can be obtained from the ellipsoid equation introduced in chapter 1 (Eq. (1.14)) that modulation is determined by the r_{33} coefficient for TE polarization (Eq. (2.1)) and by the r_{13} coefficient for TM (Eq. (2.2)). However, in the latter, there will be no modulation, neither for TE nor for TM polarization.

2.2. Electro-optical design

$$\Delta n_{TE} = \frac{1}{2} n_e^3 r_{33} E_z \quad (2.1)$$

$$\Delta n_{TM} = \frac{1}{2} n_o^3 r_{13} E_z \quad (2.2)$$

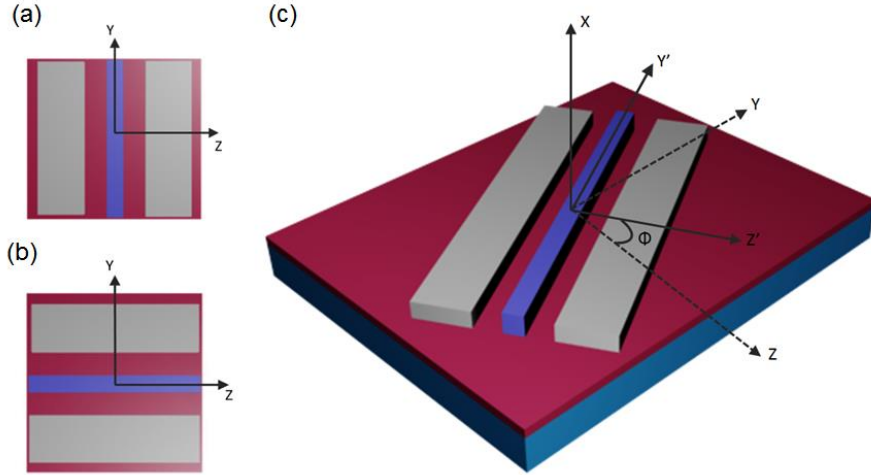


Figure 2.22: Waveguide structure for a-axis oriented BTO. The optical axis (z-axis) is in-plane in the BTO layer and can be (a) parallel or (b) perpendicular to the applied electric field. (c) The waveguide can also be rotated by an angle of ϕ in the yz plane to enhance the EO performance.

The EO performance can be enhanced by rotating the waveguide in the yz plane (around x) by a given angle ϕ , as depicted in Figure 2.22(c), to achieve an effective EO coefficient that will be a linear combination of r_{13} , r_{33} and r_{51} . To analyse the EO performance, it is more convenient to define the coordinate system along the applied electric field and the propagation of light (z' and y' axes respectively in Figure 2.22(c)). The applied electric field is mainly in the horizontal direction so it can be assumed that $E_x=0$. The index ellipsoid in the new coordinate system is obtained by using the following transformation:

$$\begin{aligned} y &= y' \cos(\phi) + z' \sin(\phi) \\ z &= -y' \sin(\phi) + z' \cos(\phi) \end{aligned} \quad (2.3)$$

By considering Eq. (1.14), the refractive index and EO coefficient can be derived for TE polarization

$$n_{z'}(\phi) = \frac{n_o n_e}{\sqrt{n_e^2 \sin^2(\phi) + n_o^2 \cos^2(\phi)}} \quad (2.4)$$

$$r_{z'}(\phi) = r_{33} \cos^3(\phi) + (r_{13} + 2r_{51}) \sin^2(\phi) \cos(\phi) \quad (2.5)$$

and for TM polarization

$$n_x = n_o \quad (2.6)$$

$$r_x(\phi) = r_{13} \cos(\phi) \quad (2.7)$$

Interestingly, the refractive index for TE polarization ranges from the ordinary to the extraordinary value when the rotation angle ranges from 0° to 90°. On the other hand, the EO coefficient as a function of the rotation angle is plotted in Figure 2.23(a). It can be seen that the maximum value is achieved for an angle of 55°. This angle is somewhat higher than the 45° value that has been previously reported in a similar waveguide structure [49, 51]. It should be noticed that this optimum angle is independent of the waveguide structure as it has been analytically derived from the index ellipsoid of BTO.

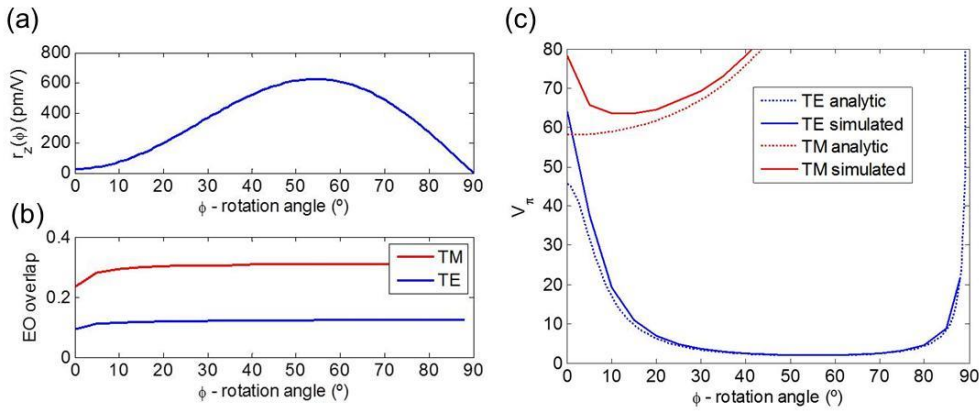


Figure 2.23: (a) EO coefficient for TE polarization, (b) EO overlap and (c) V_π voltage as a function of the rotation angle for both polarizations.

By looking at Figure 2.23(a), it is also confirmed that there will not be any index modulation for a rotation angle of 90° and, from Eq. (2.7), the same will occur for TM polarization. The maximum EO coefficient for TM polarization will be given at 0°. However, the value is much lower than for TE polarization as only r_{13} coefficient is involved.

Figure 2.23(b) shows the EO overlap integral as a function of the rotation angle for both TE and TM polarization, which has been calculated using the following equation:

$$\Gamma(\phi) = \frac{S \iint_{BTO} E_e(\phi) |E_o(\phi)|^2 dx dz'}{\iint |E_o(\phi)|^2 dx dz'} \quad (2.8)$$

where $E_e(\phi)$ and $E_o(\phi)$ are the simulated amplitudes of the electric and optical fields, respectively, at each rotation angle. It should be noticed that the permittivity of BTO will also depend on the rotation angle so that we have considered that $\epsilon_z = 2200 \cdot \sin(\phi) + 56 \cdot \cos(\phi)$ and $\epsilon_x = 2200$ [28].

The EO overlap integral will be almost constant with the rotation angle, with values $\Gamma_{TE} \approx 11\%$ and $\Gamma_{TM} \approx 29\%$. The EO overlap integral decreases at small rotation angles due to the low permittivity of the BTO at such angles. The refractive index and EO coefficients described in Eq. (2.4)-(2.7) have been used to simulate the change in the

effective index of the fundamental mode. Then, we can extract the V_π voltage of the modulator as a function of the rotation angle. Results are shown in Figure 2.23(c) for both TM and TE polarization. The V_π voltage can also be analytically calculated as

$$V_{\pi,TE}(\phi) \approx \frac{\lambda S}{\Gamma_{TE} n_z^3(\phi) r_z(\phi) L} \quad (2.9)$$

$$V_{\pi,TM}(\phi) \approx \frac{\lambda S}{\Gamma_{TM} n_o^3 r_{13} \cos(\phi) L} \quad (2.10)$$

where λ is the wavelength, S is the separation between the electrodes, L is the active length and Γ_{TE} and Γ_{TM} are the EO overlap integral for TE and TM polarization. In our case, $\lambda=1550\text{nm}$, $S=2.6\mu\text{m}$, $L=2\text{mm}$ (we consider for simulations a Mach-Zehnder interferometer modulator in which the active arm, with 2mm of length, is formed by the HE waveguide structure), $\Gamma_{TE}=11\%$ and $\Gamma_{TM}=29\%$.

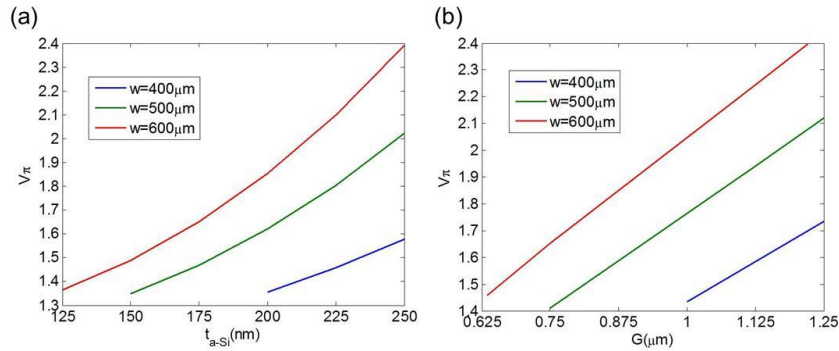


Figure 2.24: V_π voltage for TE polarization and $\phi = 55^\circ$ as a function of (a) the amorphous silicon thickness and $G=1\mu\text{m}$ and (b) the waveguide-to-electrode separation and $t_{\text{a-si}}=220\text{nm}$. Results are shown for different waveguide widths.

The V_π voltages calculated by Eq. (2.9)-(2.10) have also been plotted in Figure 2.23(c). It can be seen that there is a very good agreement between simulation and analytic results except for smaller rotation angles where the EO overlap integral decreases and therefore the assumption of a constant value is no longer valid. The optimum EO performance is obtained for TE polarization and a rotation angle of 55° , in agreement with Figure 2.23(a), for which a V_π voltage as low as 2V is achieved.

For TM polarization, although the overlap integral is almost two times higher due to the stronger optical confinement, a drastically higher V_π voltage of 64V is obtained at the optimum angle around 10° due to its low Pockels coefficient involved.

The influence of the amorphous silicon thickness, waveguide width and waveguide-to-electrode separation on the EO performance has also been analysed via simulations for TE polarization and the optimum rotation angle. Figure 2.24(a) shows the V_π voltage as a function of the amorphous silicon thickness, $t_{\text{a-si}}$, for different waveguide widths. It can be seen that a V_π voltage as low as 1.35 V ($V_\pi \cdot L = 0.27\text{V} \cdot \text{cm}$) can be achieved by using thinner amorphous silicon layers. However, there is a minimum thickness that cannot be

Chapter 2: Design of electro-optic modulators based on BaTiO₃ in silicon

exceeded to avoid losses. Furthermore, the minimum thickness, which has been chosen to ensure propagation losses below 1dB/cm, will depend on the waveguide width. Wider waveguides with higher effective indices allow using thinner amorphous silicon layers. However, it can be seen in Figure 2.24(a) that the minimum achievable V_π voltage is almost the same independently of the waveguide width. Wider waveguide should be preferred to minimize additional propagation losses due to sidewall roughness. Figure 2.24(b) shows the V_π voltage as a function of G for different waveguide widths and taking into account an amorphous silicon thickness of 220nm. Electrodes can be placed closer to wider waveguides, as shown in Figure 2.21(a), and hence the V_π voltage can be decreased. Nonetheless, there is a lower bound in the minimum waveguide-to-electrode separation in this case to avoid losses due to the interaction of the optical mode with the metallic contacts. The interesting point is that there will also be a minimum achievable V_π voltage independently of the waveguide width. Therefore, the optimum EO performance can be achieved independently of the waveguide width by optimizing the amorphous silicon thickness and waveguide-to-electrode separation.

2.2.2.2. EO performance for c-axis oriented BaTiO₃

The waveguide structure is sketched in Figure 2.25(a) for c-axis oriented BTO. In this case, the optical axis (z-axis) is perpendicular to the horizontal plane.

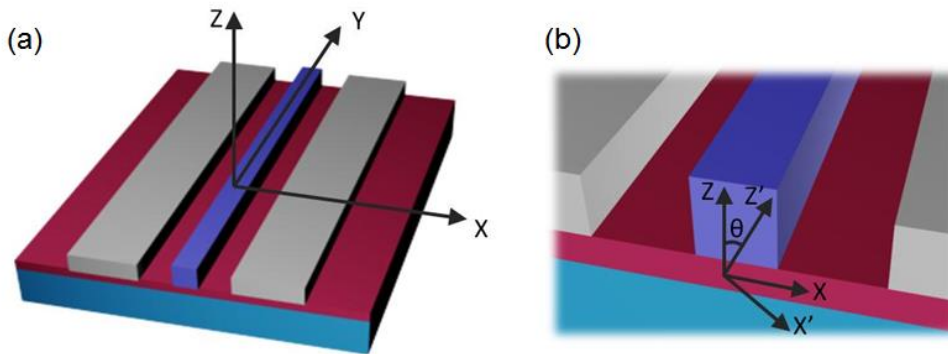


Figure 2.25: Waveguide structure for c-axis oriented BTO. (a) The optical axis (z-axis) is out-of-plane in the BTO layer, (b) However, there is a rotation in the xz plane (θ -angle) when a voltage is applied in the electrodes.

However, with the application of an electric field, the index ellipsoid is rotated around the y -axis and therefore the principal axes in the transversal plane are no longer aligned with the waveguide structure, as depicted in Figure 2.25(b). The angle between the rotated $x'z'$ and the original xz coordinates can be derived from the ellipsoid index equation (Eq. (1.14)):

$$\theta = \frac{1}{2} \operatorname{atan} \left(\frac{2r_{51}V}{S \left[\frac{1}{n_e^2} - \frac{1}{n_o^2} \right]} \right) \quad (2.11)$$

Assuming the applied electric field is mainly in the x-axis, we can therefore accept $E_z=E_y=0$. On the other hand, unlike what happens for a-axis oriented BTO, the rotation of the waveguide in the xy plane will not affect the EO performance.

Figure 2.26(a) shows the induced rotation angle of the BTO principal axes in the transversal plane as a function of the applied voltage and for different waveguide-to-electrode separations. The induced rotation will affect the optical signal by rotating the input polarization. This undesired effect can be neglected if the V_π voltage is small enough to minimize the induced rotation. Furthermore, smaller V_π voltages will be required if the waveguide-to-electrode separation is decreased, as depicted in Figure 2.26(a).

The variation of the refractive indices as a function of the applied electric field will be as follows:

$$\Delta n_{TE} = \frac{n_o^3 r_{51}^2 E_x^2}{2 \left(\frac{1}{n_e^2} - \frac{1}{n_o^2} \right)} \quad (2.12)$$

$$\Delta n_{TM} = -\frac{n_e^3 r_{51}^2 E_x^2}{2 \left(\frac{1}{n_e^2} - \frac{1}{n_o^2} \right)} \quad (2.13)$$

The V_π voltage for TE and TM polarizations can be derived from Eq. (1.14) as

$$V_{\pi,TE} = \sqrt{\frac{\left(\frac{1}{n_e^2} - \frac{1}{n_o^2} \right) \lambda S^2}{\Gamma_{TE} n_o^3 r_{51}^2 L}} \quad (2.14)$$

$$V_{\pi,TM} = \sqrt{\frac{\left(\frac{1}{n_e^2} - \frac{1}{n_o^2} \right) \lambda S^2}{\Gamma_{TM} n_e^3 r_{51}^2 L}} \quad (2.15)$$

when low θ -angle values ($\theta < 10^\circ$) are considered. The square root causes a non-linear phase shift variation with the applied voltage, as it is shown in Figure 2.26(b). It should also be noticed that the phase shift will be positive ($n_{TM} < 0$) for TM polarization but negative ($n_{TE} > 0$) for TE polarization.

The absolute value of the simulated phase shift has been compared in Figure 2.26(b) with the one calculated analytically by assuming a constant electric field, $E_x=V/S$, and

Chapter 2: Design of electro-optic modulators based on BaTiO₃ in silicon

the maximum achievable overlap integral previously obtained. In this case, BTO permittivity is $\epsilon_x=2200$ and $\epsilon_z=56$. It can be seen that there is a good agreement between both results thus indicating an efficient EO performance. The V_π voltage is smaller for TM ($V_\pi=4.5V$) than for TE ($V_\pi=7.2V$) due to the higher optical mode confinement in the BTO layer. However, the same waveguide-to-electrode separation ($G=1\mu m$) as well as amorphous silicon thickness ($t_{aSi}=220nm$) have been considered for both polarizations. From (Eq. (2.14)-(2.15)), the V_π voltage of TE and TM polarization can be related as:

$$\frac{V_{\pi,TM}}{V_{\pi,TE}} \approx \frac{S_{TM}}{S_{TE}} \sqrt{\frac{\Gamma_{TE}}{\Gamma_{TM}}} \quad (2.16)$$

assuming that the ordinary and extraordinary indices have a comparable value ($n_o \approx n_e$). This expression indicates that the lower overlap integral for TE ($\Gamma_{TM} > \Gamma_{TE}$) could be compensated by using a smaller electrode separation ($S_{TE} < S_{TM}$) thus yielding to lower V_π voltages.

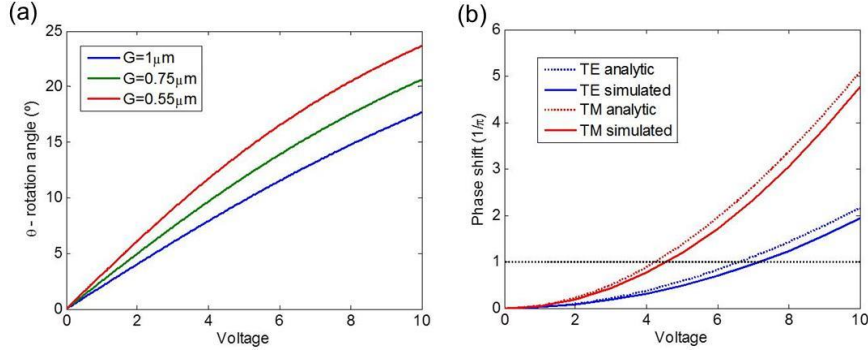


Figure 2.26: (a) Rotation angle of the BaTiO₃ principal axes as a function of the applied voltage and for different waveguide-to-electrode separations, (b) Absolute simulated and analytic phase shift for both polarizations as a function of the applied voltage for $G=1\mu m$.

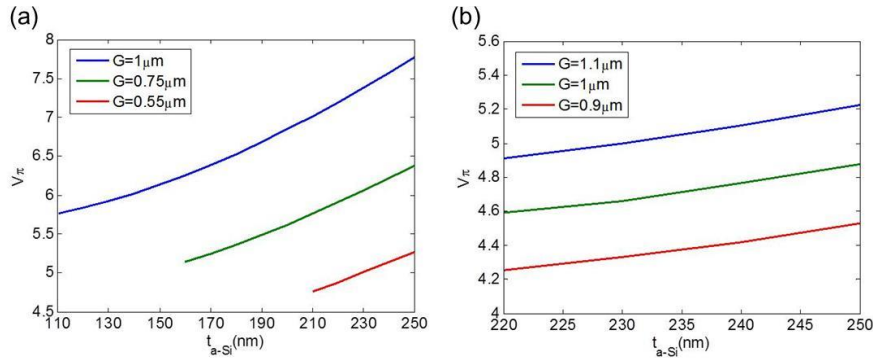


Figure 2.27: V_π voltage for (a) TE and (b) TM polarizations as a function of the amorphous silicon thickness taken into account different waveguide-to-electrode separations and a waveguide width of 600nm.

Finally, Figure 2.27 compares the V_π voltage for (a) TE and (b) TM polarization by changing the amorphous silicon thickness and waveguide-to-electrode separation. It can be seen that a larger improvement can be achieved for TE polarization by optimizing

2.2. Electro-optical design

these parameters. Furthermore, the impact of minimizing the waveguide-to-electrode separation is stronger than that of decreasing the amorphous silicon thickness.

Therefore, the lowest V_π value for TE polarization 4.75V, has been achieved by reducing the waveguide-to-electrode separation to 550nm and using a slightly lower amorphous silicon layer thickness of 210nm. The limit for each configuration has also been determined for having propagation losses below 1 dB/cm. Nevertheless, it should be noticed that the polarization rotation effect will be more accentuated for smaller waveguide-to-electrode separations, as it was shown in Figure 2.16(a). However, this effect will be almost negligible due to the low V_π voltages achieved. In the case of TM polarization (Figure 2.27(b)), the amorphous silicon thickness cannot be decreased below 220nm to avoid losses. Nonetheless, the waveguide-to-electrode separation can be decreased to 900nm to improve the V_π voltage.

To conclude, the optimum BaTiO₃ ferroelectric domain orientation to enhance EO modulation in a silicon CMOS compatible waveguide structure has been investigated via simulations. Furthermore, the expressions to calculate the V_π voltage have also been derived for both BTO orientations and light polarizations. Thereby, all possible cases have been analyzed and compared in order to design the optimum modulation structure.

	WG Rotation angle	Polarization	V_π [V]	W [nm]	G [μ m]	t_{aSi} [nm]
a-axis	55°	TE	1.35	400	1	220
c-axis	0°	TM	4.25	600	0.9	220
	0°	TE	4.75	600	0.55	210

Table 2.2: Main design parameters obtained from simulations to achieve the minimum halfway voltage for each orientation of BaTiO₃.

Assuming fixed values of, $L=2$ mm, $t_{Si}=100$ nm and $t_{BTO}=50$ nm, Table 2.2 summarizes the lowest achievable V_π values as well as the corresponding amorphous silicon thickness, waveguide width and waveguide-to-electrode separation for both a-axis and c-axis BTO orientation. In principle, according to simulations, and assuming a single ferroelectric domain, a-axis oriented BaTiO₃ for TE polarization is the most suitable option to achieve the lowest V_π .

2.2.3. Influence of multi-domain BaTiO₃ ferroelectric orientation

In the previous section, the optimum BTO ferroelectric domain orientation to enhance the EO modulation was analyzed assuming a single domain orientation, achieving a theoretical a $V_\pi \cdot L$ as low as 0.27V·cm..

Chapter 2: Design of electro-optic modulators based on BaTiO₃ in silicon

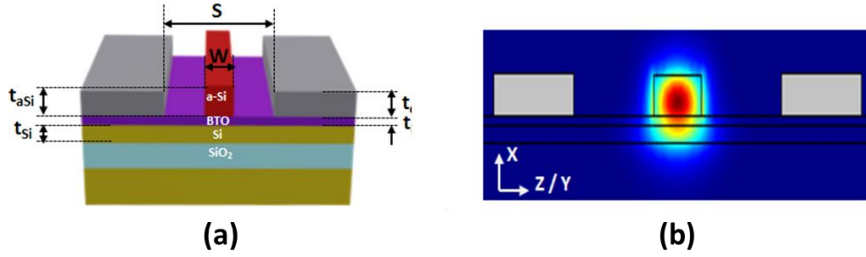


Figure 2.28: (a) Schematic of the waveguide cross-section and (b) fundamental mode profile for TE polarization at a wavelength of $1.55 \mu\text{m}$.

However, during the fabrication of thin-film BTO layers a multi-domain structure is usually formed [46, 47]. In the present study, we carefully analyze the influence of the multi-domain structure, as well as the waveguide rotation angle, on the EO modulation performance.

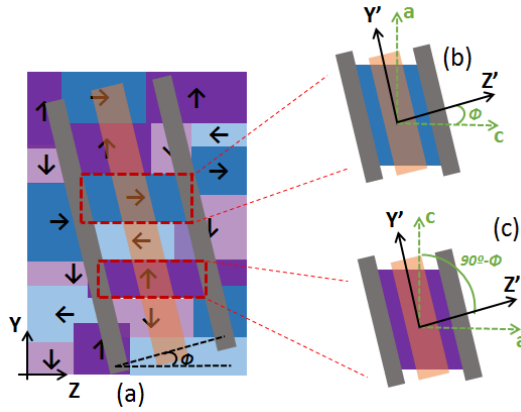


Figure 2.29: (a) Top view schematic of the optical waveguide with electrodes rotated by a certain angle, ϕ , which is defined with respect to the z-axis. The influence of the multi-domain BTO structure is analyzed by separately considering (b) 0° and (c) 90° domains. The arrow indicates the spontaneous polarization present in the tetragonal form of BTO which is parallel to its crystallographic c-axis.

Figure 2.29(a) shows a top view of the rotated waveguide with the rotation angle, ϕ , defined with respect to the z-axis. Four in-plane domain variants, with their polarization directions represented by arrows, can be distinguished in a-axis oriented BTO films. It is assumed that domains along the optical waveguide do not change their orientation in the z direction. In order to analyze the influence of the multi-domain BTO structure, the so-called 0° domains (see Figure 2.29(b)) and 90° domains (see Figure 2.29(c)) must be separately considered.

Focusing on 0° domains and initially considering that there are not antiparallel domains along the optical waveguide, the index ellipsoid when the waveguide is rotated can be obtained by applying a transformation from the original zy coordinate system to a new $z'y'$ coordinate system, which is defined along the applied electric field and the propagation of light. Thereby, the EO coefficient and BTO refractive index can be derived for TE polarization as:

2.2. Electro-optical design

$$r_z'(\phi) = r_{33} \cos^3(\phi) + (r_{13} + 2r_{51}) \sin^2(\phi) \cos(\phi) \quad (2.17)$$

$$n_z'(\phi) = \frac{n_o n_e}{\sqrt{n_e^2 \sin^2(\phi) + n_o^2 \cos^2(\phi)}} \quad (2.18)$$

From Eq. (2.17), the EO coefficient assuming a randomly mixed BTO domain distribution can be modelled by the following equation:

$$r_{eff}(\phi, \alpha) = r_z'(\phi) + \alpha [r_z'(90^\circ - \phi) - r_z'(\phi)] \quad (2.19)$$

where α is related to the orientation of the domains, taking values between 0 (all domains 0° oriented) and 1 (all domains 90° oriented). A similar expression can be derived from Eq. (2.18) to calculate the BTO refractive index, $n(\phi, \alpha)$, in the presence of mixed domains. The presence of a multi-domain structure will give rise to an optimum rotation angle of the optical waveguide to have the highest effective Pockels response depending on the α parameter.

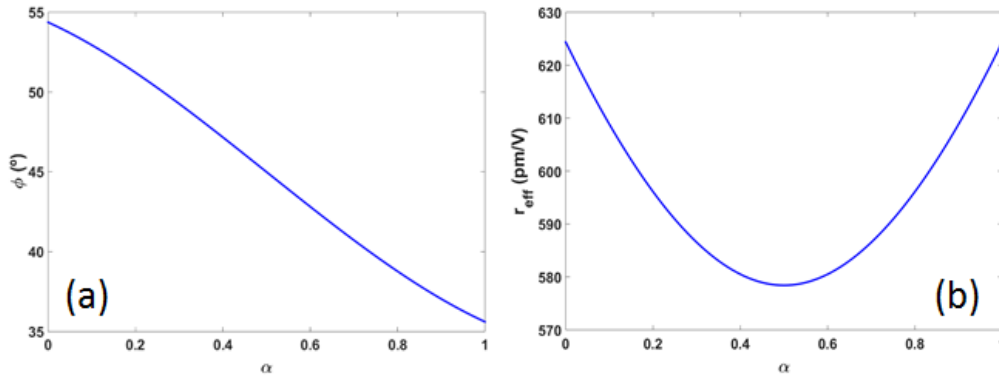


Figure 2.30: a) Optimum rotation angle to have (b) the highest Pockels coefficient depending on the mixed BTO domain distribution (α parameter).

Figure 2.30 shows the obtained results. The optimum angle shifts from 35° for $\alpha=1$ to 55° for $\alpha=0$, obtaining the highest value of $r_{eff}=624$ pm/V in both cases. Furthermore, for equally-mixed domain variants, i.e. for 50% of 0° and 90° domains ($\alpha=0.5$), a local minimum can be seen in Figure 2.30(b).

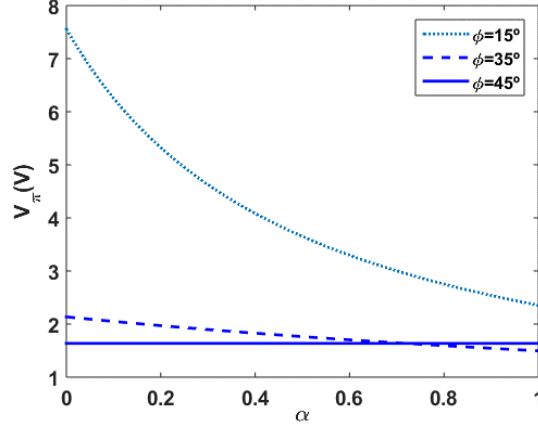


Figure 2.31: V_{π} voltage as a function of α parameter for three different rotation angles of the optical waveguide.

Nonetheless, the effective Pockels coefficient remains high ($r_{\text{eff}}=578\text{pm/V}$). The refractive index and EO coefficient have been used to analyze the influence of the multi-domain structure on the V_{π} voltage of the modulator for different rotation angles of the optical waveguide. In a Mach-Zehnder modulator, the V_{π} voltage can be analytically estimated as:

$$V_{\pi,TE}(\phi, \alpha) \approx \frac{\lambda S}{\Gamma_{TE} n^3(\phi, \alpha) r_{\text{eff}}(\phi, \alpha) L} \quad (2.20)$$

where λ is the wavelength, S is the separation between the electrodes, L is the active length and Γ_{TE} is the EO overlap integral for TE polarization. In our case, the active length has been fixed to $L=2\text{mm}$, $\lambda=1550\text{nm}$, $S=2\mu\text{m}$ and $\Gamma_{TE}=11.66\%$.

Figure 2.31 shows the V_{π} voltage as a function of α parameter for three different rotation angles. It can be seen that the lowest V_{π} voltage (below 1.5V) is achieved for the optimum rotation angle of $\phi=35^\circ$, which provides the highest Pockels coefficient but only when most of the domains are 90° oriented ($\alpha \approx 1$).

However, the V_{π} voltage increases when more 0° domains are present. On the contrary, it is interesting to notice that for a rotation angle of $\phi=45^\circ$, the V_{π} voltage has a constant value of 1.64V and it does not depend on α parameter and therefore on the in-plane domain structure. This behaviour can be easily proved by looking at Eq. (2.19) and implies that a higher robustness in the EO performance will be achieved at the expense of a small penalty on the V_{π} voltage due to a slightly smaller effective Pockels coefficient. On the other hand, when the rotation angle is far away from 45° , there is a large dependence of the V_{π} voltage with respect to the multi-domain structure, as it can be clearly seen in Figure 2.31 for $\phi=15^\circ$.

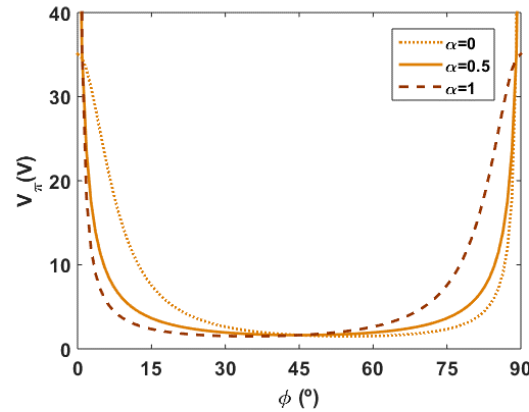


Figure 2.32: V_π voltage as a function of the rotation angle for different BTO domain distributions (α parameter).

Figure 2.32 depicts the V_π voltage as a function of the rotation angle of the optical waveguide for different BTO domain distributions. The lowest V_π voltage for $\alpha=0$ (0° domains) is found at rotation angles above 45° while for $\alpha=1$ (90° domains) is obtained at rotation angles below 45° . However, it can be seen that these low V_π voltages will drastically increase for rotation angles below 15° or above 75° .

Furthermore, it can also be clearly observed that the dependence of the V_π voltage with the BTO domain distribution significantly increases when the rotation angle is not close to 45° , as it was also shown in Figure 2.31.

Results shown in Figure 2.30, Figure 2.31 and Figure 2.32 have been obtained considering that antiparallel domains are not present independently of the α parameter. However, it can be deduced from Eq. (2.17) that the EO coefficient will have a different sign in antiparallel domains. Therefore, the phase shift accumulated by the optical mode will be cancelled when travelling through antiparallel domains (see Figure 2.29(a)). This effect can be simply modelled as a reduction of the effective active length. From Eq. (2.20), a lower active length will be proportional to an increase of the V_π voltage. In the proposed modulator, a percentage of antiparallel domains as high as 66% of the total number of domains present across the active length can be supported to keep the V_π voltage below 5V.

In summary, the influence of the multi-domain structure on the EO performance has been analyzed. Comparing to the single domain study for a-axis oriented BTO (see section 2.2.1.), the EO performance is clearly reduced. Although the variability of the V_π values as a function of the rotated angle of the waveguide is important, we have ensured that at an angle of 45° the EO performance remain constant, independently of the a-axis domain distribution that forms the structure.

The case of a multi-domain structure for c-axis oriented BTO has not been under study because of its simplicity, since there are only two kinds of domain variants and antiparallel domains cancel each other.

2.3. RF design

The main objective of an EO modulator is to transfer data at high velocity rates. For this purpose, we need to modulate at high frequency and therefore a suitable RF design becomes decisive.

In the radio frequency field, the most common nominal impedance value is 50Ω. The reason of this value resides in the compromise between maximum handling power and lowest attenuation. The RF electric signal generates an electromagnetic wave which is spread through the electrodes in the direction of the optical beam. Ideally, if the phase velocities of the RF signal and optical wave are perfectly matched, an efficient modulation could be carried out even at high frequencies.

The difference between both RF and optical signals gives us the theoretical EO bandwidth Δf assuming a RF lossless medium [73]:

$$\Delta f = \frac{2c}{\pi L(n_m - n_o)} \quad (2.21)$$

where c is the velocity of light in the vacuum, L is the length of the modulator, n_m is the microwave index and n_o the group index.

Therefore, to fully exploit the enormous capabilities of BTO, we have to carefully design the optimum electrodes to ensure RF impedance matching with low RF losses, high modulation efficiency (i.e. low $V_{\pi} \cdot L$) and high EO bandwidth.

For this end, we envisaged a design of the electrodes by placing them directly on top of the BTO layer, as previously described in the HE structure. In this way we focused on enhancing the EO effect. For the RF analysis it has been considered purely a-axis single domain BTO at a rotation angle of the waveguide of 55°. The modulator structure used in this design consisted of a MZM of 2mm length.

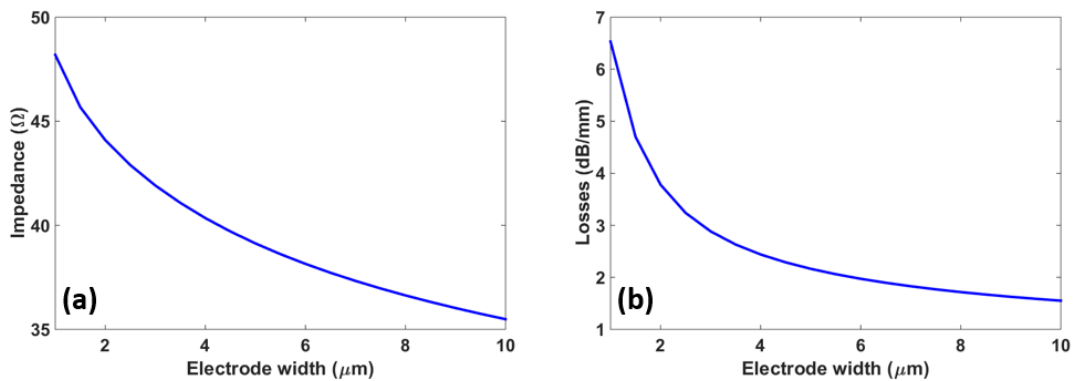


Figure 2.33: Influence of the electrode width on the (a) impedance and (b) RF losses.

In order to select suitable electrodes, the influence of the electrode width on the impedance and RF losses was simulated. The obtained results, depicted in Figure 2.33, show a clear trade-off between obtaining low RF losses and impedance around 50Ω . Therefore, an electrode width of $2\mu\text{m}$ was selected to achieve a good compromise between both values.

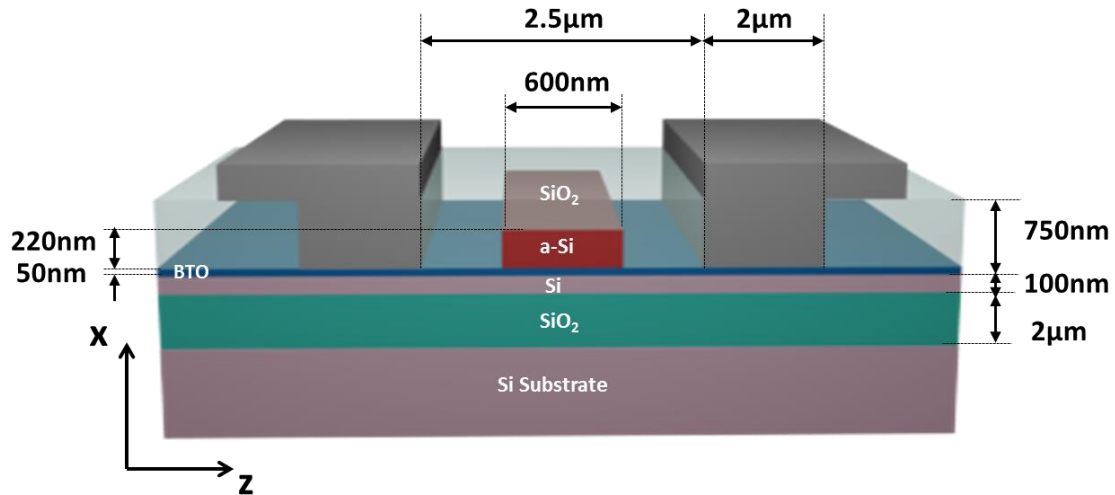


Figure 2.34: Schematic of the waveguide cross-section.

The characteristic parameters of the simulated structure are depicted in Figure 2.34. Usually, a SiO₂ layer is deposited over the optical waveguide to protect the device and lateral windows are opened to place the electrodes on top of the BTO layer thus enhancing the modulation efficiency.

The high permittivity of BTO ($\epsilon_z \sim 56$, $\epsilon_x \sim 2200$) reduces the RF impedance in comparison with usually lower dielectric constant. In such a way, the electrode dimensions have been designed to overcome the high permittivity of BTO. For that purpose, symmetric coplanar electrodes, as depicted in Figure 2.34, were chosen to achieve the matching impedance around 50Ω maintaining a narrow gap of $2.5\mu\text{m}$ in the optical waveguide with the aim of keeping the modulation efficiency as high as possible.

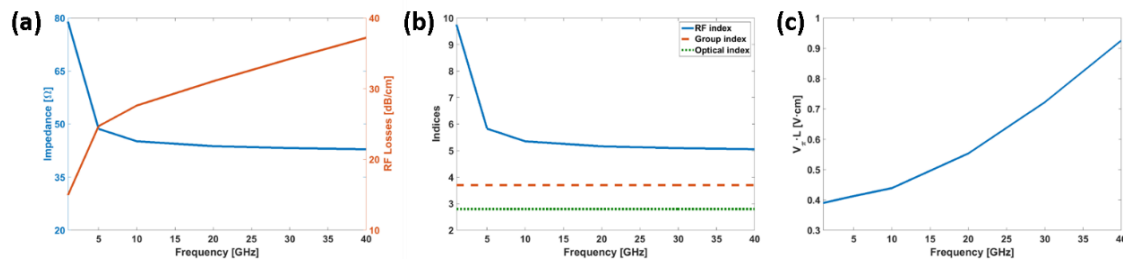


Figure 2.35: (a) RF impedance and RF losses, (b) RF and optical group indices and (c) modulation efficiency as a function of the frequency.

Figure 2.35(a) shows the impedance and RF losses, where an impedance around 50Ω and low RF losses were obtained. Figure 2.35(b) depicts the effective and optical group indices as a function of the frequency. Our results show an EO bandwidth higher than 40

Chapter 2: Design of electro-optic modulators based on BaTiO₃ in silicon

GHz, ensured as a result of the velocity matching between the electrical and optical signals (Eq. (2.21)). The modulation efficiency variation with the RF frequency is shown in Figure 2.35(c). The $V_{\pi} \cdot L$ product is below $1\text{V} \cdot \text{cm}$ in the 40 GHz frequency range.

Chapter 3

Fabrication and characterization of electro-optic modulators based on BTO in silicon

3.1. General approach to develop photonics structures

The methodology followed during this work takes part in three different phases: design, sample fabrication and experimental characterization. These three phases are connected as depicted in Figure 3.1. The first step was the design through simulation work and the analysis of different waveguide structures based on BTO on silicon, previously shown in chapter 2. Concurrently, it was carried out the development and optimization of the fabrication processes which placed restrictions in the design phase, for which a continuous feedback between the three stages was necessary during the project.

The fabrication was developed at the facilities of three different groups: the Nanophotonic Technology Center (NTC) of the Universitat Politècnica de València together with the National Institute of Lyon and the investigation group of IBM Research-Zurich Laboratory, both experts in the deposition of BTO on silicon. Then, the fabricated samples were characterized at NTC facilities and this constant feedback between all partners was crucial to obtain the electro-optic (EO) modulation results that here are presented.

3.2. BTO fabrication techniques

For the fabrication of active devices, the following general approach was followed, which relies on three main blocks:

- Design/fabrication/characterization of a-Si/SOI waveguides.
- Design/fabrication/characterization of a-Si/BTO/SOI waveguides.
- Design/fabrication/characterization of active devices exploiting the EO effect in BaTiO₃.

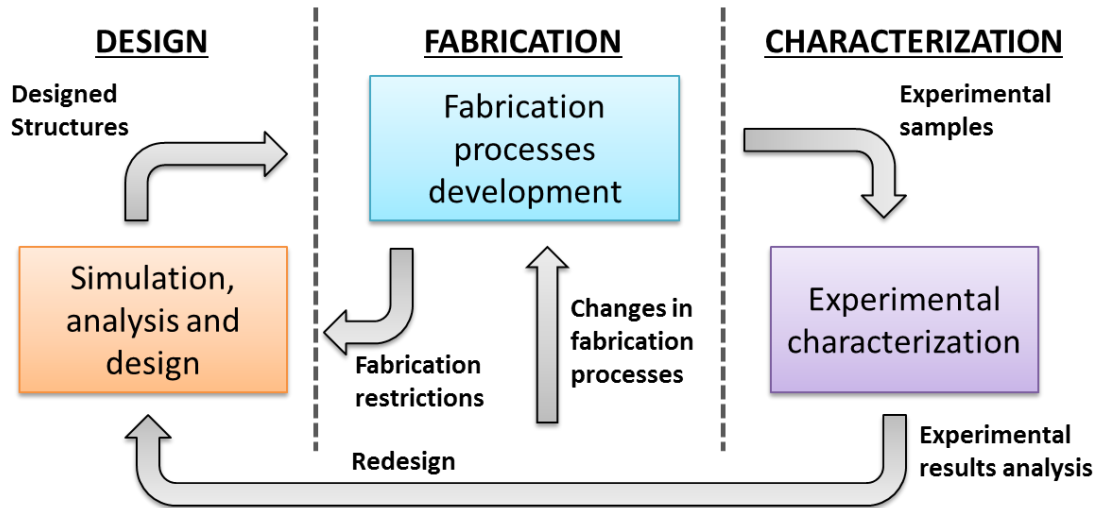


Figure 3.1: Methodology followed during this work.

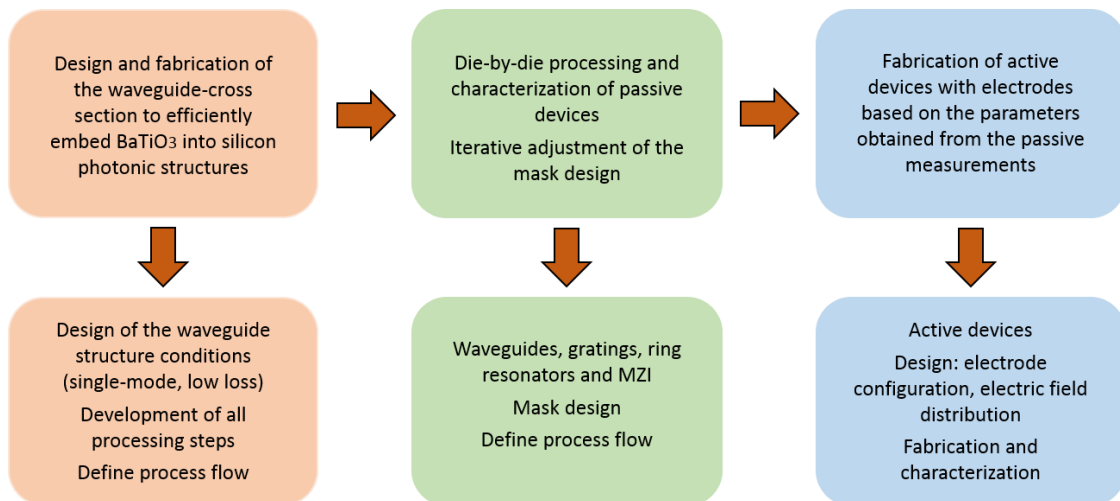


Figure 3.2: Route for the fabrication of active devices.

3.2. BTO fabrication techniques

As mentioned in chapter 1, this thesis is framed in the SITOGA project. Within the SITOGA consortium, IBM and INL partners were responsible of the BTO fabrication due to their experience and equipment. Therefore, as the work done in this thesis is not involved in BTO fabrication technique, in this chapter is shown a brief description of the

different fabrication processes that were used: radio frequency (RF) sputtering by INL and molecular beam epitaxy (MBE) by IBM. In both techniques, before BTO deposition, a thin layer of STO was grown by MBE to mitigate the mismatch between the lattice parameters of BTO and Si.

3.2.1. RF sputtering

The sputtering process, firstly discovered in 1852, and developed as a thin film deposition technique by Langmuir in 1920 [74], is a method which involves the physical removal from a target and the formation of a thin layer of the withdrawn material on a substrate by applying high-velocity particles. The process takes part in a plasma where the ions are accelerated towards the target and therefore, the bombardment allows the atoms of the target to be discharged and collected at the surface of the substrate. The most common technique for growing thin films by sputter deposition is by using a magnetron source, and depending on how the magnetron is powered, we can classify a large variety of methods like direct current (DC), pulsed DC, radio frequency (RF) or high power impulse magnetron sputtering [75].

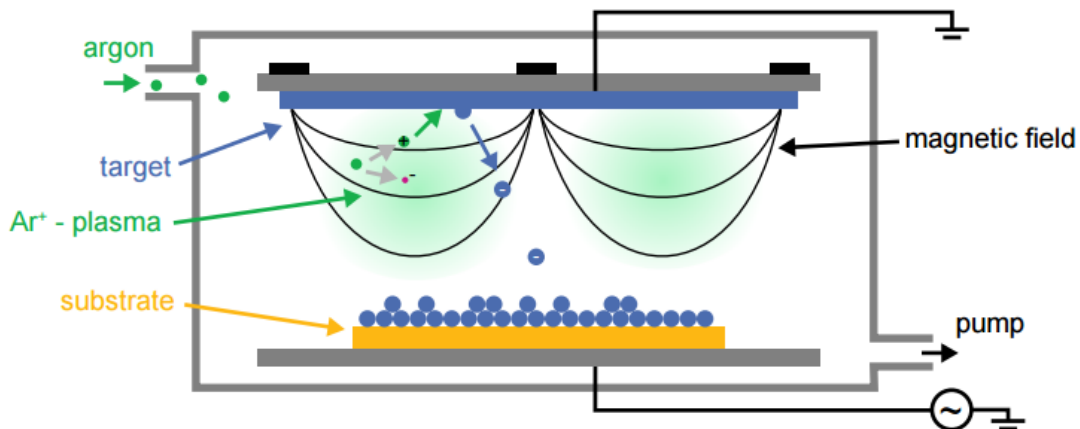


Figure 3.3: Illustration of RF-sputtering system. *Courtesy of Stefan Abel [77].*

More concretely, RF sputtering is the technique characterized by alternating the electrical potential of the current in the vacuum at radio frequencies. The main advantage of this method is to avoid the charge build up that can occur when insulating materials are sputtered, resulting in a deterioration of the film quality [76]. The sputtering process is illustrated in Figure 3.3.

3.2.2. Molecular Beam Epitaxy

The Molecular Beam Epitaxy (MBE) technique was developed in 1968 at Bell Laboratories [78]. This broadly used deposition method allows growing high quality epitaxial films in a precise and carefully controlled way. The conditions are quite strict, since there is need to dispose of a very clean environment with very low pressures in the ultra-high vacuum (UHV) regime [77].

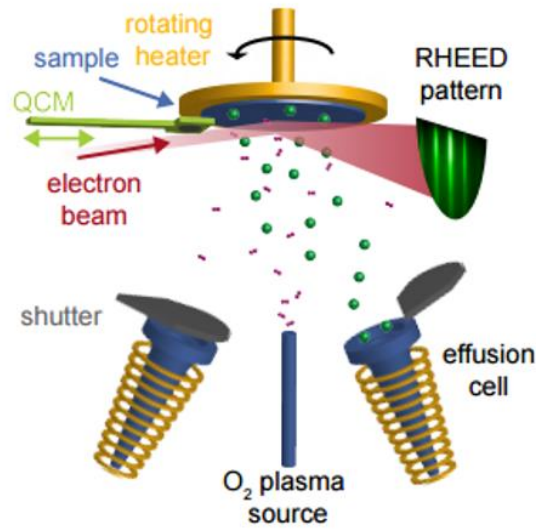


Figure 3.4: Illustration of MBE growing technique. *Courtesy of Stefan Abel [77].*

In this process, the substrate (silicon in our case) is heated up some hundreds of degrees. Thereupon, precise beams of atoms or molecules are thrown at the substrate from effusion cells in gas form. The molecules land on the surface of the substrate and after condensing, they are built up very slowly in ultra-thin layers [79]. Figure 3.4 illustrates MBE process.

3.3. Low loss amorphous silicon

In this section we describe the process followed towards achieving amorphous silicon (a-Si) with low propagation losses on BTO/SOI wafers. In this way, the first step consisted in developing the deposition of a-Si on SiO₂.

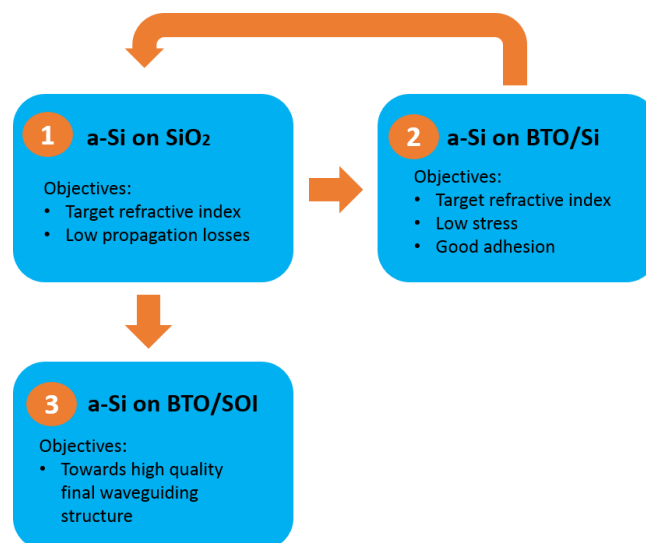


Figure 3.5: Processes followed to optimize a-Si deposition on BTO/SOI.

Chapter 3: Fabrication and characterization of electro-optic modulators based on BaTiO₃ in silicon

Once a refractive index around 3.47 and relatively low losses were achieved, the next step was to use the same recipe to deposit a-Si on BTO on silicon with the aim of obtaining again a suitable value of the refractive index and good adhesion. Due to the fact that BTO was grown on Si, we used the same a-Si recipe successfully accomplished on BTO to deposit a-Si on SiO₂ to test propagation losses. The summary of the processes followed is depicted in Figure 3.5.

Process name	Process Conditions	Sample	n_{a-Si}	α_{TE}	α_{TM}	Comments
NTC1	SiH ₄ : 100 sccm N ₂ : 1500 sccm T= 200°C P= 4.6 Torr	#1	N/A	30dB/cm	-	High roughness
		#2	N/A	15dB/cm	-	Improved etching process
		#3	N/A	10dB/cm	-	Improved etching process
		#4	2.237	<10dB/cm	>50dB/cm	Wider waveguide in GDS file
NTC2	SiH ₄ : 550sccm N ₂ : 500 sccm T= 200°C P= 2.2 Torr	#1	2.697	15dB/cm	<10dB/cm	Reduction of N ₂ plasma gas
NTC3	SiH ₄ :80 sccm H:260 sccm T= 350°C P= 4.6 Torr	#1	3.534	18dB/cm	<10dB/cm	Change to H plasma gas

Table 3.1: Evolution in the optimization of the a-Si deposition process at NTC. α_{TE} and α_{TM} are propagation losses for TE and TM polarizations respectively. n_{a-Si} is the refractive index of the amorphous silicon layer.

The deposition of a-Si by plasma-enhanced chemical vapour deposition (PECVD) on SiO₂ was developed at NTC facilities. The a-Si layers were deposited onto substrates consisting of 2 μ m SiO₂/Si, with a targeted a-Si thickness of 220nm and three different processes, whose parameters are summarized in Table 3.1. The ellipsometry measurements were performed to obtain the refractive index values in each case.



Figure 3.6: SEM images of fabricated a-Si:H waveguides. The waveguide thickness is ~220nm. The waveguide width is 450nm in sample NTC1-#1 and was changed to 500nm in NTC1-#4.

3.3. Low loss amorphous silicon

The starting point was a recipe that consisted on N₂ as plasma gas (NTC1 process) with a flow of 1500 standard cubic centimetre per minute (sccm). The precursor gas was silane (SiH₄) with a flow of 100 sccm. The evolution in the optimization of the process is summarized in Table 3.1. In the first samples high propagation losses were measured for TE polarization and no light was measured for TM polarization. High losses were attributed to sidewall roughness, as clearly shown in Figure 3.6, rather than absorption in the material. Optimization of the etching process gave rise to very low propagation losses for TE (<10dB/cm) despite extremely high losses for TM. The low refractive index value of ~2.24 was then clearly attributed to the high use of nitrogen and was also the explanation of high losses for TM polarization due to leakage of the mode to the substrate because of the lower confinement.

The process was adjusted and optimized to minimize the use of nitrogen (NTC2 process). The refractive index was increased to ~2.7 but it was still too low ($n_{a-Si}=3.47$ target). In this case, very low propagation losses were measured for TM due to the higher confinement of the mode in the waveguide.

However, we realized by literature that a-Si needs to be deposited in a plasma of hydrogen in order to passivate the dangling bonds, which are strongly absorbing in the infrared [80]. Then, a process based on hydrogen (NTC3 process) to increase the refractive index was developed. The quality of the hydrogenated a-Si (a-Si:H) that will be deposited onto the active BTO layers plays a fundamental role with respect to the waveguide and device performance. First of all, the refractive index of the layer can vary depending on the hydrogen content and deposition conditions. Furthermore, the losses in amorphous silicon are strongly dependent on the deposition conditions and can vary by several orders of magnitude. Therefore, to control the fabrication process is crucial towards achieving low-loss amorphous silicon. In this context, a refractive index of ~3.54 was firstly estimated which was very close to the target value. Experimental characterization of propagation losses gave also rise to relatively good results: around 18dB/cm for TE polarization and below 10dB/cm for TM polarization (Table 3.1). Despite larger propagation losses measured in NTC3 process rather than in NTC2 process, the difference between the refractive indexes of a-Si was more important in order to choose the suitability of NTC3 process.

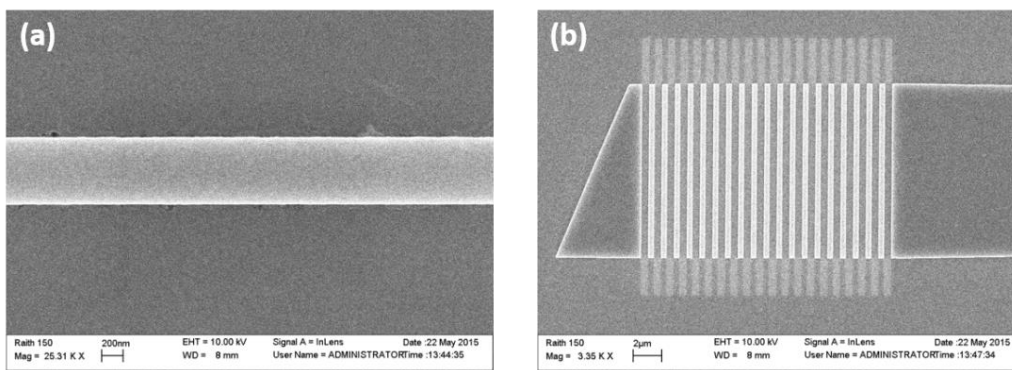


Figure 3.7: SEM images of the (b) waveguide and (c) grating coupler.

Chapter 3: Fabrication and characterization of electro-optic modulators based on BaTiO₃ in silicon

It must be pointed out that grating couplers were used in all cases as coupling light mechanism. Propagation losses were estimated by cut-back method through the use of waveguides with different lengths [81]. Figure 3.7 depicts scanning electron microscope (SEM) images of (a) waveguide and (b) grating coupler.

After the a-Si deposition on SiO₂ was successfully developed and optimized being the losses properly characterized, we proceed to optimize the a-Si deposition on BTO samples over a silicon substrate. It must be highlighted that such task was carried out with the aim of fully studying the influence of the different deposition parameters on the quality of the material. In this way, these runs were realized for testing the quality of the material and the feasibility of the deposition and no light waveguiding characterization was achieved since no optical confinement by index contrast is obtained on simply silicon substrate.

The successfully developed a-Si recipe optimized on SiO₂ used a temperature as high as 350°C. Such temperature increases the stress of the a-Si layer when deposited on BaTiO₃ and therefore, the a-Si layer peels off from the sample. We thus decreased the temperature down to 200°C (Recipe 1 in Table 3.2) but the refractive index was also decreased to 3.05.



Figure 3.8: Stress problem in sample processed with recipe 2.

	Temperature	RF power	SiH ₄ flow	H ₂ flow	Pressure	n	Comments
Recipe 1	200 °C	100W	80sccm	260sccm	4.6Torr	3.05	Low index
Recipe 2	225 °C	200W	62sccm	279sccm	3Torr	3.47	High stress
Recipe 3	200 °C	100W	50sccm	300sccm	3Torr	3.41	Good stress-n compromise

Table 3.2: PECVD processes amorphous silicon deposition parameters developed.

Therefore, the influence on the refractive index of the RF-power, pressure and H₂/SiH₄ ratio by using a low temperature around 200°C was analysed with the objective of obtaining a refractive index around 3.47. A new recipe with a low temperature of 225°C

3.3. Low loss amorphous silicon

was obtained with a refractive index of 3.47 (Recipe 2 in Table 3.2). Nevertheless, this recipe led to high stress in the a-Si layer and therefore the quality of the material was decreased.

The influence of the process parameters on the stress was then analysed by using Raman dispersion. Results showed, as expected, that the stress critically depends on the temperature, RF and H₂ flow. The reduction of stress is obtained at expenses of decreasing the refractive index so there is a trade-off between them. In this context, we were able to develop a new recipe (Recipe 3 in Table 3.2) with a refractive index of 3.41 and low stress of a-Si on BTO. Hence, a good adhesion of the BTO adhesion was achieved.

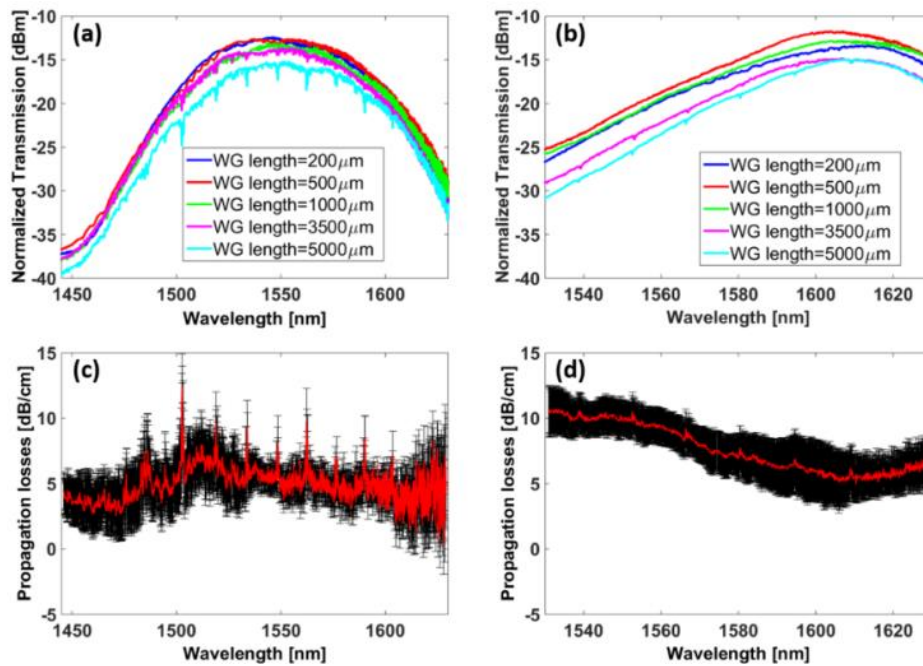


Figure 3.9: Normalized transmission spectra for (a) TE and (b) TM polarization of the a-Si/SiO₂ waveguides with different lengths fabricated with the final recipe. Propagation losses for (c) TE and (d) TM polarization.

Recipe 3 was then used for depositing a-Si layers on a SiO₂ substrate to test optical losses. In this way, a refractive index of 3.41, low stress, roughness below 0.2 nm and optical losses below 10 dB/cm for TE and TM were achieved with the final recipe. Figure 3.9 shows the normalized transmission spectra and the propagation losses for TE and TM polarization of the a-Si/SiO₂ waveguides with different lengths.

To summarize, the a-Si deposition process based on PECVD was successfully developed and optimized. The main goals were to achieve a refractive index value close to 3.47, optical losses below 10 dB/cm and reduced stress to avoid the delamination from the BTO layer. The final PECVD process developed at NTC facilities was based on H₂ as plasma gas and SiH₄ as precursor gas. The process parameters (temperature, RF power, pressure and H₂/SiH₄ ratio) were optimized to achieve the target goals. The stress of the a-Si layer was characterized using Raman dispersion and optical propagation losses were

characterized by fabricating and measuring the transmission spectrum of optical waveguides with different lengths. The roughness of the deposited a-Si layer was also analyzed and characterized by using AFM measurements. The main results of this study are the following:

- A low temperature, around 200°C, is required to reduce the stress of the a-Si layer when deposited on BTO.
- The reduction of stress is obtained at expenses of decreasing the refractive index existing a trade-off between them.

3.4. Fabrication of BTO based modulators

The process steps to fabricate optical devices in the a-Si/BTO/SOI stack, which is summarized in Table 3.3, was developed, optimized and successfully demonstrated. Firstly, the BTO layer was grown either by RF sputtering or MBE as explained in previous section. After the a-Si deposition, the sample was cleaned and consequently the resist film was coated on the a-Si layer. Afterwards, the sample was exposed by a direct writing electron beam lithography (EBL). The resist was developed prior to a reactive-ion etching inductively coupled plasma (RIE-ICP). Once the etching patterned the waveguides in the a-Si, a SiO₂ upper cladding was deposited by PECVD to protect the devices.

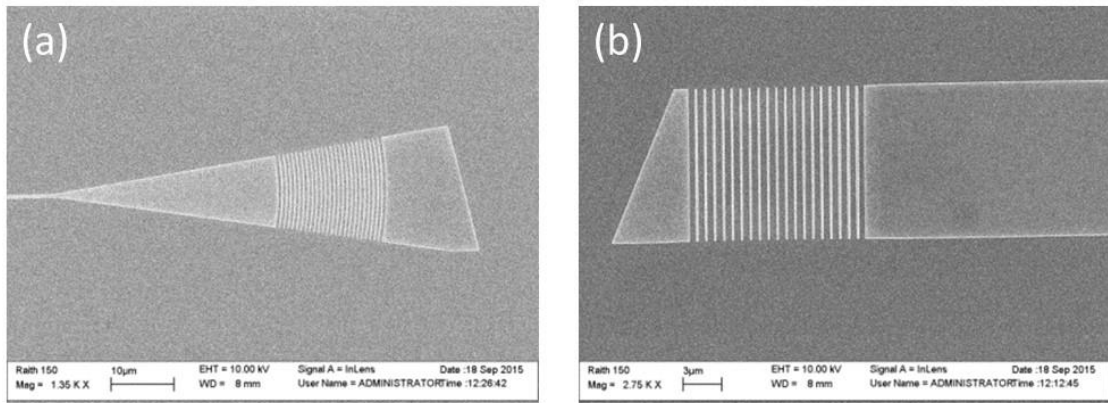


Figure 3.10: SEM images of (a) focused and (b) linear gratings.

Regular linear and focusing grating couplers were designed by means of 2D and 3D-FDTD simulations to minimize coupling losses. The design was carried out by considering that the grating is fully-etched in the amorphous silicon layer to ease fabrication. Better results were obtained for focusing grating, for which losses below 6dB for both TE and TM polarizations were achieved. Figure 3.10 shows a SEM image of the fabricated (a) focused and (b) linear gratings.

3.4. Fabrication of BTO based modulators

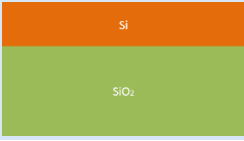
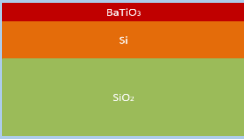
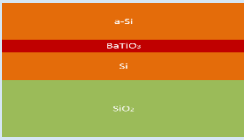
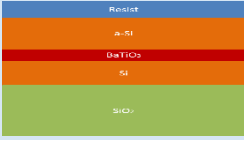
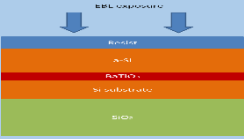

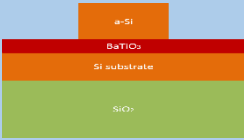
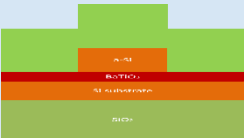
	Process	Technical Parameters
1.0	Commercial wafer 	Si over 2 μ m of SiO ₂
2.0	BTO deposition 	BTO deposition by either RF sputtering or MBE
3.0	a-Si deposition 	a-Si deposition by PECVD
4.0	Process: a-Si etching and SiO₂ deposition (cladding)	
4.1	Resist coating 	Spin-coating of HSQ resist. The resist film is coated on the a-Si layer.
4.2	EBL exposure 	Exposure in EBL system (VistecEBPG5000) The dose suggested here is used to fabricate waveguides in SOI technology.
4.3	HSQ resist Development 	The HSQ resist is developed.
4.4	RIE-ICP etching 	a-Si etching 1 minute a-Si etching process
4.5	PECVD SiO₂ deposition 	Upper cladding deposition SiO ₂ is deposited on the SOI sample by using PECVD.

Table 3.3: Description of the steps to fabricate optical devices in the a-Si/BTO/SOI stack.

3.5. Electrode fabrication process

Electrode contacts on BaTiO₃ were successfully fabricated and tested at NTC facilities.

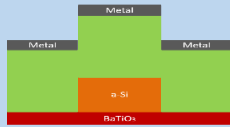
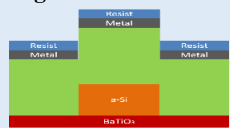
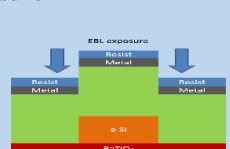
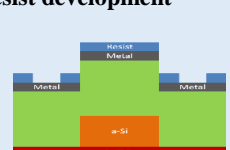
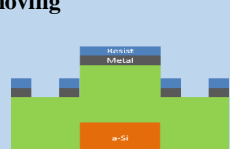
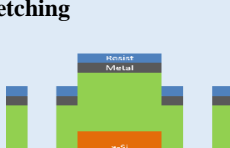


	Process	Technical Parameters
5.0	Process: silicon dioxide windows etching	
5.1	Chromium evaporation 	Evaporation of Cr Electron-beam evaporation.
5.2	Resist Coating 	Spin-coating of 950K PMMA A4 from MicroChem Corp. 100 nm thick resist layer
5.3	EBL exposure 	Exposure in EBL system (VistecEBPG5000) Metallic marks were used to align SiO ₂ windows with a-Si waveguides.
5.4	PMMA resist development 	<ul style="list-style-type: none"> • Development of the resist in MIBK:IPA (1:10) – 45 s • Rinsing in IPA – 45 s
5.5	Metal removing 	Metal is removed from not protected areas.
5.6	RIE-ICP etching 	Silicon dioxide etching 9 minutes SiO ₂ etching process
5.7-5.9	Cleaning, Resist Coating and EBL exposure	
5.10	Metal deposition 	Evaporation of Al, Ti, Cr/Au Electron-beam evaporation.
5.11	Lift-off 	Resist stripping

Table 3.4: Description of the electrode fabrication process.

3.5. Electrode fabrication process

Firstly, in order to place the electrodes on top of the BTO layer, there was need to open lateral windows in the cladding by developing a SiO₂ etching process up to the BTO layer. For this purpose, a chromium evaporation on the cladding prior to the 100nm thick resist PMMA coating was realized. Thereafter, the sample was exposed by a direct EBL and then the resist was developed. The metal was removed from this not exposed area and a RIE-ICP etching process was used to remove the silica cladding. After a metal removing, another 100nm thick resist PPMA coating was deposited. Hence, a new EBL exposure was carried out to define the electrodes in the resist. Finally, metal deposition of the electrodes was performed by evaporation and a lift-off process was realized. The fabrication process of electrodes is summarized in Table 3.4.

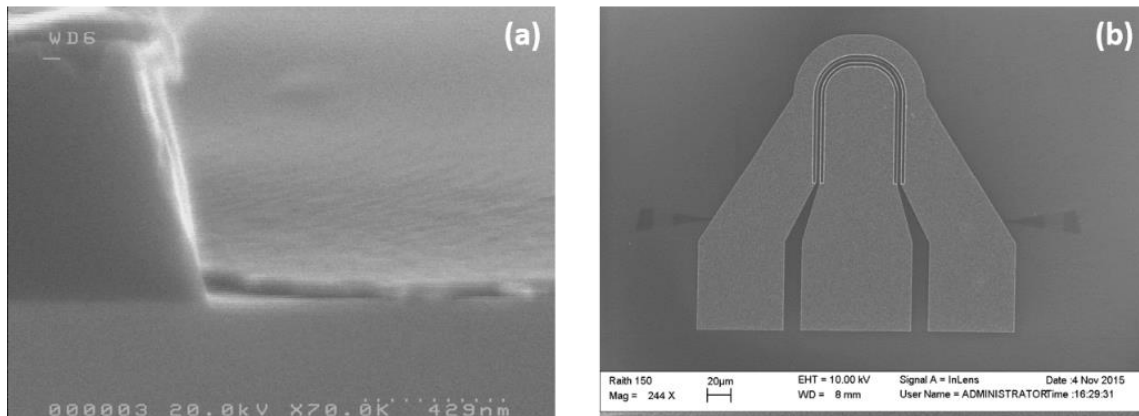


Figure 3.11: (a) Silica windows for fabricating the electrodes and (b) ring resonator with metal electrodes.

Figure 3.11 shows a SEM image of the silica window and a SEM image of a ring resonator with metal electrodes, respectively.

3.6. Optical characterization

Prior to demonstrating high speed EO modulators, we proceed to the passive characterization of the structures. The first step was to show that the light transmission could be achieved in the BTO based waveguides structures. Due to the late delivery of 100nm Si wafers (optimum Si layer obtained by simulation), it obligated us to make some runs with standard 220nm Si thickness substrates. Although very high losses were measured, these runs were used to successfully demonstrate the integration of BTO on Si. The structures used and the results obtained in all processed samples are shown along next subsections. The main difference between them is the deposition technique of the BTO layer. While INL partner deposited BTO by RF sputter, IBM provided us samples with BTO grown by MBE.

3.6.1. Fabricated devices

The general GDS (Graphic Database System) that we utilized consisted in sets of waveguides with different length to calculate propagation losses.

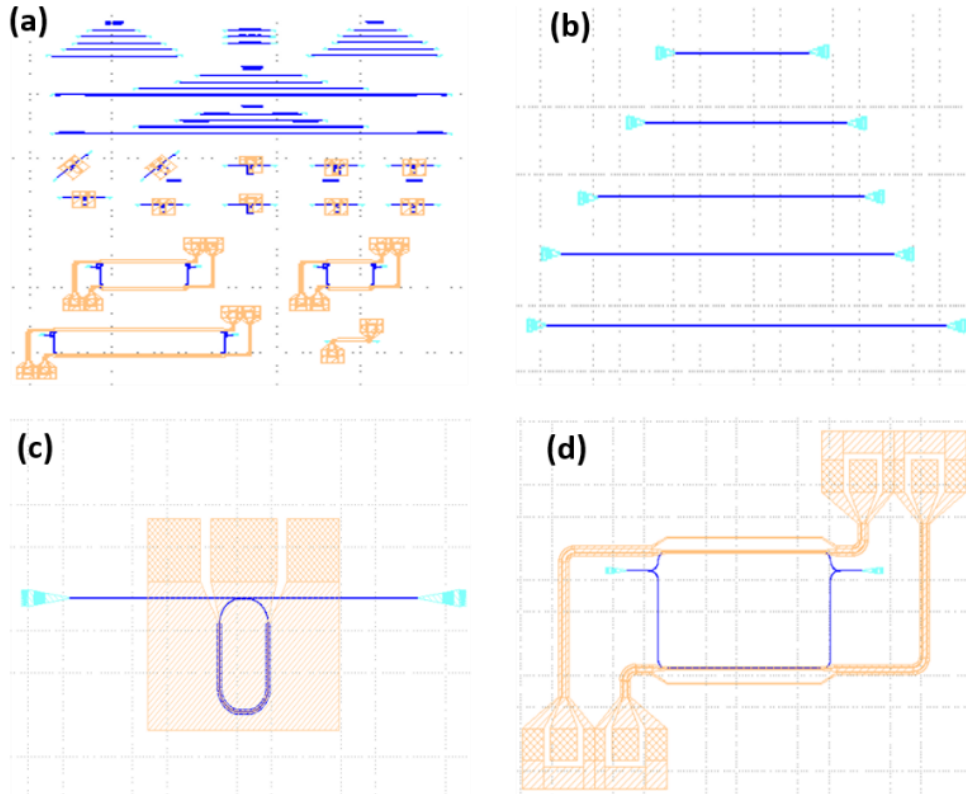


Figure 3.12: (a) Example of a GDS used for fabrication. Inset in the (b) set of waveguides with different lengths, (c) a ring resonator and (d) a MZI.

In Figure 3.12(a),(b) it can be seen an overview of a complete GDS and an example of the fabricated waveguides. Furthermore, we included structures that were introduced in chapter 1, such as ring resonators and MZI (Figure 3.12(c),(d)) with the aim of demonstrating EO modulation.

3.6.2. Experimental set-up

In passive characterization, an external cavity laser is employed. Directly after the laser, the input polarization state is set by adjusting an external polarization controller (PC), being the light injected into the chip with the selected polarization through vertical coupling with a single mode fiber. In order to monitor the received power, an optical power meter is used, which is also connected to a computer by a GPIB bus to measure the transmission spectra of the devices. Figure 3.13 shows the basic set-up with vertical coupling for passive characterization.

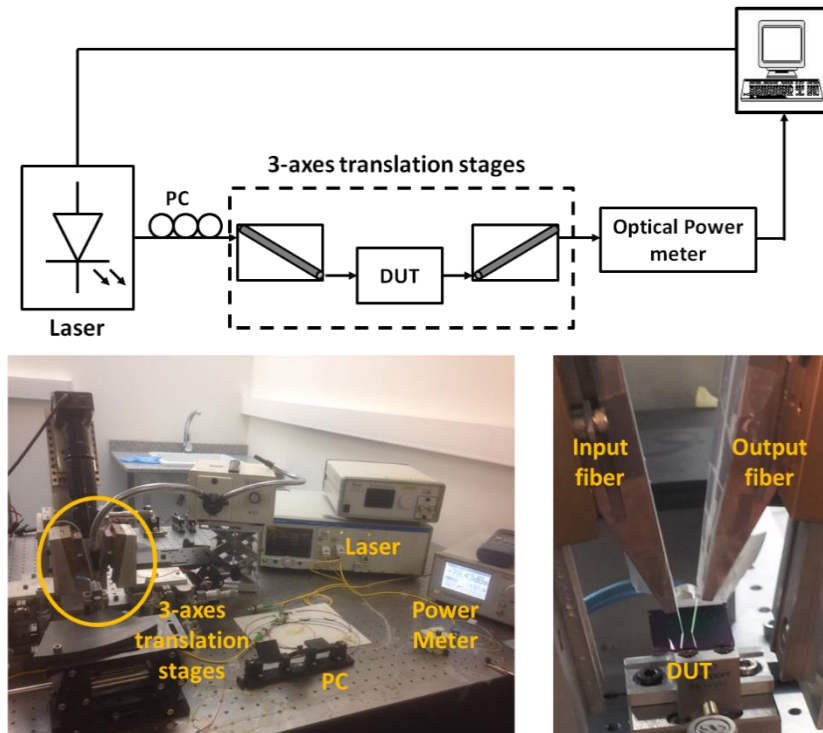


Figure 3.13: Schematic of the passive characterization set-up with vertical coupling.

3.6.3. Samples with RF sputtered BTO

Chronologically, we will start with INL RF sputtered BTO samples. In the first run, that we named #INL1 sample, the a-Si deposition was also performed at INL. In this first run, the thickness of the BTO layer was a bit thicker than expected (65nm) and 600nm width waveguides were patterned. Ring resonators were also added in the GDS (coupled to the shortest waveguide). The sample was covered with 750nm of SiO₂ in order to protect the devices. Propagation losses of 250-300dB/cm were obtained for both TE and TM polarization, as shown in Figure 3.14(a),(c). Gratings were adequately centred approximately at 1550nm wavelength, as expected from the design.

According to the design that was previously done, no such large losses were expected. The main differences between simulation work and experimental characterization was the low refractive index of the a-Si, which was $n=3.089$ instead of targeted value ($n=3.4758$) and the thickness (65nm instead of 50nm) of the BTO layer.

	n_{a-Si}	t_{a-Si}	n_{BTO}	t_{BTO}
#INL1	3.089	220nm	--	65nm

Table 3.5: Fabrication parameters of sample #INL1.

For TE polarization, it is expected that the lower refractive index of the a-Si pushes down the optical mode into the structure, thus decreasing the effective refractive index

value of the optical mode and slightly increasing optical losses. Furthermore, in the SEM image of the waveguide, which is depicted in Figure 3.15, it can be seen the high granularity that appeared on the a-Si seems to stand out as the major responsible of large losses.

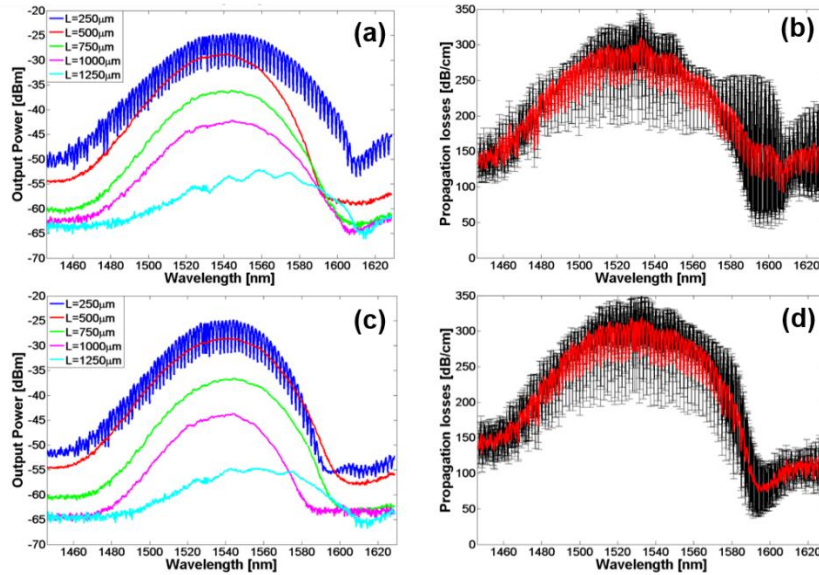


Figure 3.14: Results of optical measurements of #INL1. Transmission spectra of waveguides with different lengths and propagation losses for (a), (b), TE polarization and (d), (e), TM polarization, respectively. Blue spectra correspond to ring resonator.

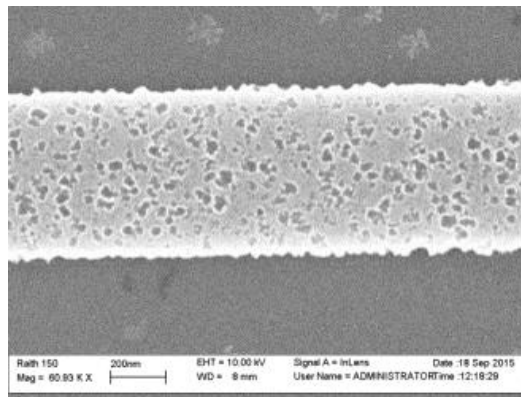


Figure 3.15: SEM image of the deposited a-Si waveguide.

The experimental results obtained in ring resonators for both polarization are shown in Figure 3.16. From these spectra, it can be extracted the experimental Free Spectral Range (FSR), the Full Width Half Maximum (FWHM) and the quality factor (Q), which are FSR~2nm, FWHM~0.5nm and Q~2680 for TE and FSR~1.96nm, FWHM~0.6nm and Q~2340 for TM polarization.

In order to analyse the accuracy of the results above presented, the simulation of the structure with the fabricated parameters and values was carried out. The group index n_g was determined by:

3.6. Optical characterization

$$n_g = n_{\text{eff}} - \lambda \frac{dn_{\text{eff}}}{d\lambda} \quad (3.1)$$

where n_{eff} is the effective index and λ is the wavelength. The simulated group index was 3.291 for TE polarization and 3.402 for TM polarization.

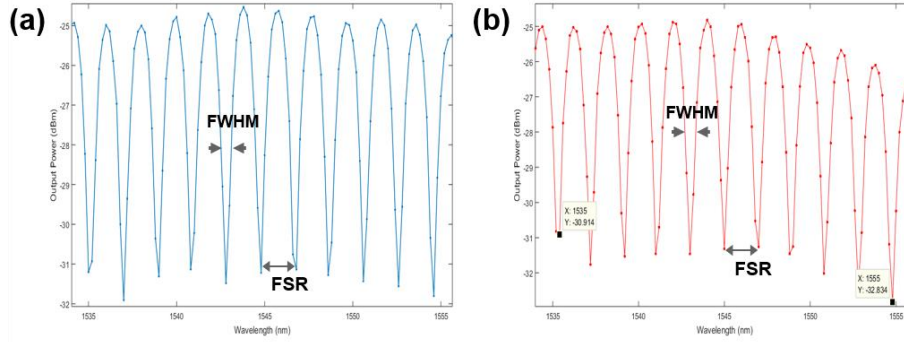


Figure 3.16: Experimental transmission spectrum of the ring resonator for (a) TE and (b) TM polarization with the FSR and FWHM depicted.

The theoretical FSR from Eq. (1.5) can be calculated and compared with the experimental one. Furthermore, from the experimental Q factor extracted from the transmission spectra, we can obtain a value of the loss per unit length α by using Eq. (1.3). In order to obtain the experimental propagation losses from the transmission spectrum we will use:

$$loss(dB/cm) = 10 \log_{10}(e^{\alpha L}) \sim 4.34 \alpha (cm^{-1}) \quad (3.2)$$

Hence, for TE polarization the theoretical results are $FSR=2.04$ and $\alpha=49.8cm^{-1}$ that corresponds to approximately 216dB/cm. Additionally, for TM polarization the estimated values are $FSR=1.97$, $\alpha=59.1cm^{-1}$ and 256dB/cm. Therefore, it can be seen that the experimental results are in agreement with the theory. From this sample, two ring resonators, one TE and one TM, were selected to undergo metallization process and be EO characterized.

In the second run (#INL2), the measured BTO layer was thinner than expected (42nm) with a refractive index of 2.208. The a-Si deposition was also performed at INL. In this case, an extra set of waveguides with $W=700nm$ was introduced in the GDS to compare propagation losses with respect to $W=600nm$ waveguides and the stitching effect. The sample was then covered with 750nm of SiO_2 .

	n_{a-Si}	t_{a-Si}	n_{BTO}	t_{BTO}
#INL2	3.00	240nm	2.208	42nm

Table 3.6: Fabrication parameters of sample #INL2.

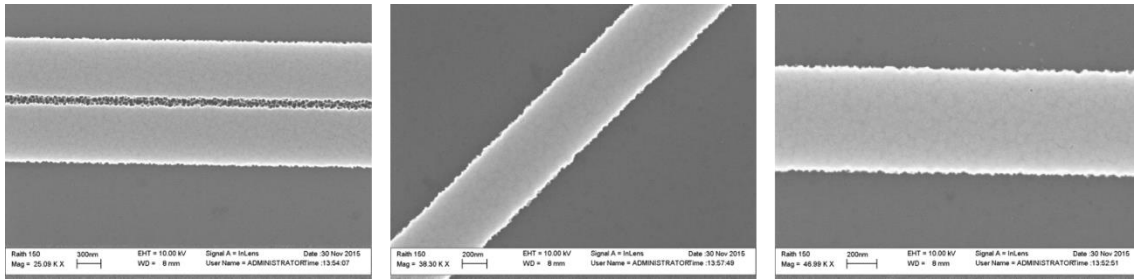


Figure 3.17: SEM images of the fabricated a-Si waveguides.

Despite the roughness was not as low as desired, the quality of the fabricated waveguides increased and no bubbles were detected, as seen in Figure 3.17.

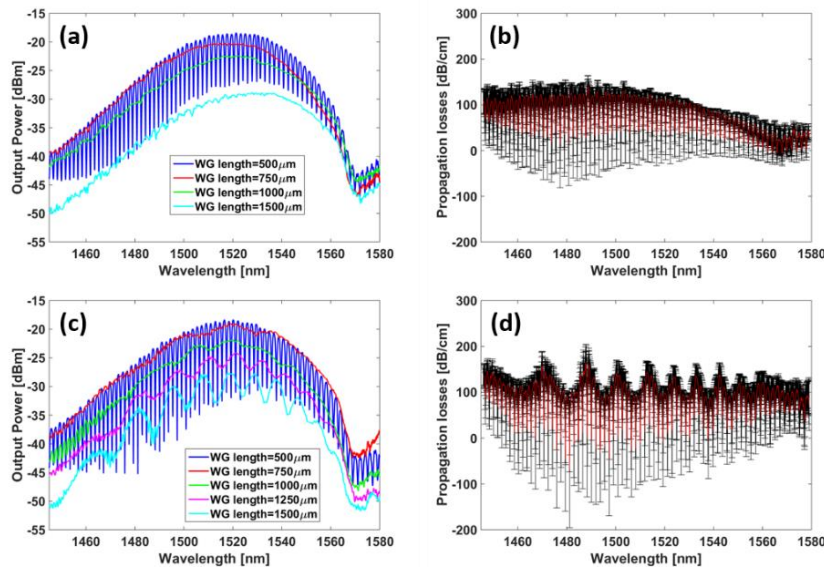


Figure 3.18: Results of optical measurements of #INL2 for TE polarization. Transmission spectra of waveguides with different lengths and propagation for (a), (b) waveguides with $W=600\text{nm}$ and (c), (d) waveguides with $W=700\text{nm}$, respectively. Blue spectra correspond to ring resonator.

Comparing to the results from #INL1, it was possible to reduce significantly the propagation losses until approximately 100dB/cm for TE polarization, as seen in Figure 3.18(b) and (d).

Due to the still low refractive index of a-Si (around 3), it would be expected that the optical mode was pushed down into the BTO and Si layers. Nevertheless, the thickness of the a-Si was 240nm instead of the 220nm designed. Increasing the thickness pushes up the optical mode. Therefore, we believe that both fabrication deviations counteracted each other avoiding the increment in the optical losses.

From the ring resonators spectra it can be extracted the experimental Q factor which is related to the ring resonator losses. The obtained value for TE polarization, $Q\sim 4340$, gave us α value of 31.3cm^{-1} by using Eq (3.2). In this way, the estimated losses were approximately 136dB/cm , a bit larger than losses by cut-back method, probably due to bend losses of the ring resonators.

3.6. Optical characterization

Regarding to TM polarization, Figure 3.19 shows the transmission spectra obtained for 600nm and 700nm waveguides widths. The lack of correlation between losses and longer distances and the strong reflections observed in all waveguides was not a good sign of the accuracy of measured propagation and insertion losses. Besides, grating couplers were centred on 1430nm, far from the original design and TM ring resonators did not show resonances.

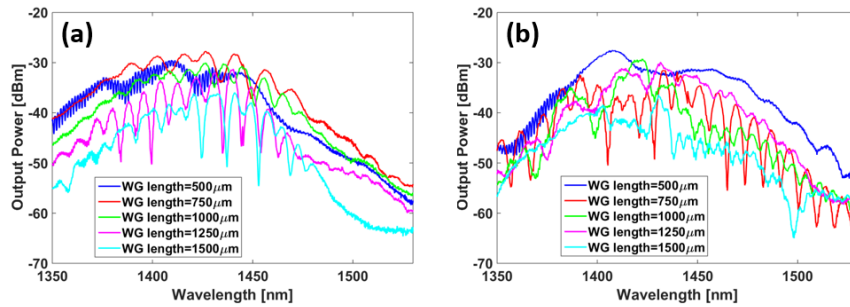


Figure 3.19: Results of optical measurements of #INL2 for TM polarization. Transmission spectra of waveguides with different lengths for (a) waveguides with $W=600\text{nm}$ and (b) waveguides with $W=700\text{nm}$. Blue spectra correspond to ring resonator.

Regarding to TM polarization, Figure 3.19 shows the transmission spectra obtained for 600nm and 700nm waveguides widths. The lack of correlation between losses and longer distances and the strong reflections observed in all waveguides was not a good sign of the accuracy of measured propagation and insertion losses. Besides, grating couplers were centred on 1430nm, far from the original design and TM ring resonators did not show resonances.

In general terms, no significant differences were observed between both $W=600\text{nm}$ and $W=700\text{nm}$ waveguides despite light reflections in the latter. Therefore, $W=600\text{nm}$ waveguides were chosen for the following samples.

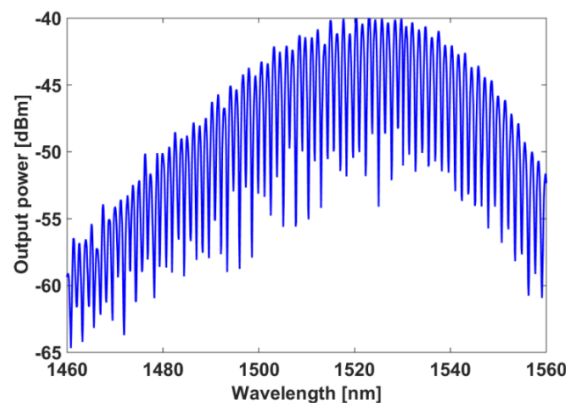


Figure 3.20: Results of optical measurements of #INL2. Transmission spectrum of the MZI for TE polarization.

A MZI structure was firstly introduced in the GDS of this sample for each polarization. In Figure 3.20 it can be seen the transmission spectrum of the 2mm long MZI for TE polarization, where large losses were measured. In the case of the MZI for TM

Chapter 3: Fabrication and characterization of electro-optic modulators based on BaTiO₃ in silicon

polarization, it was not possible to measure the transmission spectrum due to extremely large losses. Therefore, TE ring resonators and MZI were selected to deposit electrodes and be EO characterized.

	n_{a-Si}	t_{a-Si}	n_{BTO}	t_{BTO}
#INL3	3.41	220nm	2.208	35nm

Table 3.7: Fabrication parameters of sample #INL3.

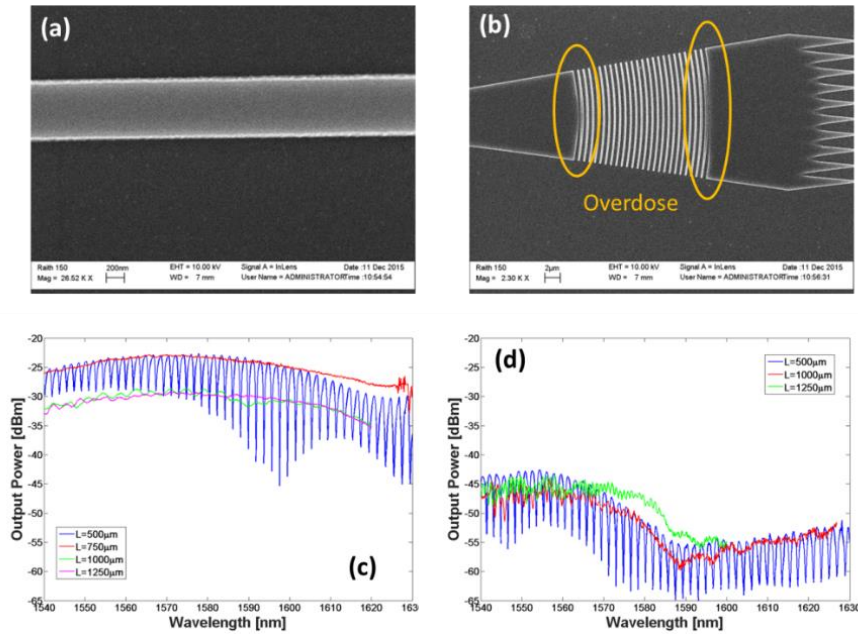


Figure 3.21: (a) SEM image of waveguide with a-Si deposited, (b) SEM image of one of the fabricated gratings showing the problem of over-exposition that happened during fabrication, transmission spectra of waveguides with different lengths for (c) TE polarization and for (d) TM polarization. Blue spectra correspond to ring resonator.

The following run (#INL3) was fabricated with slightly thinner BTO thickness than expected (35nm) with a refractive index of 2.208. The deposition of a-Si was successfully realized at NTC facilities with a refractive index of 3.41, close to the objective, and considerably lower roughness and granularity than in previous samples was obtained, as it can be seen in Figure 3.21(a).

Unfortunately, gratings were not perfectly fabricated due to an over-exposition effect (see Figure 3.21(b)). Therefore, the estimation of propagation losses by cut-back method was not accurate because coupling losses were not the same in all gratings. However, we can obtain losses inherent to the ring resonator by measuring the quality factor. The experimental values were $Q \sim 7980$ for TE and $Q \sim 3970$ for TM, which corresponded to α value of 16.2cm^{-1} and 34cm^{-1} respectively. In this way, the estimated losses were approximately 70dB/cm for TE and 147dB/cm for TM.

3.6. Optical characterization

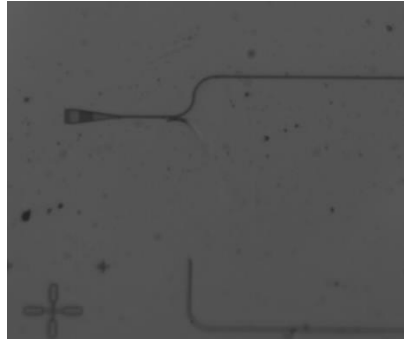


Figure 3.22: MZI with cuts in the waveguide.

Regarding to modulating structures, it was not possible to measure light in any MZI because of some cuts in the waveguides (Figure 3.22). However, as it is depicted in Figure 3.21(c),(d), ring resonators (coupled to the shortest waveguide) for both TE and TM polarization showed a good extinction ratio (ER) and were metallized to be EO characterized.

The a-Si deposition at NTC facilities in #INL4 followed the same recipe developed in previous sample, thus obtaining an a-Si refractive index of 3.41, a BTO refractive index of 2.216 and roughness below 1nm. The thickness of the sputtered BTO layer was 35nm, again lower than expected. As in previous samples, ring resonators and MZI were included, all of them with a waveguide width of 600nm. Finally, the sample was covered by 750nm of SiO₂ cladding.

	n_{a-Si}	t_{a-Si}	n_{BTO}	t_{BTO}
#INL4	3.41	220nm	2.216	35nm

Table 3.8: Fabrication parameters of sample #INL4.

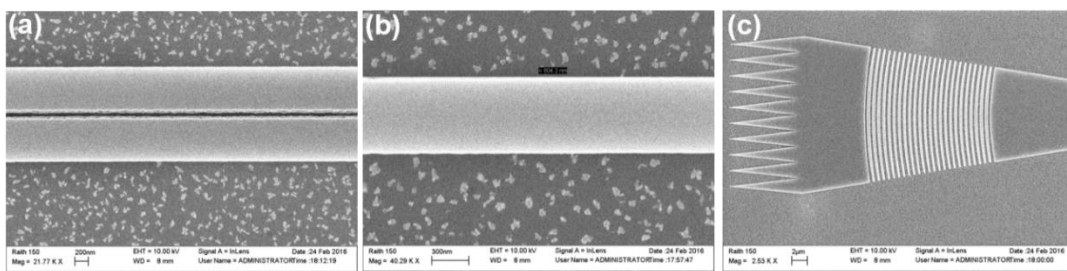


Figure 3.23: (a) SEM image of ring resonator, (b) waveguide with a-Si deposited and (c) focused grating coupler.

SEM images of the fabricated waveguides and gratings are shown in Figure 3.23. It can be appreciated some granularity on the BTO surface, which according to the good obtained results, it did not seem to affect optical losses.

The transmission spectra and propagation losses are depicted in Figure 3.24, both for TE and TM polarization. Propagation losses for TE around 20dB/cm were measured, significantly decreasing the values obtained in previous samples. However, due to the fact

that some waveguides were damaged and high losses were measured, only few spectra were used to calculate losses. Hence, the accuracy of these results was not the optimum.

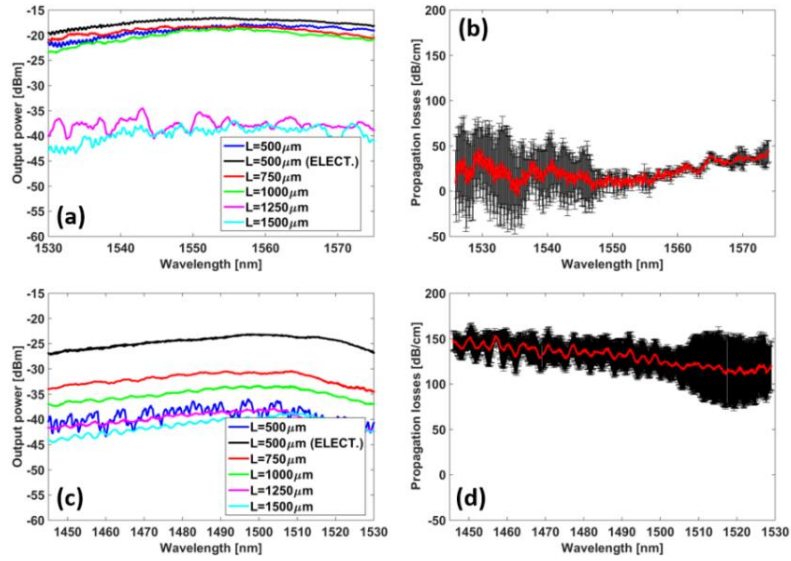


Figure 3.24: Results of optical measurements of #INL4. Transmission spectra of waveguides with different lengths and propagation losses for (a), (b) TE polarization and (c), (d) TM polarization, respectively.

Regarding to TM polarization, a better performance was measured compared to previous samples, although still large losses, around 130dB/cm, were extracted (Figure 3.24(d)). As in previous samples, we obtained losses inherent to the ring resonator by measuring the quality factor. The experimental values were $Q \sim 9250$ for TE and $Q \sim 3390$ for TM, which corresponded to α value of 14.8cm^{-1} and 40.5cm^{-1} respectively. In this way, the estimated losses were approximately 64dB/cm for TE and 175dB/cm for TM.

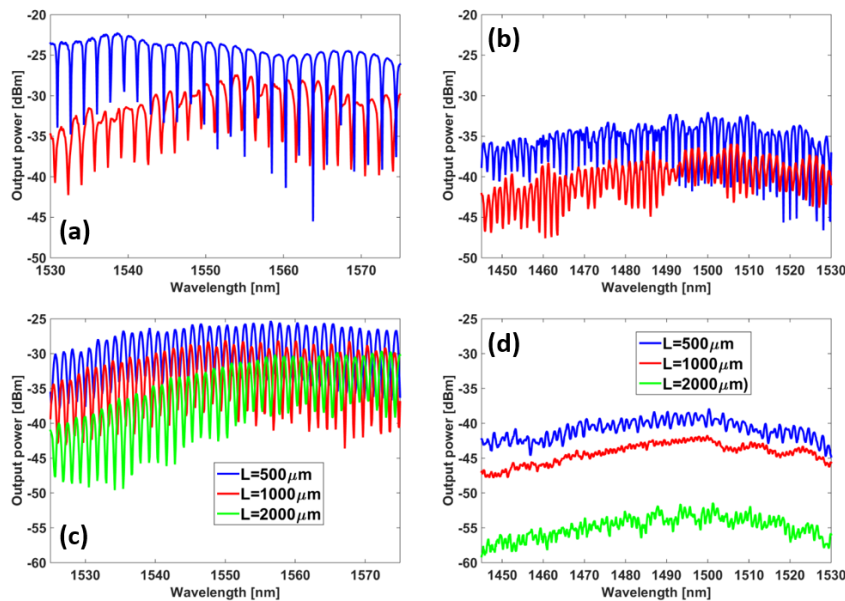


Figure 3.25: Results of optical measurements of #INL4. Transmission spectra of ring resonators for (a) TE and (b) TM polarization. Transmission spectra for MZI with different lengths for (c) TE and (d) TM polarization, respectively.

3.6. Optical characterization

The transmission spectra of ring resonators that presented lowest losses for both TE and TM polarization are shown in Figure 3.25(a),(b). The main difference between them was the larger losses and the lower extinction ratio (ER) of the resonances for TM polarization rings. The only difference between ring resonators was the distance between the waveguide and the ring, which values were chosen to obtain larger ER.

With respect to MZI, one more time we extracted better results for TE polarization (Figure 3.25(a)) rather than TM polarization (Figure 3.25(b)). The TE MZI spectra showed a good behaviour with clear resonances and an ER of approximately 10dB. TM MZI response presented significant larger losses and no resonances were observed. All TE modulating structures and TM ring resonators were metallized.

The last sample with BTO fabricated at INL and a-Si deposited and successfully characterized at NTC was #INL5. It was the first time in which the fabricated BTO thickness (51nm) was close to the designed one. The roughness was also low (around 1nm) and the $n_{a-Si}=3.41$. The measured refractive index of the BTO was 2.213. It was introduced in the GDS some extra blocks of waveguides with different widths (700nm, 1000nm and 1500nm), in order to compare propagation losses. This time, the sample was covered by a cladding of 500nm of SiO₂.

	n_{a-Si}	t_{a-Si}	n_{BTO}	t_{BTO}
#INL5	3.41	220nm	2.213	51nm

Table 3.9: Fabrication parameters of sample #INL5.

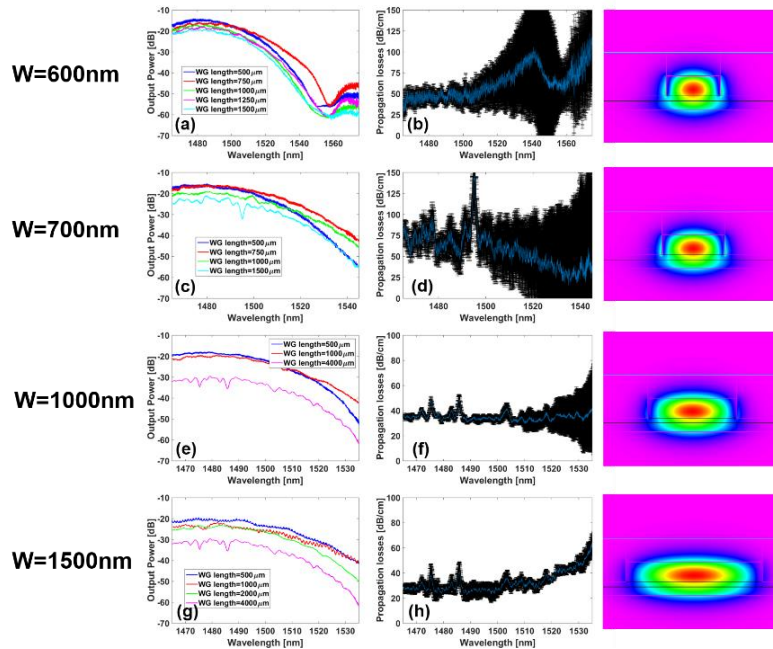


Figure 3.26: Results of optical measurements of #INL5 for TE polarization. Transmission spectra of waveguides with different lengths and propagation losses for (a), (b) waveguides with W=600nm (c), (d) W=700nm, (e), (f) W=1000nm and (g), (h) W=1500nm, respectively. The TE modes corresponding to each waveguide width are shown in the right side.

Propagation losses of 40dB/cm were obtained for $W=600\text{nm}$ and TE polarization, as seen in Figure 3.26. It is expected that wider waveguides support multi-mode propagation and therefore, if superior order modes are excited, that would increase propagation losses.

However, for TE polarization we obtained lower propagation losses for wider waveguides widths. This is mainly due to the TE mode nature. As it can be seen in Figure 3.26, in the 600nm waveguide width the TE mode is strongly confined in the a-Si waveguide. When increasing the waveguide width, TE mode becomes less confined and thus losses due to roughness of the waveguide fade.

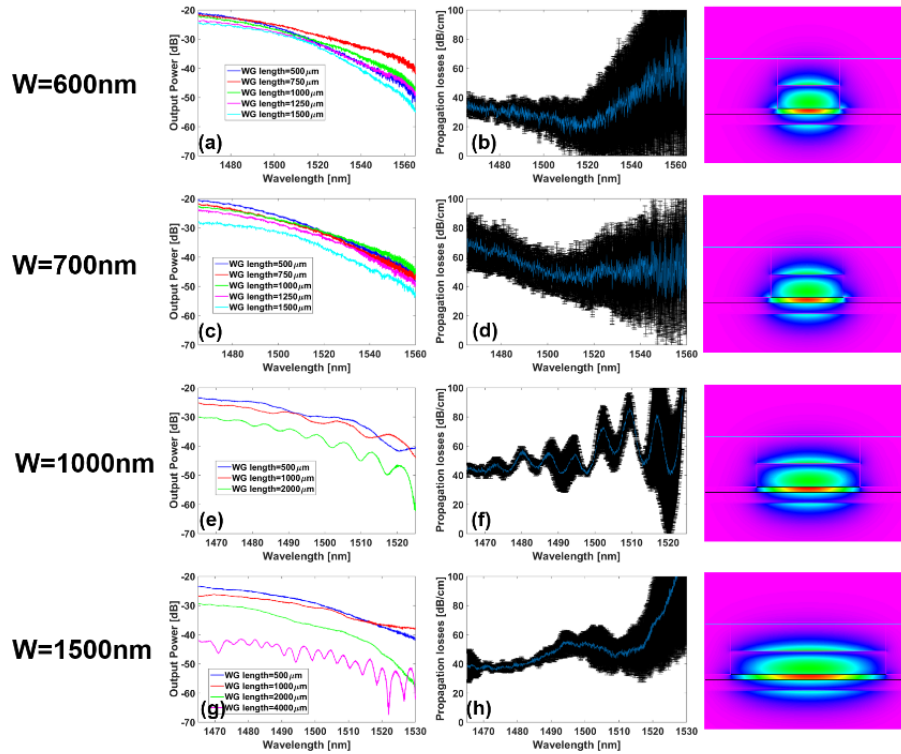


Figure 3.27: Results of optical measurements of #INL5 for TM polarization. Transmission spectra of waveguides with different lengths and propagation losses for (a), (b) waveguides with $W=600\text{nm}$ (c), (d) $W=700\text{nm}$, (e), (f) $W=1000\text{nm}$ and (g), (h) $W=1500\text{nm}$, respectively. The TM modes corresponding to each waveguide width are shown in the right side.

For TM polarization (Figure 3.27), propagation losses of 30dB/cm were measured for 600nm width waveguides. In this case, wider waveguides did not show better performance in terms of propagation losses. Indeed, this can be also explained because of the nature of the TM mode. The confinement of the TM mode is mainly in the BTO layer. Hence, increasing the waveguide width slightly affects propagation losses for TM polarization. The summary of the results of all waveguides for TE and TM polarization is shown in Table 3.10 and Table 3.11.

3.6. Optical characterization

	Width [nm]	Propagation losses
TE	600	40dB/cm @ 1480nm
	700	50dB/cm @ 1480nm
	1000	35dB/cm @ 1480nm
	1500	25dB/cm @ 1480nm
TM	600	35dB/cm @ 1470nm
	700	60dB/cm @ 1470nm
	1000	45dB/cm @ 1470nm
	1500	40dB/cm @ 1470nm

Table 3.10: Propagation losses obtained for all sets of waveguides with different width for TE and TM polarization.

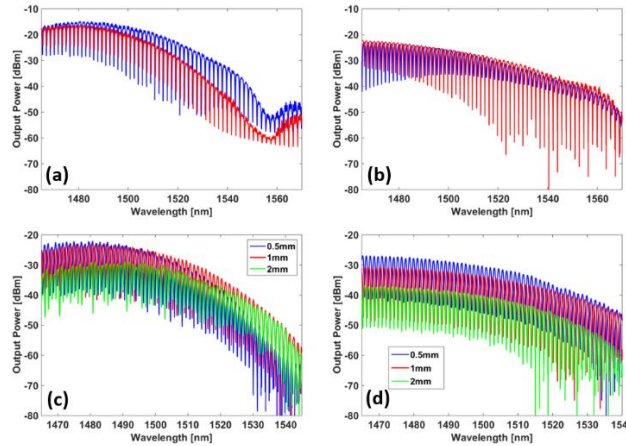


Figure 3.28: Results of optical measurements of #INL5. Transmission spectra of ring resonators for (a) TE and (b) TM polarization. Transmission spectra for MZI with different lengths for (c) TE and (d) TM polarization, respectively.

With respect to modulator devices, we obtained clear resonances in ring resonators (Figure 3.28(a),(b)) and MZI (Figure 3.28(c),(d)) for both TE and TM polarization with larger ER than in previous samples. Losses inherent to the ring resonator by measuring the quality factor were also analysed. The experimental values were $Q \sim 10950$ for TE and $Q \sim 4690$ for TM, which correspond to α value of 12.8cm^{-1} and 31.4cm^{-1} respectively. In this way, the estimated losses were approximately 55dB/cm for TE and 135dB/cm for TM. Higher losses for TM might be attributed to bend losses due to the TM mode high confinement in the BTO region rather than in the a-Si waveguide. As a result of the clear resonances and good ER that showed all modulating devices, we proceed to metallize them in order to analyse their EO behaviour

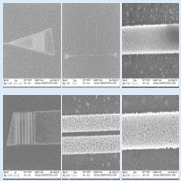
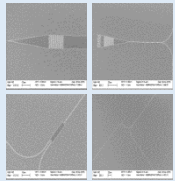
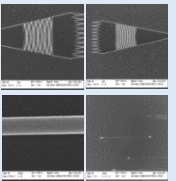
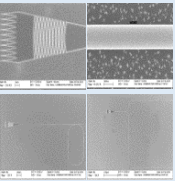
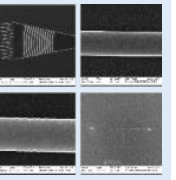
	#INL1	#INL2	#INL3	#INL4	#INL5
$t_{a-Si}/t_{BTO}/t_{Si}$	220nm a-Si 65nm BTO 4nm STO 100nm Si on SOI	240nm a-Si 42nm BTO 3nm STO 100nm Si on SOI	220nm a-Si 35nm BTO 3nm STO 100nm Si on SOI	220nm a-Si 35nm BTO 3nm STO 100nm Si on SOI	220nm a-Si 51nm BTO 3nm STO 100nm Si on SOI
n_{BTO}	--	2.208	2.208	2.216	2.213
n_{a-Si}	3.089	3	3.41	3.41	3.41
SEM Images					
Optical results (Propagation losses)	$\alpha_{TE} \approx \alpha_{TM} \approx 250-300 \text{ dB/cm}$	$\alpha_{TE} \approx 100 \text{ dB/cm}$	Propagation losses not well estimated. Over-exposition problem in grating couplers.	$\alpha_{TE} \approx 20 \text{ dB/cm}$ $\alpha_{TM} \approx 130 \text{ dB/cm}$	$\alpha_{TE} \approx 40 \text{ dB/cm}$ $\alpha_{TM} \approx 30 \text{ dB/cm}$
Metallized structures	TE and TM RR.	TE RR and MZI.	TE and TM RR	TE and TM RR TE MZI	TE and TM RR and MZI

Table 3.11: Summary of the fabrication parameters, SEM images and optical results of BTO sputtered samples (RR=ring resonator).

In Table 3.11 it can be seen the summary of all samples processed by RF sputtered BTO, besides the obtained optical results and structures that were metallized. Through the different fabricated samples, we have been able to decrease losses until 20-30dB/cm probably linked to a reduction in the a-Si roughness and due to the better quality of the deposited BTO layer.

3.6.4. Sample with MBE BTO

The only sample optically characterized provided by IBM consisted in MBE grown BTO. The measured BTO thickness was 63nm and the refractive index 2.31.

	n_{a-Si}	t_{a-Si}	n_{BTO}	t_{BTO}
#IBM1	3.41	220nm	2.31	63nm

Table 3.12: Fabrication parameters of sample #IBM1.

3.6. Optical characterization

The a-Si deposition was successfully accomplished at NTC, obtaining $n_{a-Si}=3.41$ and roughness around 0.2nm. This sample was covered with 500nm of SiO₂.

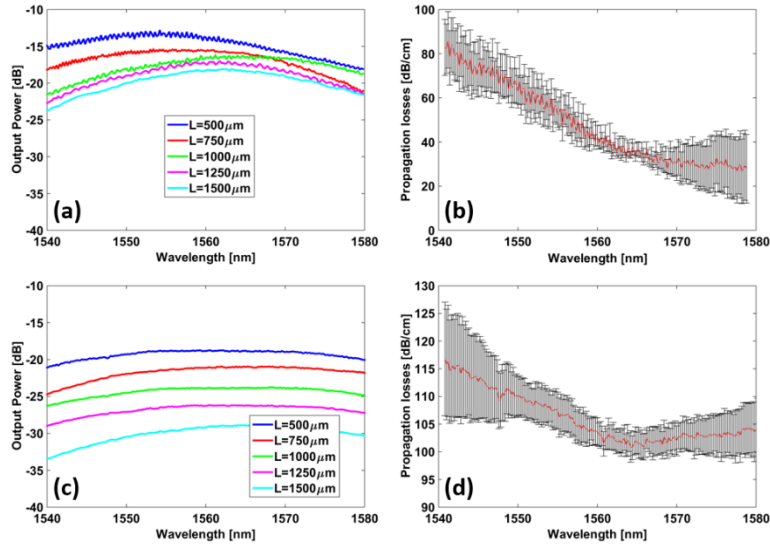


Figure 3.29: Results of optical measurements of #IBM1. Transmission spectra of waveguides with different lengths and propagation losses for (a), (b) TE polarization and (c), (d) TM polarization, respectively.

Propagation losses around 40-60dB/cm were obtained for TE polarization, as shown in Figure 3.29(b). In the case of TM polarization, the measured propagation losses were larger (Figure 3.29(d)), between 100-110dB/cm. With respect to losses connected to the ring resonators, we extracted experimental values of $Q \sim 4650$ for TE and $Q \sim 3070$ for TM, which corresponded to α values of 28.8cm^{-1} and 44.5cm^{-1} respectively. In this way, the estimated losses were approximately 124dB/cm for TE and 193dB/cm for TM. Due to the lack of more samples, we were not able to determine whether the origin of these losses were related to the BTO itself or connected to fabrication process steps.

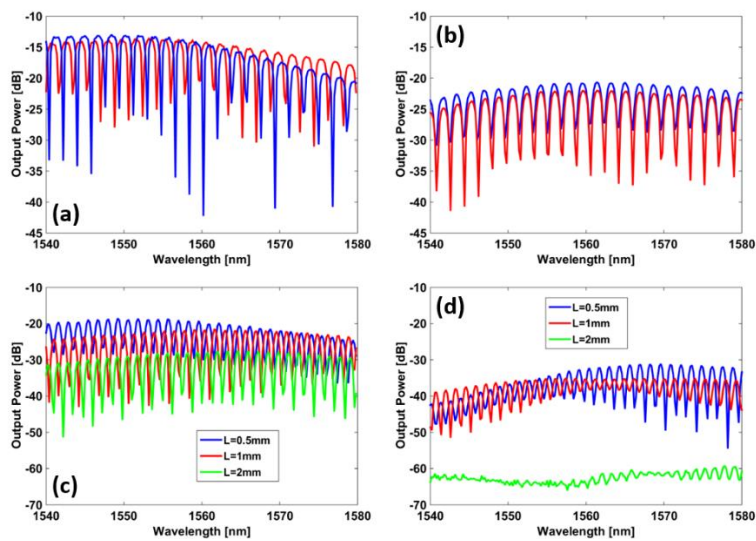


Figure 3.30: Results of optical measurements of #IBM1. Transmission spectra of ring resonators for (a) TE and (b) TM polarization. Transmission spectra for MZI with different lengths for (c) TE and (d) TM polarization, respectively.

In this sample, ring resonators and MZI of both TE and TM polarization, which showed clear resonances with high ER, were metallized in order to characterize their EO behaviour. After optical results, in next section we will explain the EO characterization that was carried out in the modulating structures.

3.7. Electro-optical characterization

Once the passive measurements were successfully carried out, we opened lateral windows in the ring resonators and MZIs that showed resonances and placed the electrodes to proceed to the EO characterization. In this section, EO measurements with DC probes were firstly performed. Among other EO effect that can take place, due to the Pockels effect present in BaTiO₃, when an electric field is applied through the electrodes the refractive index changes and therefore the resonance shifts. After characterizing the modulating structures in DC regime, we applied RF signals through RF probes to the electrodes in order to achieve EO modulation.

3.7.1. DC regime

3.7.1.1. Experimental set-up

Light is coupled from a laser to the chip via a lensed fiber after polarization control, as it has been previously explained for passive characterization. In this set-up, a DC signal is applied to the electrodes of the ring resonators and MZIs through DC probes. The transmission spectra for different voltages are measured in this kind of set-up. A schematic and pictures of the real set-up are shown in Figure 3.31.

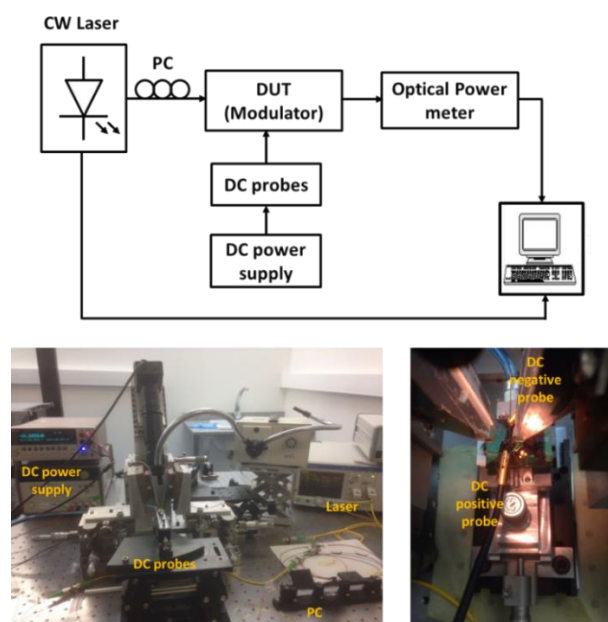


Figure 3.31: Experimental set-up for realizing DC measurements.

3.7.1.2. DC electro-optic results

RF sputtered BTO samples

As explained in subsection 3.5, a process for the electrode fabrication by opening lateral windows and metallization was developed at NTC facilities. Following such process, ring resonators in #INL1 were metallized (Figure 3.32) and EO characterized.

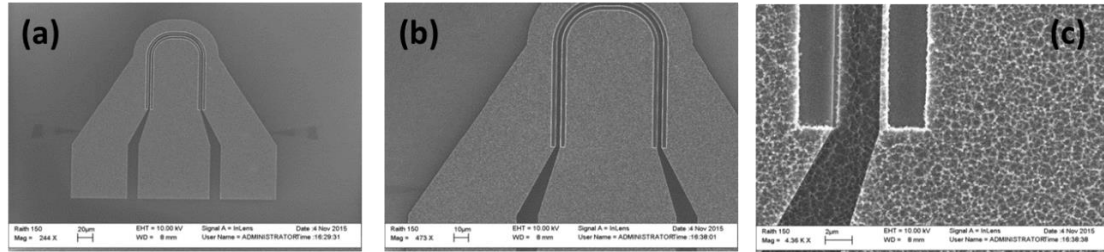


Figure 3.32: SEM images of lumped electrodes on one of the fabricated racetracks in #INL5.

Because of the ferroelectric nature of BaTiO_3 , this material is formed by regions that have spontaneous polarization, known as domains. As aforementioned in chapter 1, when an electric field is applied, those domains which are oriented in the same direction of the electric field will remain aligned and those which are aligned in another direction, will experience a tendency to change their orientation towards the direction in which the electric field is applied. When the applied electric field is high enough to align all domains, the coercive field is reached and thus all domains are aligned. Hence, by applying some consecutive sweeps both positive and negative voltage values, we expect to align domains in both directions and be able to observe the characteristic butterfly behaviour of ferroelectric materials. In this way, we proceed to measure ring resonators in DC regime.

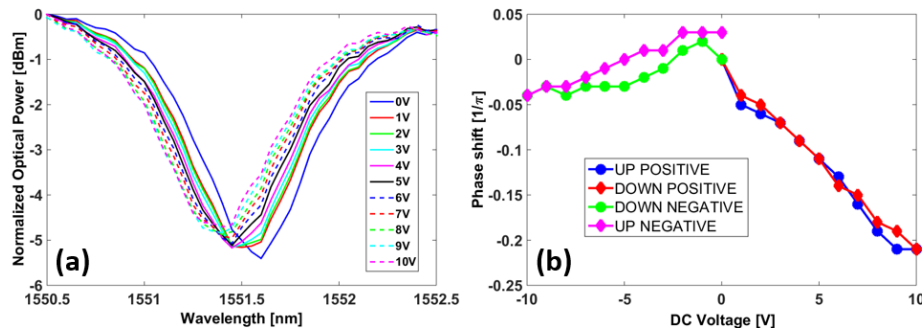


Figure 3.33: (a) Resonance shift for different DC voltages and (b) phase shift as a function of applied DC voltage.

In Figure 3.33(a) it can be observed the sweep of the resonance between 0 and 10V. By sweeping positive and negative voltages, we obtained that both upward and backward paths of voltages (i.e. the response when the voltage increases and when decreases respectively) have the same direction (Figure 3.33(b)), where a linear wavelength shift is clearly observed. From the wavelength shift of the resonance due to the applied voltage

we can evaluate the modulation efficiency of the ring resonator by calculating the $V_{\pi} \cdot L$ product by following equations:

$$\Delta\lambda = \lambda(V_{DC} = 0V) - \lambda(V_{DC} = 5V) = 121 \text{ pm} \quad (3.3)$$

$$FSR = \frac{\lambda^2}{n_g L_{ring}} \rightarrow n_g = \frac{\lambda^2}{FSR \cdot L_{ring}} = 3.36 \quad (3.4)$$

$$\Delta n_{eff} = \frac{\Delta\lambda}{\lambda} n_g \frac{L_{ring}}{L_{active}} = 3.7 \cdot 10^{-4} \quad (3.5)$$

$$\Delta\Phi = \frac{2\pi}{\lambda} L_{active} \Delta n_{eff} = 0.12\pi \quad (3.6)$$

$$L_{\pi} = \frac{\lambda}{2\Delta n_{eff}} = 2.1 \text{ mm} = 0.21 \text{ cm} \quad (3.7)$$

$$V_{\pi} \cdot L = V \cdot L_{\pi} = 5V \cdot 0.21 \text{ cm} = 1.05V \cdot \text{cm} \quad (3.8)$$

where λ is the wavelength, $\Delta\lambda$ is the wavelength variation, FSR is the free spectral range, n_g is the group index, L_{ring} is the length of the ring resonator, L_{active} is the active length of the ring resonator, Δn_{eff} is the variation of the effective refractive index, $\Delta\Phi$ is the phase shift, V is the applied voltage, V_{π} is the half-way voltage and L_{π} is the required length for a phase shift of π .

From such DC measurements, and with the formulas above mentioned, we obtained a modulator efficiency $V_{\pi}L$ of 1.05Vcm. Despite no butterfly behaviour was detected, the linear dependence of the phase shift against the applied voltage is characteristic of the Pockels effect for a-axis grown BTO. Furthermore, the resonance shifted to the same direction for both positive and negative voltages, which might be related with ferroelectric domain switching. However, the non-perfect butterfly shape indicates the presence of other physical effects besides Pockels effect, which could be the redistribution of charges at the BaTiO₃/Si interface or charging of bandtail states in the a-Si:H layer [54,84]. In any case, the clear indication of Pockels effect would be the demonstration of high speed modulation, which is sought in next subsection.

In sample #INL2 both ring resonators and MZI structures were metallized and measured in the DC regime to analyse the EO switching performance. However, no ring resonator showed any EO behaviour. The sweep of the resonance between 0V and 20V for the TE ring resonator is depicted in Figure 3.34.

As it can be seen, no resonance shift was observed even when applying 20V through the electrodes of the ring resonator. Nevertheless, when a voltage was applied to a MZI we did experience a clear change. Figure 3.35(a) shows the phase shift as a function of the applied DC voltage for the MZI structure.

3.7. Electro-optical characterization

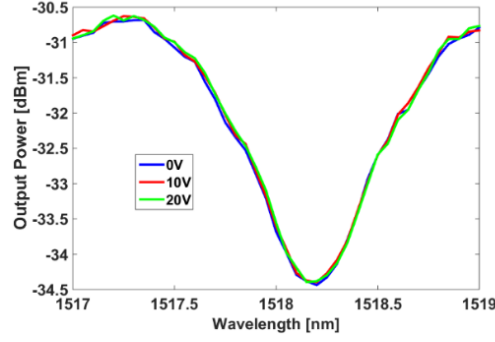


Figure 3.34: Resonance of the TE ring resonator for different DC voltages

The reason of this EO behaviour difference between ring resonators and MZI within the same sample could be connected to a poor crystallinity of the BTO fabricated material since the longest length of the MZI may include some small crystalline areas whereas the short length of the ring resonator may not. The reduced number of devices in this sample did not allow us to extract broader conclusions.

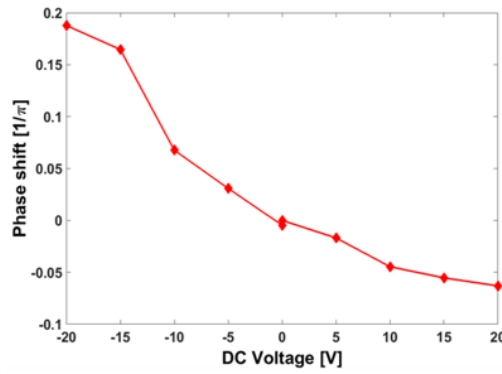


Figure 3.35: Phase shift as a function of the DC voltage of the MZI structure.

In order to evaluate the modulation efficiency of the MZI, the $V_{\pi} \cdot L$ product of the MZI can be calculated as follows:

$$\Delta\lambda = \lambda(V_{DC} = -20V) - \lambda(V_{DC} = 0V) = 133 \text{ pm} \quad (3.9)$$

$$FSR = \frac{\lambda^2}{n_g \Delta L} \rightarrow n_g = \frac{\lambda^2}{FSR \cdot \Delta L} = 3.43 \quad (3.10)$$

$$\Delta n_{eff} = \frac{\Delta\lambda}{\lambda} n_g \frac{\Delta L}{L} = 7.36 \cdot 10^{-5} \quad (3.11)$$

$$\Delta\Phi = \frac{2\pi}{\lambda} L_{active} \Delta n_{eff} = 0.19\pi \quad (3.12)$$

$$L_{\pi} = \frac{\lambda}{2\Delta n_{eff}} = 1.05 \text{ cm} \quad (3.13)$$

$$V_{\pi} \cdot L = V \cdot L_{\pi} = 20V \cdot 1.05cm = 21V \cdot cm \quad (3.14)$$

where L is the length of the MZI and ΔL is the length difference between the arms of the MZI.

With respect to the ring resonator from the #INL1, for the 2mm-long MZI modulator, a much lower modulation efficiency of 21V·cm was calculated. By comparing both results it can be highlighted several issues:

- No hysteresis was observed in any device.
- The phase shift variation had different slopes depending on the voltage sign in both devices.
- The sign of the phase shift variation, and therefore of the effective index, for both structures is opposite when negative voltages are applied.

Therefore, it can be stated that although we were able to see an EO response, the obtained results were not in agreement with the expected performance for modulation exclusively based on Pockels effect. Indeed, the behaviour experienced of device in sample #INL2 can be explained due to the metallization process.

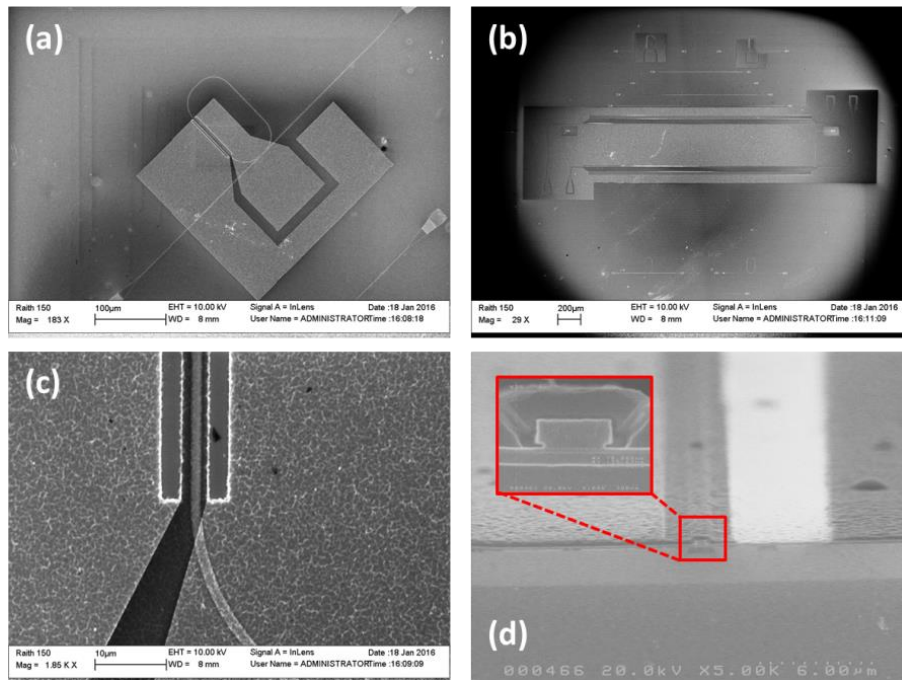


Figure 3.36: SEM images of devices in sample #INL2. (a) Ring resonator modulator with lumped electrodes, (b) MZI modulator with travelling wave electrodes, (c) detail of opened windows in metallization process and (d) transversal profile of one arm of the MZI and inset of a detail of the a-Si/BTO/Si waveguide.

SEM images of some fabricated structures with electrodes are shown in Figure 3.36. As can be seen in Figure 3.36(d), one window was not opened in the MZI and the metallization was carried out onto the silica cladding. Indubitably, it affected to the EO

3.7. Electro-optical characterization

performance thus decreasing significantly the EO overlap in the BTO region and therefore the modulation efficiency.

In sample #INL3 ring resonators were metallized and were measured in DC regime to obtain the modulator phase shift by means of the wavelength shift as a function of the DC voltage.

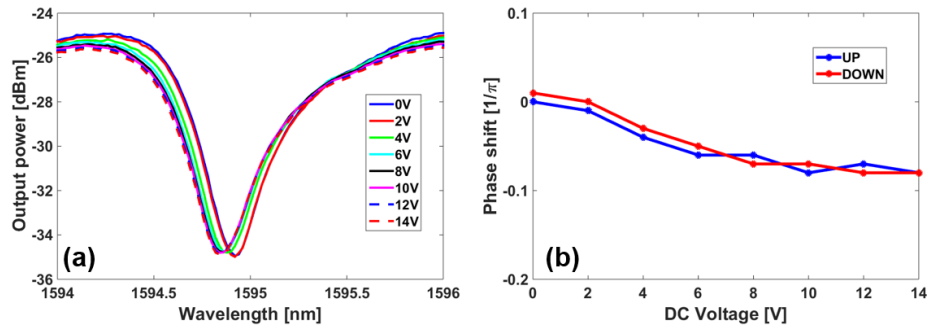


Figure 3.37: (a) Resonance shift for different DC voltages and (b) phase shift as a function of applied DC voltage.

Figure 3.37(a) the wavelength shift of the resonance when applying a voltage is shown for a ring resonator. Although both upward and backward paths of voltage were similar (Figure 3.37(b)), the short shift of the resonance gave rise to a $V_{\pi} \cdot L$ product of around $4.2V \cdot cm$ for the TE ring resonator by using Eq. (3.3)-(3.8). We believed that the low modulation efficiency is probably caused by not optimum quality of the BTO layer.

In order to reduce the fabrication steps that could be damaging the BTO layer and therefore the EO performance, in sample #INL4 it was avoided the etching step in the silica cladding and electrodes were placed above 500nm of SiO_2 . In this sample, many MZI and ring resonators were tested and even when applying 20V, the resonance roughly move. The reason why EO measurements lacked of resonance shifting might be the large voltage drop across the SiO_2 layer in combination with a strongly coercive field not accessible in the experiments [78]. Therefore, it was decided to keep opening lateral windows in next samples and deposit the electrodes directly on the BTO layer to increase the EO overlap.

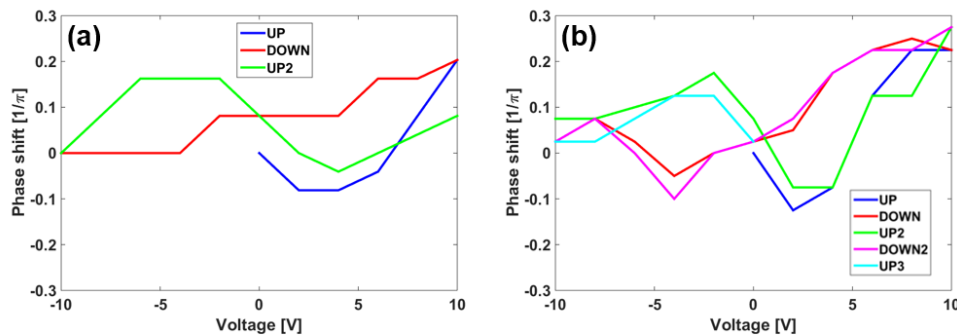


Figure 3.38: Phase shift as a function of the DC applied voltage for (a) 1mm and (b) 2mm long TE polarized MZI.

By that means we proceed in sample #INL5. In this sample, we observed clear wavelength shifts when sweeping the applied voltage between -10V and 10V to MZI of both TE and TM polarization. In Figure 3.38 it is depicted the phase shift as a function of the applied voltage for two TE MZI of different length.

Despite large variability between devices, MZI showed the called “butterfly” hysteresis, characteristic of ferroelectric materials. As previously discussed, the EO response of two antiparallel domains is cancelled. However, antiparallel domains can be switched by flipping their ferroelectric polarization. This happens when the applied electric field overcomes the coercive field. Therefore, this loop is the expected behaviour for ferroelectric switching. Furthermore, we demonstrate that multiple loops lie approximately on top of each other (Figure 3.38b)), thus making the switching reproducible. Undoubtedly, this is a clear signature of ferroelectric behaviour of BTO.

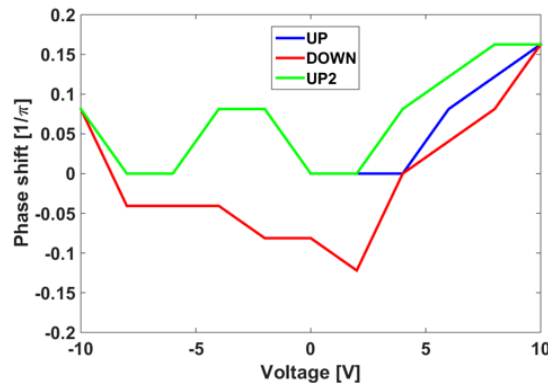


Figure 3.39: Phase shift as a function of the DC applied voltage for 2mm long TM polarized MZI.

In the case of TM polarized MZI, although switching was appreciated, it was not possible to measure any hysteresis behaviour (Figure 3.39). From the Eq. (3.9)-(3.14) the modulation efficiency can be calculated by estimating the $V_{\pi} \cdot L$ product of the MZIs. The obtained results were:

- For the TE 1mm long MZI: $V_{\pi} \cdot L = 3.6 \text{V} \cdot \text{cm}$
- For the TE 2mm long MZI: $V_{\pi} \cdot L = 5.7 \text{V} \cdot \text{cm}$
- For the TM 2mm long MZI: $V_{\pi} \cdot L = 12.5 \text{V} \cdot \text{cm}$

Comparing to the best analyzed cases in simulation, a considerably lower modulation efficiency was obtained in experimental characterization. The reason might be linked to a mixture of a-axis and c-axis domains and the 0° oriented waveguide towards the BTO layer. However, in this sample, the modulation efficiency obtained for the MZIs was considerably improved comparing to previous samples. The reason behind this behaviour might be connected to the longer distance between electrodes previously utilized in the first 3 samples (3.6μm versus 2.5μm).

3.7. Electro-optical characterization

MBE BTO Sample

Static EO measurements were carried out in sample #IBM1. SEM images of a fabricated MZI with electrodes is shown in Figure 3.40.

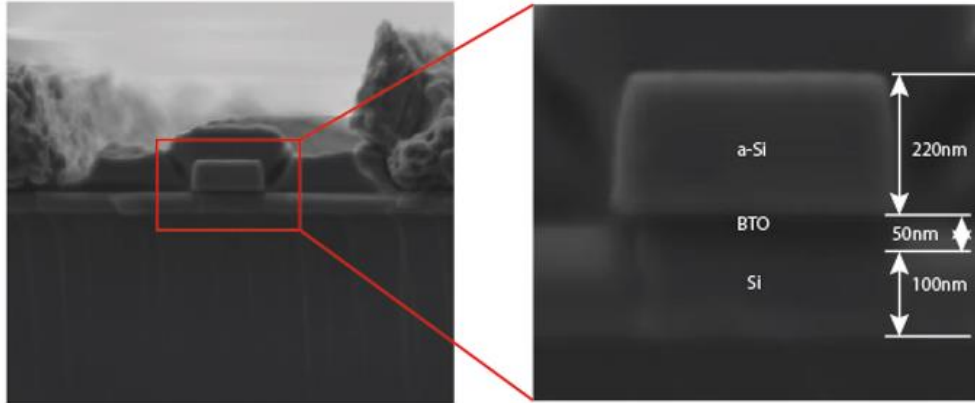


Figure 3.40: SEM images of the fabricated waveguide with electrodes.

A clear resonance shift is observed in all MZI and ring resonators. Figure 3.41(a) shows the resonance shift when applying a DC voltage to the 1mm long TE MZI electrodes. In previous samples, current values around μA were measured. However, current values up to few mA were measured in this sample (Figure 3.41(b)) and consequently it cannot be assumed that Pockels effect is the only responsible of the resonance movement at DC regime.

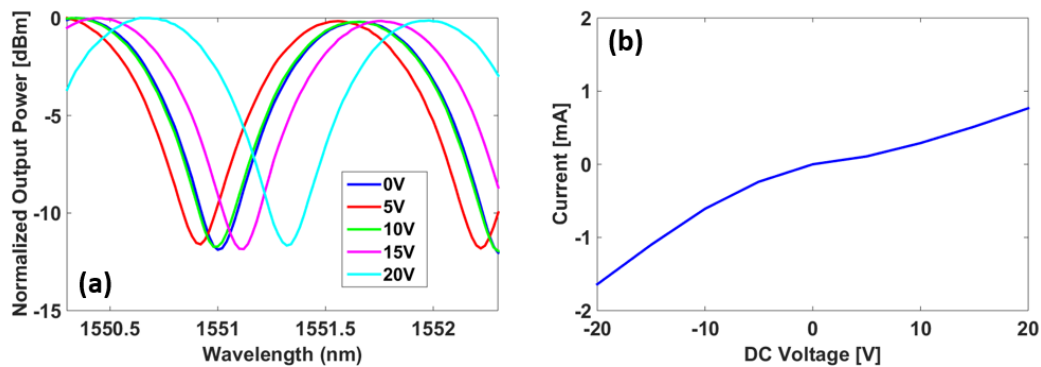


Figure 3.41: (a) Wavelength shift of the MZM response for different DC bias voltages and (b) current measured as a function of the applied voltage.

In fact, the thermo-optic effect is clearly dominating in the DC regime when high voltages are applied, hiding any possible ferroelectric behaviour. As it can be seen in Figure 3.42, longer MZI produce longer resonance shifts for the same DC voltage, being the relation between phase shift applied voltage quadratic for longer MZI.

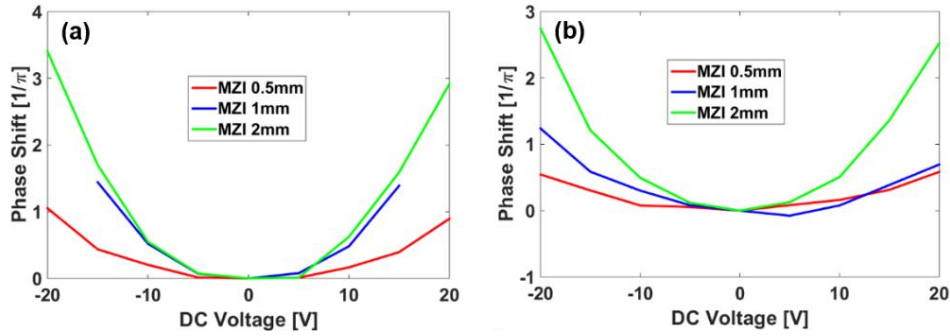


Figure 3.42: Phase shift as a function of the DC applied voltage of MZM with different lengths for (a) TE and (b) TM polarization.

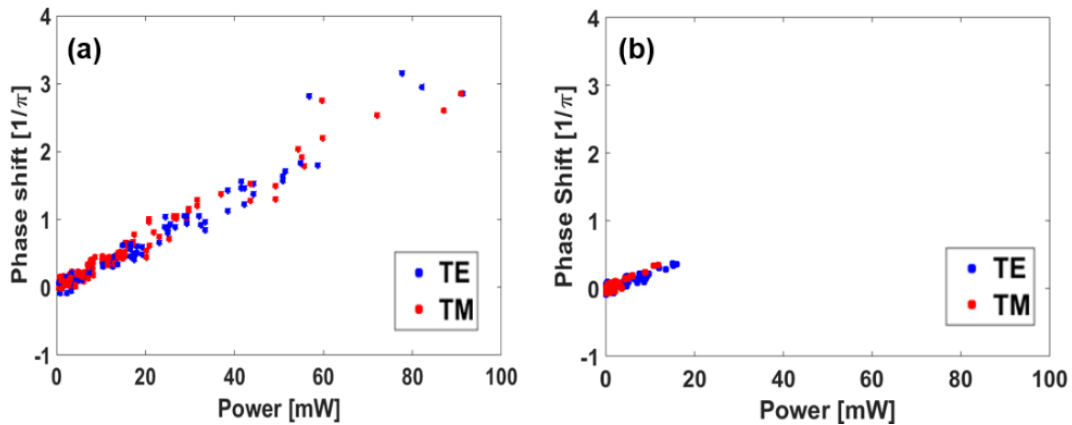


Figure 3.43: Phase shift as a function of the applied power for all (a) MZM and (b) ring resonators.

In such cases, as expected from the dominating thermo-optic effect, the refractive index change is always positive for both positive and negative applied voltages. Moreover, the phase shift variation of all MZI and ring resonators show a clear linearly dependence on the electrical DC power (Figure 3.43), evidencing one more time the thermo-optic effect dominion in DC regime.

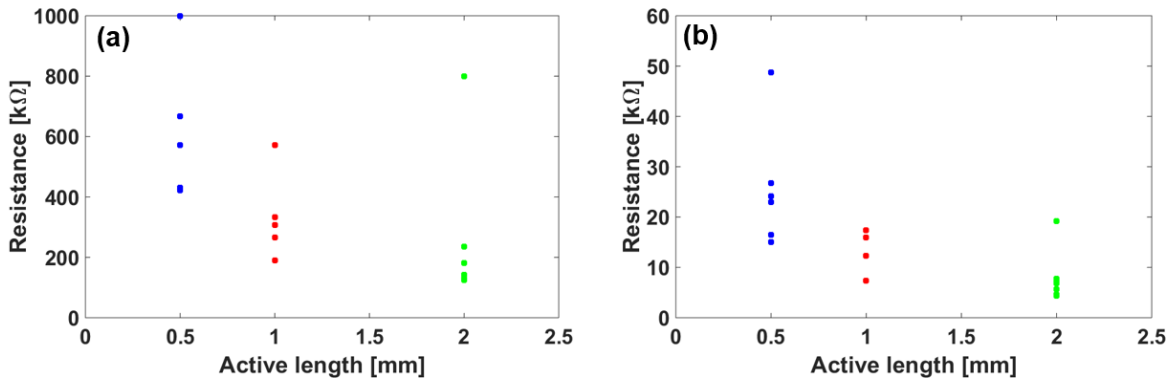


Figure 3.44: Resistance of the MZI when applying (a) 5V and (b) 20V for different lengths.

The resistance of different devices were also analysed. It is interesting to notice that devices show different resistance depending on the applied voltage and the active length. In Figure 3.44 it is depicted the resistance values for all MZI when 5V and 20V are

3.7. Electro-optical characterization

applied, respectively. In fact, the resistance values can vary even one order of magnitude. In addition, lower resistance is obtained also in devices with longer active length.

The high current values measured produced a variation in losses that might be connected to carrier effects. Although this variation was not evidenced in all devices, if electrical power was reduced for high voltages, the effect of the carriers was more clearly revealed. Indeed, at low voltages, negative phase shifts were appreciated in some cases, being stronger for TM polarization. In general terms, the influence of carriers was more important for TM rather than TE polarization (Figure 3.45).

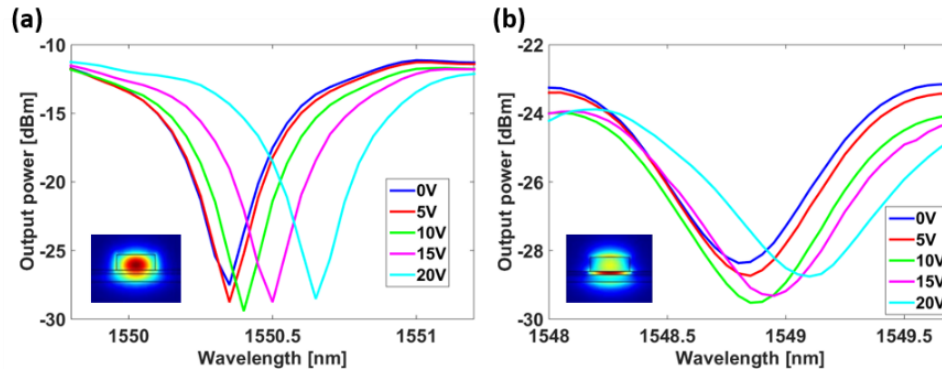


Figure 3.45: Wavelength shift of a ring resonator response for different DC bias voltages for (a) TE and (b) TM polarization. Insights of the respective TE and TM mode.

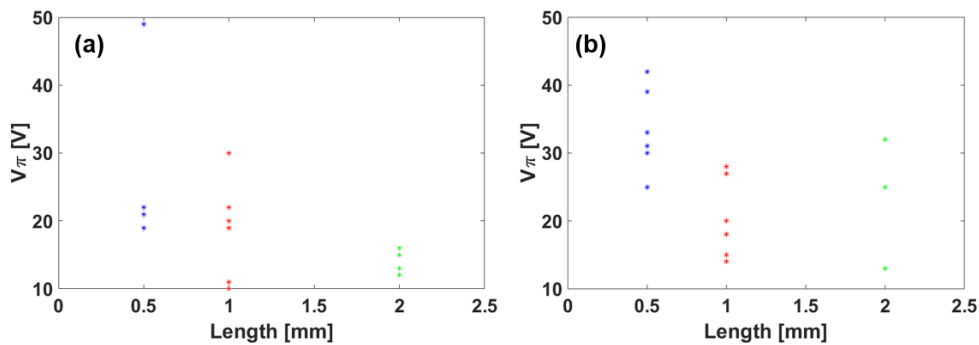


Figure 3.46: V_π values for all MZI as a function of the length for (a) TE and (b) TM polarization.

The V_π results were also analysed. Figure 3.46 depicts the obtained V_π results of all MZI for both TE and TM polarization. The V_π are characterized by obtaining a clear dependence with the active length of the modulators and being the V_π lower for TE than TM.

The main conclusions that we obtained are below listed:

- The resistance decreases (power increases) for longer active lengths
- The phase shift mainly depends on the power consumption
- Same power \rightarrow smaller effective index variation with longer active lengths
- Same index variation \rightarrow higher phase shift variation for TE polarization

Due to the domination of the thermo-optic effect in DC regime, the contribution of Pockels effect remains hidden. According to the formulation, and assuming that both effects act independently, for c-axis grown BTO, both Pockels and thermo-optic effect produce a positive phase shift change for TE polarization. However, for TM polarization, Pockels effect produces a negative phase shift.

$$\Delta\varphi_{TE} \approx \Delta\varphi_{TO-TE} + \Delta\varphi_{EO-c-TE} \quad (3.15)$$

$$\Delta\varphi_{TM} \approx \Delta\varphi_{TO-TM} - \Delta\varphi_{EO-c-TM} \quad (3.16)$$

In the case of a-axis grown, Pockels effect would produce a negative phase shift for both TE and TM polarization.

$$\Delta\varphi_{TE} \approx \Delta\varphi_{TO-TE} - \Delta\varphi_{EO-a-TE} \quad (3.17)$$

$$\Delta\varphi_{TM} \approx \Delta\varphi_{TO-TM} - \Delta\varphi_{EO-a-TM} \quad (3.18)$$

This difference is evidenced in the experimental results, obtaining a higher V_π for TM polarization. Furthermore, for this polarization, at low DC voltages some devices showed a small negative phase shift, which could be an indication of Pockels effect for c-axis grown BTO. In any case, to prove the presence of the Pockels effect, there is need to characterize the high speed performance of the MZM and ring resonators.

Finally, in order to find out the reason of the high current measured in all devices, different tests were carried out in the same run. Firstly, electrodes were deposited directly on the BTO layer. After running several measurement tests, it was not possible to obtain similar currents values as in the processed MZM.

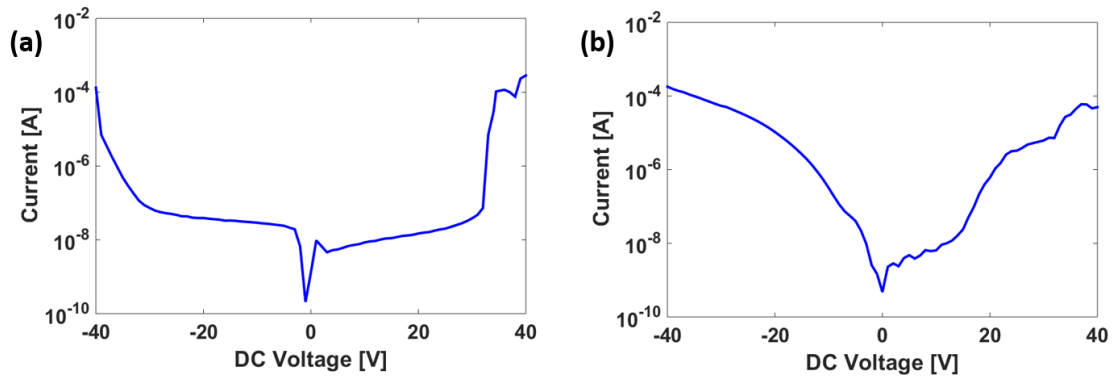


Figure 3.47: Current-Voltage behaviour for two tests. a) Sample without SiO₂ cladding and b) sample with SiO₂ cladding and lateral windows.

Current values lower than 1mA were detected when a voltage of 40V was applied (Figure 3.47(a)). Then, a piece of the same sample was covered with 500nm of SiO₂ cladding. Afterwards, lateral windows were opened and aluminium electrodes were placed directly on top of the BTO layer as in the original device to test if the high current measured was due to the electrode process. In this case, the obtained current values were of the same magnitude as in the previous test (Figure 3.47(b)), and again no high current

3.7. Electro-optical characterization

was measured as in the processed sample. It must be highlighted that in both cases, the highest measured current value was lower than 1mA even when applying around 40V. It must be pointed out that these studies were carried by placing the electrodes at the same distance as in the original sample. Unfortunately, these tests were not decisive to determine the origin of the high current measured. Therefore, the origin of the high current is not clear and might be connected with fabrication processes carried out in the original sample.

The summary of the EO behaviour at DC regime and the modulation efficiency of the devices in each sample is shown in Table 3.13.

	#INL1	#INL2	#INL3	#INL4	#INL5	#IBM1
BTO deposition technique	RF Sputtering					MBE
EO behaviour at DC regime	Linear phase shift variation Vs DC bias. Different slope and negative effective index variation for both positive and negatives voltages.	Linear phase shift variation Vs DC bias. Different slope and effective index variation for both positive and negatives voltages.	Linear phase shift variation Vs DC bias.	No EO behaviour.	Hysteresis behaviour in TE MZI.	Quadratic phase shift variation Vs DC bias. High current measured. Thermo-optic effect dominates at DC regime.
Modulation efficiency ($V_{\pi} \cdot L$)	1.05V·cm in a TE ring resonator. DE =3.6 μ m	21V·cm in a TE MZI. DE =3.6 μ m	4.2V·cm in a TE ring resonator. DE =3.6 μ m	--	3.6V·cm and 12.5V·cm in a TE and TM MZI. DE =2.5 μ m	

Table 3.13: Summary of the EO behaviour at DC regime and modulation efficiency of devices in all samples (DE=distance between electrodes).

3.7.2. RF regime

As before mentioned, the clear indication of Pockels effect would be the demonstration of high speed operation. For this purpose, we characterized at RF frequencies the devices which have shown an EO behaviour in DC regime. Once analogic modulation at high RF

frequencies is successfully demonstrated, we can introduce a sequence of bits in order to test the digital transmission capability.

3.7.2.1. Experimental set-ups

The method carried out to perform modulation measurements at RF frequencies consists in applying sinusoidal RF signals to the electrodes through high-speed ground-signal-ground (GSG) RF probes to modulate a continuous wave signal coming from a laser.

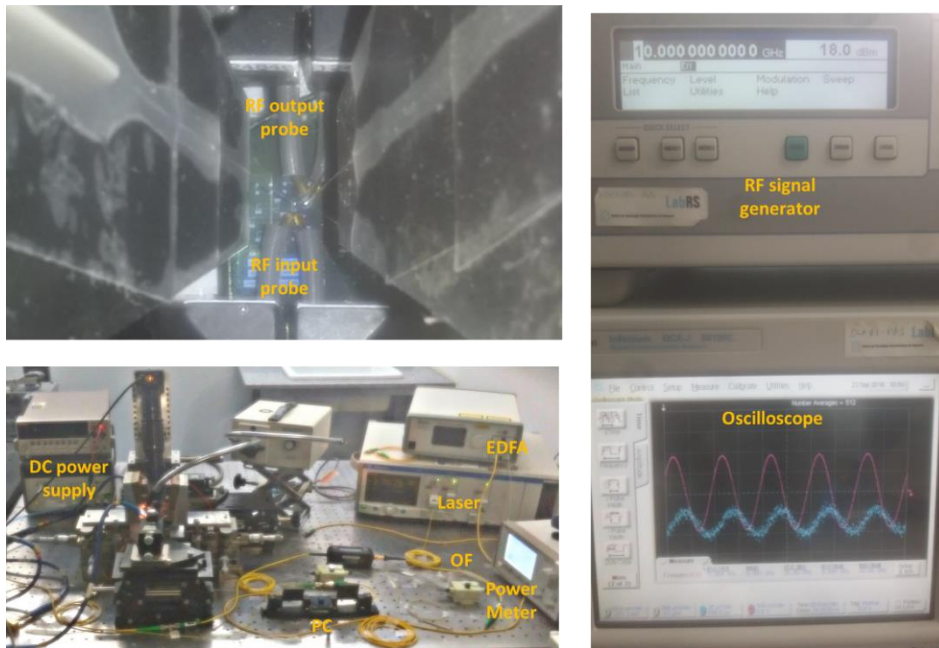
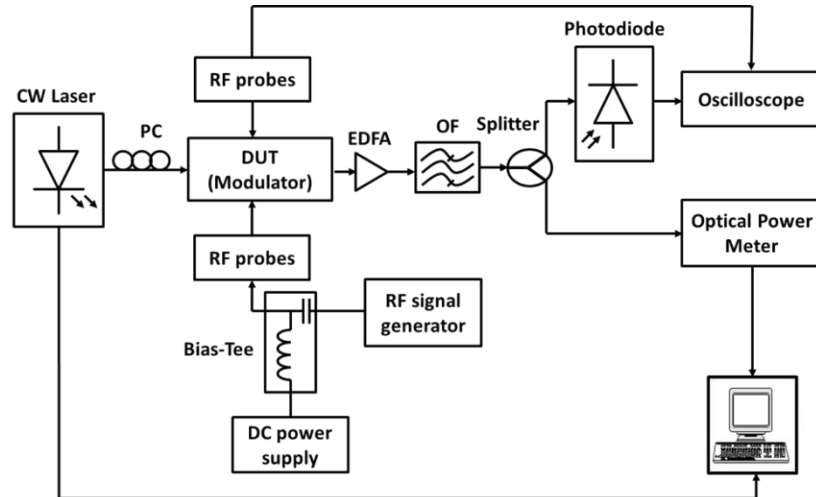


Figure 3.48: Schematic and figures of the characterization setup for the modulation at RF.

The output modulated optical signal is optically amplified by an erbium-doped fibre amplifier (EDFA) and then filtered via an optical filter (OF) to clean the noise introduced by the EDFA. Hence, both the modulating signal after the RF electrodes and the modulated signal after being photodetected are monitored by an oscilloscope. Before

3.7. Electro-optical characterization

being photodetected, the modulated signal is split to simultaneously monitor the photodetected temporal signal at the oscilloscope and the spectrum of the optical signal through the power meter to optimize the modulation performance at QB point. The experimental setup is shown in Figure 3.48.

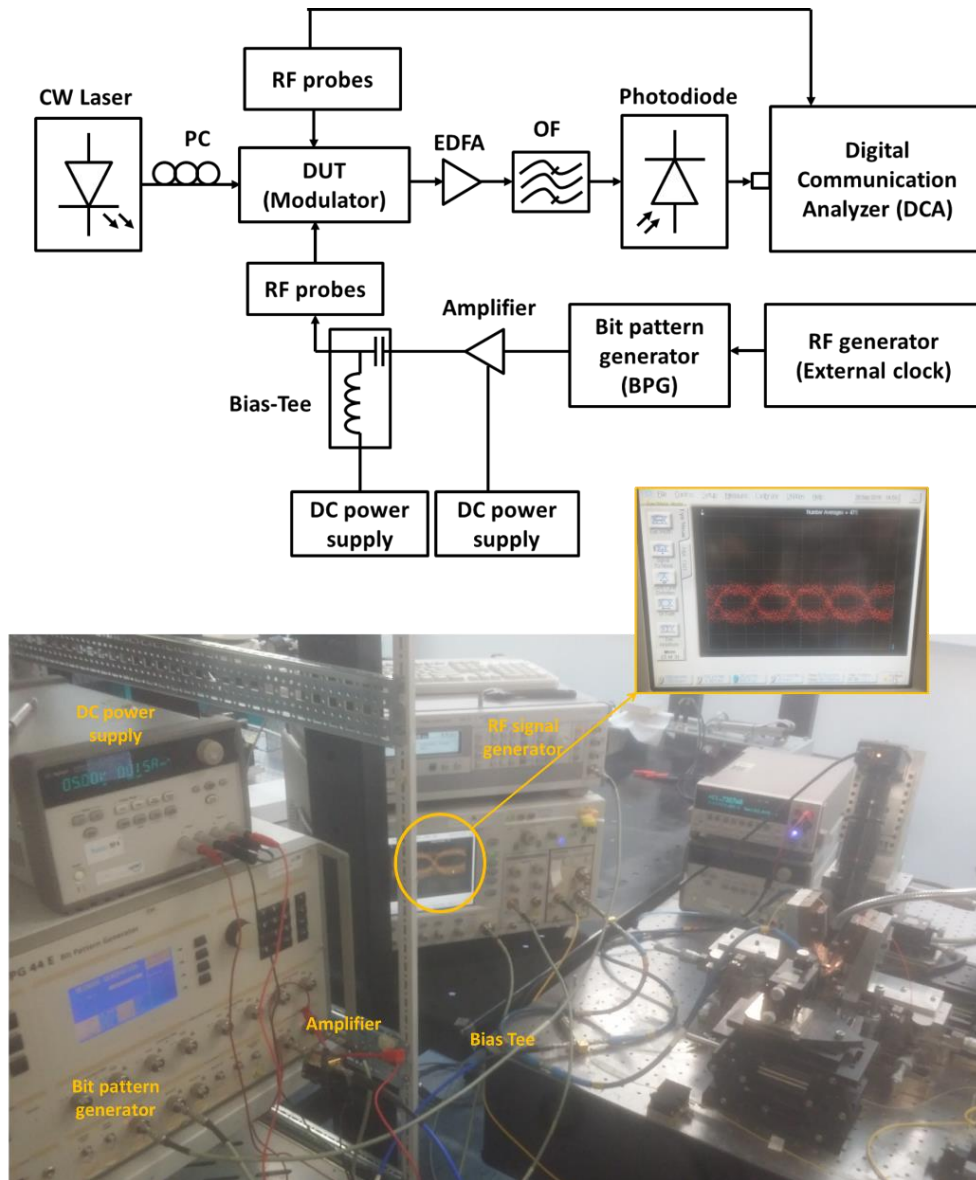


Figure 3.49: Schematic and figures of the characterization set-up for data transmission measurements.

To characterize the high speed data transmission capability, a non-return-to-zero (NRZ) pseudorandom bit sequence (PRBS) of length 2^7-1 delivered by a bit pattern generator (BPG) is applied, connected to an external clock. The input electrical signal is amplified through a high-speed RF amplifier to achieve the desired voltage swing and combined to DC bias voltage using a bias-Tee. The modulating signal is applied by high-speed GSG RF probes to the electrodes. The output modulated optical signal is then optically amplified by an EDFA, then filtered via an OF and finally photo-detected prior

to visualize the signal at the digital communication analyser (DCA). The experimental setup is shown in Figure 3.49.

3.7.2.2. RF electro-optic analogic results

RF sputtered BTO samples

In sample #INL1 a ring resonator was EO characterized. A low frequency signal was introduced into the modulator by using RF probes through lumped electrodes as above explained. In this way, we were able to observe modulation only up to 2MHz with a DC bias of 4V. Figure 3.50 shows the microscope image of the RF probes and optical fibers (Figure 3.50(a)) and the RF modulated signal at 100kHz (Figure 3.50(b)) and 2MHz (Figure 3.50(c)).

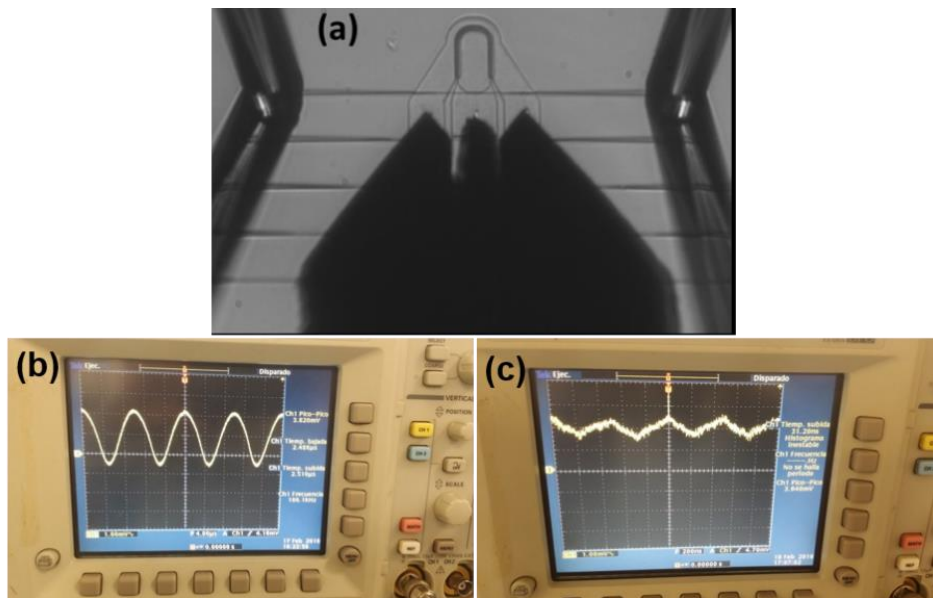


Figure 3.50: (a) Microscope image showing the RF probes and optical fibers, output modulated signal measured at (b) $f=100\text{kHz}$ and at (c) 2MHz .

Higher RF frequency operation was not possible. The main reason that was limiting the performance was probably the thin thickness of the metal electrodes (around 100nm) used in this sample, besides the large propagation losses.

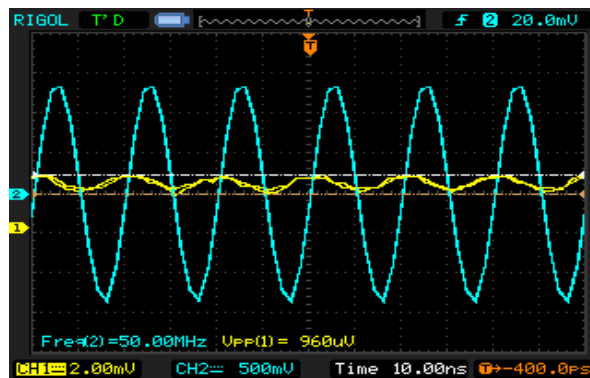


Figure 3.51: Output modulated signal measured at a frequency of 50MHz.

3.7. Electro-optical characterization

Therefore, in next samples the thickness of the aluminium electrodes was increased to 500nm. However, we were not able to experience modulation at RF frequencies until sample #INL5. In such sample we were able to demonstrate modulation up to 50MHz, as it can be see depicted in Figure 3.51. The blue line shows the input RF signal and the yellow one is the modulated signal.

Notwithstanding that the obtained modulation was significantly improved comparing to the first results, the RF performance was still low. Indeed, we identified the main reason of this unexpected low efficient modulation and probably the lack of modulation or low EO behaviour observed in last samples to be the poor crystallinity of the BTO layer. As it can be seen depicted in High Angle Annular Dark-Field (HAADF) pictures (Figure 3.52), important amorphous regions appeared in the BTO material. The reason of this amorphous areas could be connected with the STO layer that is previously grown on Si to overcome the mismatch between the lattice parameters of BTO and Si. In this way, the STO amorphization seemed to lead to amorphous columns in the BTO layer. Therefore, if the barium titanate is grown amorphous instead of crystalline, the material does not present Pockels coefficient in these regions. Hence, the fact that some parts of the material was amorphous strongly reduced the EO response in the MZI, or even eliminated the possible EO response of ring resonators due to its smaller length. Obviously, this fact is directly linked to the low EO behaviour obtained in devices of this and previous sample.

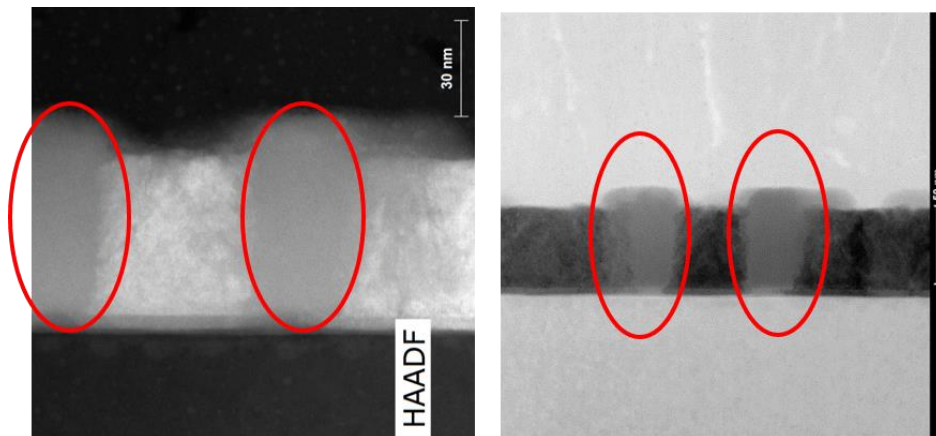


Figure 3.52: HAADF images highlighting the amorphous columns present in the BTO layer.

MBE BTO sample

In sample #IBM1 many devices presented EO behaviour when were EO characterized at DC regime. Therefore, we attempted to characterize them at RF frequencies. Following the measuring method described in section 3.7.2.1, we were able to observe EO modulation up to 30 GHz with an applied modulating signal of 5.6Vpp and a DC bias of 10V. Figure 3.53(a),(b) depict measured signals at 15GHz and 30GHz where the blue wave corresponded to the modulated signal and the pink wave to the modulating input RF signal. At higher frequencies, both electrical signals were attenuated due to electrode losses. Nonetheless, the demonstration of EO modulation at frequencies beyond 10 GHz

discards the presence of any other effect rather than Pockels as responsible of the modulation.

The influence of the DC bias voltage was also characterized to analyse the nature of the BTO ferroelectric orientation since, as previously discussed, the involved Pockels coefficients and hence the EO modulation performance depends on the BTO ferroelectric orientation. The amplitude of the modulated signal at 5GHz is depicted as a function of the DC applied bias in Figure 3.53(c) being the optical wavelength adjusted at each DC bias voltage to ensure modulation at the QB point. It must be highlighted here that the modulated signal should be rectified without applying a DC bias, i.e. at a DC voltage of 0V. However, this performance is not observed because an offset phase shift, which is thermo-optically generated by the RF signal, is always present. It is also interesting to point out from Figure 3.53(c) that a non-linear response is achieved when the DC bias increases, which would be linked to a c-axis crystallographic orientation of the BTO.

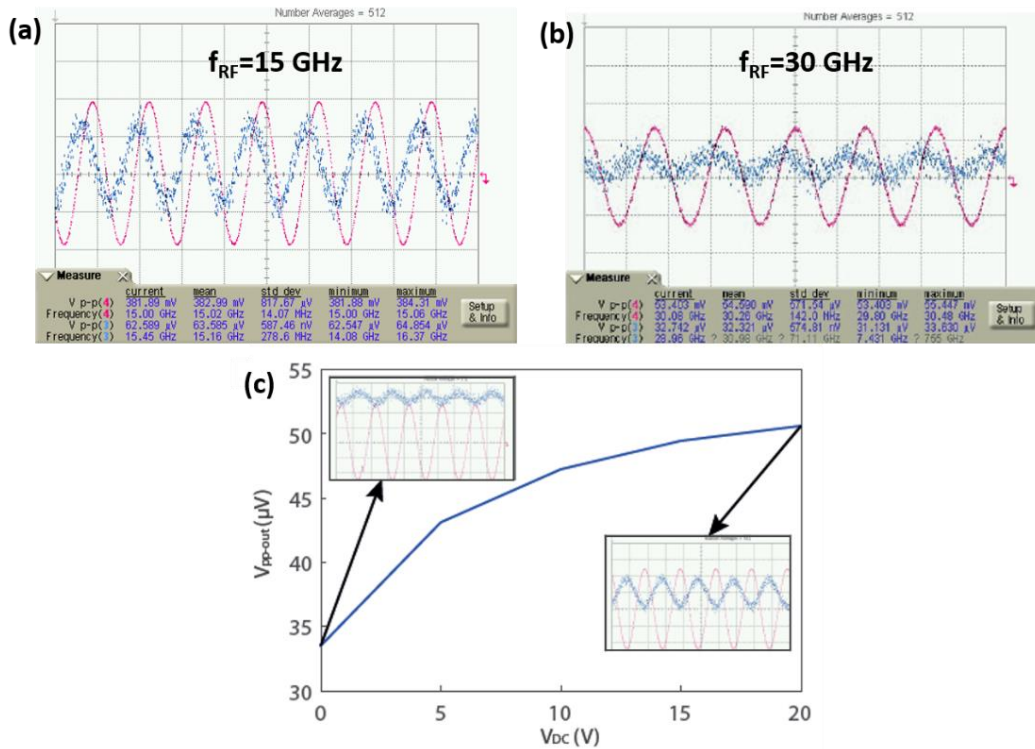


Figure 3.53: High-speed EO measurements. (a) Modulation response at 15GHz. (b) Modulation response at 30GHz. The blue wave corresponds to the photodetected EO modulated signal while the pink wave is the modulating signal measured at the output of the RF electrode. Results were obtained applying a DC bias of 10V and using an electrical amplification, being the RF voltage peak to peak of 5Vpp. (c) Peak to peak voltage of the photodetected EO modulated signal as a function of the applied DC bias for a RF signal of 5 GHz and without electrical amplification ($V_{RF}=3.3V_{pp}$).

3.7. Electro-optical characterization

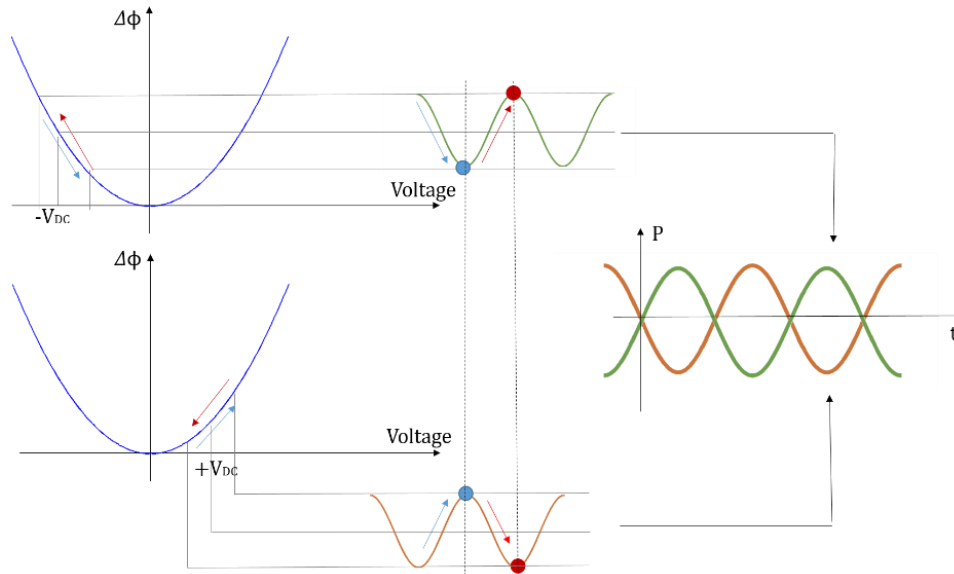


Figure 3.54: Schematic to explain the influence of the DC bias polarity on the EO modulation due to Pockels effect in c-axis grown BTO. The symmetry in the phase response implies that the modulated signals should be in counter phase for the same DC bias voltage but with different polarity.

On the other hand, Pockels modulation of c-axis grown BTO also implies that the modulated signals should be in counter phase for the same DC bias voltage but with different polarity, as schematically described in Figure 3.54. For this purpose, we measured the EO response of the MZM at 5GHz for DC bias voltages of +10V and -10V, as depicted in Figure 3.55. In fact, it can be seen how the modulated signals (blue waves) are in counter phase when the sign of the DC bias voltage is reversed. Hence, the obtained results are also in agreement with Pockels modulation in c-axis grown BTO.

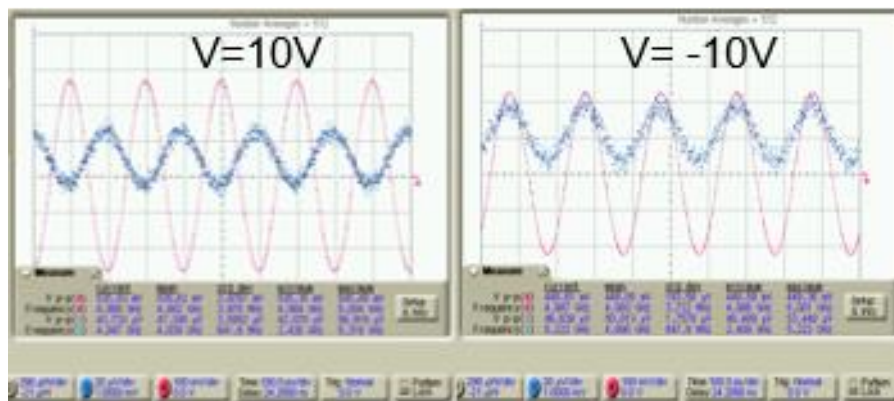


Figure 3.55: (a) Modulation response for a DC bias voltage of +10V. (b) Modulation response for a DC bias voltage of -10V. The RF frequency is 5 GHz and the applied peak to peak voltage is 3.3V.

Finally, out-of-plane and in-plane X-ray diffraction (XRD) scans on the fabricated sample were performed, confirming the prevailing c-axis orientation (Figure 3.56).

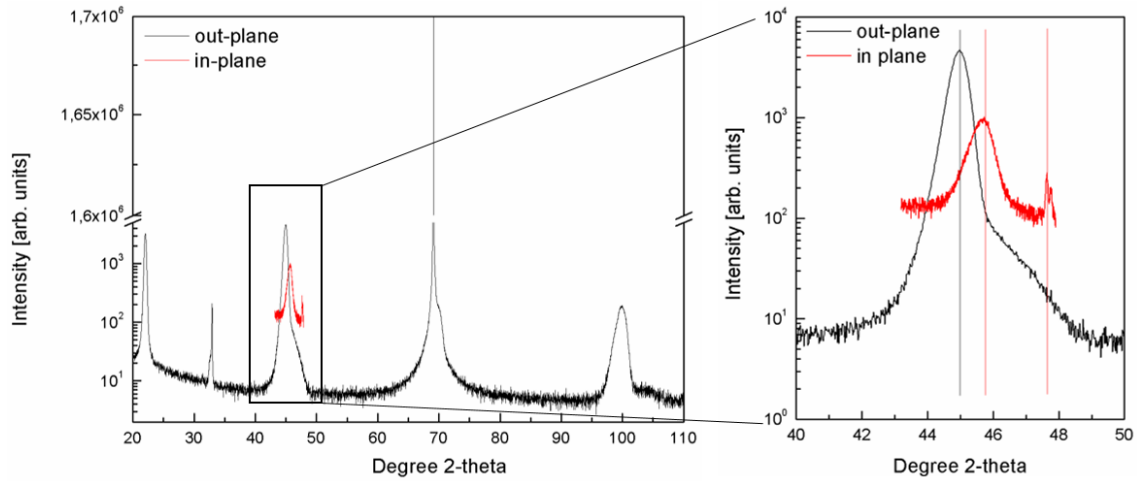


Figure 3.56: XRD pattern of the BTO film grown on SrTiO₃-SOI template by MBE for out-of-plane and in-plane measurements.

	#INL1	#INL2	#INL3	#INL4	#INL5	#IBM1
BTO deposition technique	RF Sputtering					MBE
Modulation results	2MHz	--	--	--	50MHz	30GHz

Table 3.14: Summary of the analogic modulation results of all samples.

3.7.2.3. RF electro-optic digital results

Once achieved modulation at high RF frequencies in sample #IBM1, we tested the data transmission capability of the modulator. The most useful figure of merit to experimentally evaluate the performance of a modulator in high speed digital transmissions is the eye diagram, in which the signal from the receiver is repetitively sampled and applied to the input of an oscilloscope while an external clock is used to trigger the horizontal sweep.

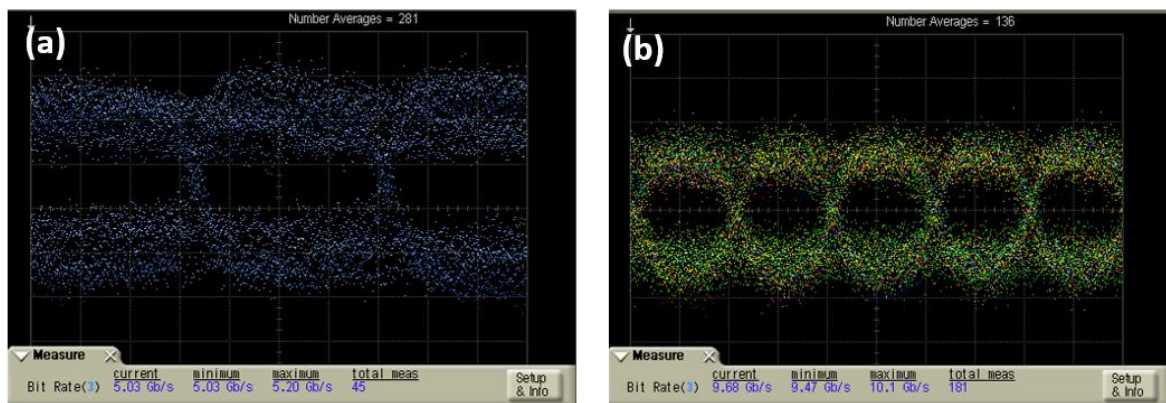


Figure 3.57: Eye diagrams at (a) 5Gbit/s and at (b) 10Gbit/s.

3.7. Electro-optical characterization

Figure 3.57 shows the obtained eye diagram for a bit rate of 5Gbit/s and 10Gbit/s. To the best of our knowledge, the highest digital data-rate transmission value reported for EO modulation in hybrid BTO on silicon devices was 300Mbit/s [49]. The obtained results in this thesis, showing EO modulation at 10Gbit/s, demonstrate the capability of high speed EO modulation in integrated BTO on silicon waveguide devices.

Chapter 4

Conclusions and future outlook

This thesis provides a contribution in the field of silicon photonics by integrating a novel material into silicon platform like barium titanate with high electro-optic coefficients.

Due to the ferroelectric nature of BaTiO₃, this material presents spontaneous polarization and it is formed by ferroelectric domains. In order to develop high efficiency electro-optic modulators based on BTO/Si we have firstly to thoroughly analyze the influence of the ferroelectric domain orientation on the EO performance. In this way, an exhaustive study of the EO performance has been carried out considering both single domain orientation and multi-domain orientation. In the former, the best EO performance has been achieved for a-axis oriented BaTiO₃ and TE polarization. In this case, the V_{π} voltage can be significantly improved by rotating the waveguide structure with respect to the principal axes of BaTiO₃. Hence, a V_{π} voltage as low as 1.35V has been obtained for a modulation length of 2mm, i.e. $V_{\pi} \cdot L = 0.27 \text{ V} \cdot \text{cm}$, at the optimum rotation angle of 55°. On the other hand, c-axis oriented BaTiO₃ allows achieving a high EO performance for both TE and TM polarizations though the phase shift variation with the applied voltage is no longer linear as it happens for a-axis oriented BaTiO₃. A V_{π} voltage of 4.25V has been achieved for TM polarization, which is slightly smaller than the value of 4.75V obtained for TE polarization.

However, a multi-domain structure is usually formed during the fabrication of thin-film BaTiO₃ layers. Therefore, the influence of a multi-domain a-axis structure on the electro-optic performance has also been analyzed in this work. Results have been obtained for a silicon CMOS compatible slot waveguide structure but the main findings can be generalized for any kind of optical waveguide structure. It has been shown that the angle of the optical waveguide with respect to the orientation of BTO domains is critical. More

concretely, the lowest V_π voltage is achieved by rotating the optical waveguide with an angle between 35° and 55° depending on the multi-domain structure. The most robust angle against variations in the domain structure is 45° but at the expenses of a slightly higher V_π voltage. In the proposed modulator, a percentage of antiparallel domains as high as 66% of the total number of domains present across the active length can be supported to keep the V_π voltage below 5V.

After the EO design, the fabrication and experimentally characterization of the proposed structures have been provided. Firstly, the a-Si deposition has been successfully demonstrated obtaining a refractive index close to the target as well as low propagation losses for both TE and TM polarization. After explaining the experimental set-up for passive characterization, the optical characterization of waveguides, ring resonators and MZI has been presented through the analyses of different samples with both RF sputtering and MBE growing methods of the BTO layer. Secondly, the experimental set-ups for DC and RF EO characterization have been introduced and hence the performance of the modulating devices in DC regime has been exposed. Significant differences between the performances of modulating devices in all samples have been obtained. Regarding to BTO fabricated by RF sputtering, although it has been demonstrated the characteristic butterfly shape that ferroelectric materials show, the poor EO behaviour at RF frequencies is directly linked to the amorphous regions that appeared in the BTO layer. With respect to the BTO sample grown by MBE, the DC performance was clearly dominated by the thermo-optic effect. Although the origin of the high current measured is not yet clear, we have been able to demonstrated EO modulation up to 30GHz. Furthermore, we obtained an eye diagram for a bit rate of 10Gbit/s. To the best of our knowledge, the highest digital data-rate transmission value reported for EO modulation in hybrid BTO on silicon devices has been 300Mbit/s [14]. Therefore, we have presented EO modulation at 10Gbit/s, demonstrating the capability of high speed EO modulation on integrated BTO/silicon waveguide devices.

In conclusion, we have demonstrated the direct integration of ferroelectric BTO thin films in the CMOS-compatible silicon photonics platform to achieve high speed EO modulation by means of linear Pockels effect. Therefore, the obtained experimental results confirm the potential impact of BTO material for developing high performance EO functionalities compatibles with the silicon platform, which could open new opportunities not only in the field of EO modulators but also in non-linear applications, quantum photonics or photonic sensors. Furthermore, in order to improve the efficiency of modulators based on BTO on silicon and therefore achieve higher data transmission capabilities, there is need to fully exploit Pockels effect and decrease optical losses by growing high quality layers of ferroelectric BTO material. It would also be interesting to control the orientation of the BTO towards obtaining purely a-axis or c-axis in order to align all domains in the same direction.

As possible direction for further research beyond this thesis, it would be interesting to investigate novel modulation techniques based on the induced change of the permittivity due to the change of thickness of the BTO layer by piezo-electric effect. Depending on

the configuration of the electrodes, this effect can have the same magnitude than the Pockels effect. Another important issue remains the demonstration of the non-volatility (bistability) effect of BTO in the silicon CMOS platform. The proposed BaTiO₃ offer a unique solution to bring the required advanced performance due to their ability to achieve an ultrafast electrically induced optical bistability and thus allowing the implementation of novel photonic devices such as optical memories or ultra-fast latching switching devices.

List of publications

JOURNAL PUBLICATIONS

- **Castera, P.**, Gutierrez, A. M., Tulli, D., Cueff, S., Orobtcchouk, R., Rojo, P., Saint-Girons, G., & Sanchis, P. (2016). Electro-Optical Modulation Based on Pockels Effect in BaTiO₃ with a Multi-Domain Structure. In IEEE Photonics Technology Letters (Vol. 28, No. 9, pp. 990-993). Institute of Electrical and Electronics Engineers (IEEE).
- **Castera, P.**, Tulli, D., Gutierrez, A. M., & Sanchis, P. (2015). Influence of BaTiO₃ ferroelectric orientation for electro-optic modulation on silicon. Optics express, 23(12), 15332-15342.
- **Castera, P.**, Gutierrez, A. M., Rosa, A., Tulli, D., Griol, A., Angelova, T., Bellieres, L., Hurtado, L., Eltes, F., Abel, S., Fompeyrine, J., & Sanchis, P. High speed electro-optic Mach-Zehnder modulator based on a hybrid BaTiO₃/Silicon waveguide structure. To be submitted.
- Rosa, A., Tulli, D., **Castera, P.**, Gutierrez, A. M., Griol, A., Baquero, M., Vilquin, B., Eltes, F., Abel, S., Fompeyrine, J., & Sanchis, P. Barium titanate (BaTiO₃) RF characterization for application in electro-optic modulators. Submitted.

CONFERENCE PUBLICATIONS

- **Castera, P.**, Rosa, A., Tulli, D., Gutierrez, A. M., Cueff, S., Orobtcchouk, R., Rojo, P., Saint-Girons, G., & Sanchis, P. (2016, August). Towards high-speed electro-optical performance in a hybrid BaTiO₃/Si Mach-Zehnder modulator. In Group

- IV Photonics (GFP), 2016 IEEE 13th International Conference in Sanghai (China), pp. 54-55. IEEE.
- Cueff, S., **Castera, P.**, Gutierrez, A. M., Romeo, P. R., Orobtcchouk, R., Wague, B Vilquin, B., Regreny, P., Rosa, A., Angelova, T., Griol, A., Sanchis, P. & Saint-Girons, G. (2016, July). Hybrid silicon-ferroelectric oxide platform for tunable nanophotonics on silicon. In Transparent Optical Networks (ICTON), 2016 18th International Conference in Trento (Italy), pp. 1-4. IEEE.
 - **Castera, P.**, Rosa, A., Gutierrez, A. M., Tulli, D., & Sanchis, P. (2016, June). Optimization of a hybrid BaTiO₃/Si Waveguide Structure for Electro-optic Modulation. 5th Spanish Nanophotonic Conference in Valencia (Spain).
 - **Castera, P.**, Gutierrez, A. M., Rosa, A., Tulli, D., & Sanchis, P. (2016, May). Optimization of a BaTiO₃ on Silicon Waveguide Structure for Electro-Optic Modulation. 18th European Conference on Integrated Optics in Warsaw (Poland).
 - **Castera, P.**, Tulli, D., Gutierrez, A. M., & Sanchis, P. (2015, August). Highly efficient BaTiO₃ on silicon electro-optic Mach-Zehnder modulator. In Group IV Photonics (GFP), 2015 IEEE 12th International Conference in Vancouver (Canada), pp. 102-103. IEEE.
 - Romeo, P. R., Hu, X., Cueff, S., Wague, B., Orobtcchouk, R., Vilquin, B., Grenet, G., Dubourdiu, C., Regreny, P., Saint-Girons, G., **Castera, P.**, Gutierrez, A. M., Sanchez, N., Angelova, T., Sanchis, P., Abel, S., & Fompeyrine, J. (2015, July). Integration of functional oxides on SOI for agile silicon photonics. In Transparent Optical Networks (ICTON), 2015 17th International Conference in Budapest (Hungary), pp. 1-4. IEEE.
 - Hu, X., Orobtcchouk, R., Cueff, S., Romeo, P. R., Regreny, P., Bachelet, R., Mazet, L., Louahadj, L., Moalla, R., Dubourdiu, C., Vilquin, B., Saint Girons, G., **Castera, P.**, Sanchez, N., Angelova, T., Griol, A., Gutierrez, A. M., & Sanchis, P. (2014, August). Slot waveguide electro-optic modulator with ferroelectric oxide BaTiO₃ on silicon. In Group IV Photonics (GFP), 2014 IEEE 11th International Conference in Paris (France), pp. 241-242. IEEE.
 - Sanchis, P., Sanchez, L., **Castera, P.**, Rosa, A., Gutierrez, A. M., Brimont, A., Saint-Girons, G., Orobtcchouk, R., Cueff, S., Rojo-Romeo, P., Bachelet, R., Regreny, P., Vilquin, B., Dubourdiu, C., Letartre, X., Grenet, G., Penuelas, J., Hu, X., Louahadj, L., Locquet, J. P., Zimmermann, L., Marchiori, C., Abel, S., Fompeyrine, J., & Hakansson, A. (2014, July). Silicon CMOS compatible transition metal dioxide technology for boosting highly integrated photonic

List of publications

devices with disruptive performance. In Transparent Optical Networks (ICTON), 2014 16th International Conference in Graz (Austria), pp. 1-4. IEEE.

OTHER PUBLICATIONS

- Deliverable D2.4: Final recipes for structures processing. Authors: Guillaume Saint-Girons, Mariela Menghini, Sébastien Cueff, Bertrand Vilquin, Regis Orobthchouk, Pedro Rojo-Romeo, Romain Bachelet, Philippe Regreny, Catherine Dubourdiou, Todora Angelova, Amadeu Griol, Juan Hurtado, **Pau Castera**, Alvaro Rosa, Ana Maria Gutierrez, Pablo Sanchis, Pia Homm, Bart van Bilzen, Jean Pierre Locquet, Stefan Abel, Jean Fompeyrine, Marilyne Sousa, Felix Eltes
- Deliverable D3.1: Developed BTO/Si based waveguiding structures. Authors: Guillaume Saint-Girons, Regis Orobthchouk, Pedro Rojo-Romeo, Sébastien Cueff, Ana María Gutierrez, **Pau Castera**, Nuria Sánchez, Teodora Angelova, Pablo Sanchis, Stefan Abel, Jean Fompeyrine, Chiara Marchiori.
- Deliverable D3.2: Characterization of the electro-optical BTO/Si performance on the chosen waveguide structure. Authors: Sébastien Cueff, Guillaume Saint-Girons, Bertrand Vilquin, Regis Orobthchouk, Pedro Rojo-Romeo, Romain Bachelet, Philippe Regreny, Ana Gutierrez, **Pau Castera**, Nuria Sánchez, Teodora Angelova, Nuria Sánchez, Amadeu Griol, Pablo Sanchis, Domenico Tulli, Stefan Abel, Jean Fompeyrine, Felix Eltes.
- Deliverable D3.3: Progress on development of novel electro-optical functionalities based on BTO/Si. Authors: Guillaume Saint-Girons, Regis Orobthchouk, Sébastien Cueff, Bertrand Vilquin, Pedro Rojo-Romeo, Romain Bachelet, Philippe Regreny, **Pau Castera**, Ana Maria Gutierrez, Pablo Sanchis, Stefan Abel, Jean Fompeyrine.
- Deliverable D3.4: Progress on the fabrication of the BTO/Si Mach-Zehnder modulator. Authors: Stefan Abel, Jean Fompeyrine, Sébastien Cueff, Guillaume Saint-Girons, Ana Maria Gutierrez, **Pau Castera**, Pablo Sanchis, Regis Orobthchouk, Bertrand Vilquin, Pedro Rojo-Romeo, Domenico Tulli.
- Deliverable D3.5: BTO/Si Mach-Zehnder modulator compliant to specifications. Authors: Stefan Abel, Johanna Nordlander, Felix Eltes, Jean Fompeyrine, Sébastien Cueff, Guillaume Saint-Girons, Ana Maria Gutierrez, **Pau Castera**, Alvaro Rosa, Pablo Sanchis, Regis Orobthchouk, Bertrand Vilquin, Pedro Rojo-Romeo, Domenico Tulli.

Bibliography

- [1] Technologies for Optical Interconnection: Challenges and Opportunities, Silicon Photonics Workshop: “Packaging and Test Challenges or Industrialization of Silicon Photonics”, Munich, 23 May 2011.
- [2] Hochberg, M., Harris, N. C., Ding, R., Zhang, Y., Novack, A., Xuan, Z., & Baehr-Jones, T. (2013). Silicon photonics: The next fabless semiconductor industry. *IEEE Solid-State Circuits Magazine*, 5(1), 48-58.
- [3] http://www.intel.com/pressroom/archive/releases/2010/20100727_comp_sm.htm
- [4] Lister, K. (2011). Luxtera delivers world’s first single chip 100Gbps integrated opto-electronic transceiver.
- [5] http://www.pecst.org/outline_en.html
- [6] Urino, Y., Noguchi, Y., Noguchi, M., Imai, M., Yamagishi, M., Saitou, S., & Arakawa, Y. (2012). Demonstration of 12.5-Gbps optical interconnects integrated with lasers, optical splitters, optical modulators and photodetectors on a single silicon substrate. *Optics express*, 20(26), B256-B263.
- [7] <http://www.helios-project.eu/>
- [8] Fang, A. W., Park, H., Cohen, O., Jones, R., Paniccia, M. J., & Bowers, J. E. (2006). Electrically pumped hybrid AlGaInAs-silicon evanescent laser. *Optics express*, 14(20), 9203-9210.
- [9] Bakir, B. B., Descos, A., Olivier, N., Bordel, D., Grosse, P., Augendre, E., Fullbert, L., & Fedeli, J. M. (2011). Electrically driven hybrid Si/III-V

- Fabry-Pérot lasers based on adiabatic mode transformers. *Optics express*, 19(11), 10317-10325.
- [10] Michel, J., Liu, J., & Kimerling, L. C. (2010). High-performance Ge-on-Si photodetectors. *Nature Photonics*, 4(8), 527-534.
- [11] Vivien, L., Polzer, A., Marris-Morini, D., Osmond, J., Hartmann, J. M., Crozat, P., Cassan, E., Kopp, C., Zimmermann, H., & Fédéli, J. M. (2012). Zero-bias 40Gbit/s germanium waveguide photodetector on silicon. *Optics express*, 20(2), 1096-1101.
- [12] Abel, S., Stöferle, T., Marchiori, C., Rossel, C., Rossell, M. D., Erni, R., Caimi, D., Sousa, M., Chelnokov, A., Offrein, B., & Fompeyrine, J. (2013). A strong electro-optically active lead-free ferroelectric integrated on silicon. *Nature communications*, 4, 1671.
- [13] Davis, C. (2014). *Lasers and Electro-optics: Fundamentals and Engineering*. Cambridge university press.
- [14] Campo, A. M. G. (2013). *Development of Integrated Silicon Photonics Modulation Devices for Digital and Analog Applications* (Doctoral dissertation, Universitat Politècnica de València).
- [15] Reed, G. T., Mashanovich, G., Gardes, F. Y., & Thomson, D. J. (2010). Silicon optical modulators. *Nature photonics*, 4(8), 518-526.
- [16] Barrios, C. A., & Lipson, M. (2004). Modeling and analysis of high-speed electro-optic modulation in high confinement silicon waveguides using metal-oxide-semiconductor configuration. *Journal of Applied Physics*, 96(11), 6008-6015.
- [17] Feng, N. N., Dong, P., Feng, D., Qian, W., Liang, H., Lee, D. C., Luff, J. B., Agarwal, A., Banwell, T., Menendez, R., Toliver, P., Woodward, T. K., & Asghari, M. (2010). Thermally-efficient reconfigurable narrowband RF-photonics filter. *Optics express*, 18(24), 24648-24653.
- [18] Soref, R., & Lorenzo, J. (1986). All-silicon active and passive guided-wave components for $\lambda = 1.3$ and $1.6 \mu\text{m}$. *IEEE Journal of Quantum Electronics*, 22(6), 873-879.
- [19] Soref, R., & Bennett, B. (1987). Electrooptical effects in silicon. *IEEE journal of quantum electronics*, 23(1), 123-129.
- [20] Jacobsen, R. S., Andersen, K. N., Borel, P. I., Fage-Pedersen, J., Frandsen, L. H., Hansen, Kristensen, M., Lavrinenko, A. V., Moulin, G., Ou, H.,

Bibliography

- Peucheret, C., Zsigri, B., & Bjarklev, A. (2006). Strained silicon as a new electro-optic material. *Nature*, 441(7090), 199-202.
- [21] Damas, P., Le Roux, X., Le Bourdais, D., Cassan, E., Marris-Morini, D., Izard, N., Maroutian, T., Lecoœur, P., & Vivien, L. (2014). Wavelength dependence of Pockels effect in strained silicon waveguides. *Optics express*, 22(18), 22095-22100.
- [22] Borghi, M., Mancinelli, M., Merget, F., Witzens, J., Bernard, M., Ghulinyan, M., Pucker, G., & Pavesi, L. (2015). High-frequency electro-optic measurement of strained silicon racetrack resonators. *Optics letters*, 40(22), 5287-5290.
- [23] Gao, Y., Huang, X., & Xu, X. (2014). Electro-optic modulator based on a photonic crystal slab with electro-optic polymer cladding. *Optics express*, 22(7), 8765-8778.
- [24] Alloatti, L., Korn, D., Palmer, R., Hillerkuss, D., Li, J., Barklund, A., Dinu, R., Wieland, J., Fournier, M., Fedeli, J., Yu, H., Bogaerts, W., Dumon, P., Baets, R., Koos, C., Freude, W., & Leuthold, J. (2011). 42.7 Gbit/s electro-optic modulator in silicon technology. *Optics express*, 19(12), 11841-11851.
- [25] Rabiei, P., Ma, J., Khan, S., Chiles, J., & Fathpour, S. (2013). Heterogeneous lithium niobate photonics on silicon substrates. *Optics express*, 21(21), 25573-25581.
- [26] Chen, L., Wood, M. G., & Reano, R. M. (2013). 12.5 pm/V hybrid silicon and lithium niobate optical microring resonator with integrated electrodes. *Optics express*, 21(22), 27003-27010.
- [27] Tanaka, T. (1954). Barium titanate ceramics and their applications. *Bull. Inst. Chem. Res. Kyoto Univ*, 32, 43-53.
- [28] Zgonik, M., Bernasconi, P., Duelli, M., Schlessler, R., Günter, P., Garrett, M. H., Rytz, D., Zhu, Y., & Wu, X. (1994). Dielectric, elastic, piezoelectric, electro-optic, and elasto-optic tensors of BaTiO₃ crystals. *Physical Review B*, 50(9), 5941.
- [29] Frey, M. H., Xu, Z., Han, P., & Payne, D. A. (1998). The role of interfaces on an apparent grain size effect on the dielectric properties for ferroelectric barium titanate ceramics. *Ferroelectrics*, 206(1), 337-353.

- [30] McNeal, M. P., Jang, S. J., & Newnham, R. E. (1998). The effect of grain and particle size on the microwave properties of barium titanate (BaTiO_3). *Journal of applied physics*, 83(6), 3288-3297.
- [31] Sreenivas, K., Mansingh, A., & Sayer, M. (1987). Structural and electrical properties of rf-sputtered amorphous barium titanate thin films. *Journal of Applied Physics*, 62(11), 4475-4481.
- [32] Dicken, M. J., Sweatlock, L. A., Pacifici, D., Lezec, H. J., Bhattacharya, K., & Atwater, H. A. (2008). Electrooptic modulation in thin film barium titanate plasmonic interferometers. *Nano letters*, 8(11), 4048-4052.
- [33] Takahashi, H., Numamoto, Y., Tani, J., & Tsurekawa, S. (2006). Piezoelectric properties of BaTiO_3 ceramics with high performance fabricated by microwave sintering. *Japanese journal of applied physics*, 45(9S), 7405.
- [34] Choi, K. J., Biegalski, M., Li, Y. L., Sharan, A., Schubert, J., Uecker, R., Reiche, P., Chen, Y. B., Pan, X. Q., Gopalan, V., Chen, L. Q., Schlom, D. G., Eom, C. B., & Chen, L. Q. (2004). Enhancement of ferroelectricity in strained BaTiO_3 thin films. *Science*, 306(5698), 1005-1009.
- [35] Wada, S., Suzuki, S., Noma, T., Suzuki, T., Osada, M., Kakihana, M., Park, S., Cross, L., & Shrout, T. R. (1999). Enhanced piezoelectric property of barium titanate single crystals with engineered domain configurations. *Japanese journal of applied physics*, 38(9S), 5505.
- [36] Panda, B., Dhar, A., Nigam, G. D., Bhattacharya, D., & Ray, S. K. (1998). Optical properties of RF sputtered strontium substituted barium titanate thin films. *Thin Solid Films*, 332(1), 46-49.
- [37] Cai, M. Q., Yin, Z., & Zhang, M. S. (2003). First-principles study of optical properties of barium titanate. *Applied physics letters*, 83(14), 2805-2807.
- [38] Cardona, M. (1965). Optical Properties and Band Structure of SrTiO_3 and BaTiO_3 . *Physical Review*, 140(2A), A651.
- [39] Wada, S., Yako, K., Kakemoto, H., Tsurumi, T., & Kiguchi, T. (2005). Enhanced piezoelectric properties of barium titanate single crystals with different engineered-domain sizes. *Journal of Applied Physics*, 98(1), 014109.

Bibliography

- [40] Yun, W. S., Urban, J. J., Gu, Q., & Park, H. (2002). Ferroelectric properties of individual barium titanate nanowires investigated by scanned probe microscopy. *Nano letters*, 2(5), 447-450.
- [41] Lei, Q., Dancer, C. E., Grovenor, C. R., & Grant, P. S. (2016). Preparation, microstructure and microwave dielectric properties of sprayed PFA/barium titanate composite films. *Composites Science and Technology*, 129, 198-204.
- [42] Damjanovic, D., Brem, F., & Setter, N. (2002). Crystal orientation dependence of the piezoelectric d_{33} coefficient in tetragonal BaTiO_3 as a function of temperature. *Applied physics letters*, 80(4), 652-654.
- [43] Valasek, J. (1921). Piezo-electric and allied phenomena in Rochelle salt. *Physical review*, 17(4), 475.
- [44] Haertling, G. H. (1999). Ferroelectric ceramics: history and technology. *Journal of the American Ceramic Society*, 82(4), 797-818.
- [45] Vijatović, M. M., Bobić, J. D., & Stojanović, B. D. (2008). History and challenges of barium titanate: Part II. *Science of Sintering*, 40(3), 235-244.
- [46] Dubourdieu, C., Bruley, J., Arruda, T. M., Posadas, A., Jordan-Sweet, J., Frank, M. M., Cartier, E., Frank, D. J., Kalinin, S. V., Demkov, A. A., & Narayanan, V. (2013). Switching of ferroelectric polarization in epitaxial BaTiO_3 films on silicon without a conducting bottom electrode. *Nature nanotechnology*, 8(10), 748-754.
- [47] Abel, S., Sousa, M., Rossel, C., Caimi, D., Rossell, M. D., Erni, R., Fompeyrine, J., & Marchiori, C. (2013). Controlling tetragonality and crystalline orientation in BaTiO_3 nano-layers grown on Si. *Nanotechnology*, 24(28), 285701.
- [48] Bernasconi, P., Zgonik, M., & Günter, P. (1995). Temperature dependence and dispersion of electro-optic and elasto-optic effect in perovskite crystals. *Journal of applied physics*, 78(4), 2651-2658.
- [49] Xiong, C., Pernice, W. H., Ngai, J. H., Reiner, J. W., Kumah, D., Walker, F. J., Ahn, C. H., & Tang, H. X. (2014). Active silicon integrated nanophotonics: ferroelectric BaTiO_3 devices. *Nano letters*, 14(3), 1419-1425.
- [50] Eltes, F., Caimi, D., Fallegger, F., Sousa, M., O'Connor, E., Rossell, M. D., Offrein, B., Fompeyrine, L., & Abel, S. (2016). Low-Loss BaTiO_3 -Si

- Waveguides for Nonlinear Integrated Photonics. *ACS Photonics*, 3(9), 1698-1703.
- [51] Pernice, W. H., Xiong, C., Walker, F. J., & Tang, H. X. (2014). Design of a silicon integrated electro-optic modulator using ferroelectric BaTiO₃ films. *IEEE Photonics Technology Letters*, 26(13), 1344-1347.
- [52] Hu, X., Cueff, S., Romeo, P. R., & Orobtcouk, R. (2015). Modeling the anisotropic electro-optic interaction in hybrid silicon-ferroelectric optical modulator. *Optics express*, 23(2), 1699-1714.
- [53] Castera, P., Tulli, D., Gutierrez, A. M., & Sanchis, P. (2015). Influence of BaTiO₃ ferroelectric orientation for electro-optic modulation on silicon. *Optics express*, 23(12), 15332-15342.
- [54] Abel, S., Stöferle, T., Marchiori, C., Caimi, D., Czornomaz, L., Stuckelberger, M., Sousa, M., Offrein, B., & Fompeyrine, J. (2016). A hybrid barium titanate–silicon photonics platform for ultraefficient electro-optic tuning. *Journal of Lightwave Technology*, 34(8), 1688-1693.
- [55] Castera, P., Gutierrez, A. M., Tulli, D., Cueff, S., Orobtcouk, R., Rojo, P., Saint-Girons, G., & Sanchis, P. (2016, May). Electro-Optical Modulation Based on Pockels Effect in BaTiO₃ with a Multi-Domain Structure. In *IEEE Photonics Technology Letters* (Vol. 28, No. 9, pp. 990-993). Institute of Electrical and Electronics Engineers (IEEE).
- [56] Abel, S., Stöferle, T., Marchiori, C., Caimi, D., Czornomaz, L., Rossel, C., & Fompeyrine, J. (2013, July). Electro-optical active barium titanate thin films in silicon photonics devices. In *Integrated Photonics Research, Silicon and Nanophotonics* (pp. IW4A-5). Optical Society of America.
- [57] Petraru, A., Schubert, J., Schmid, M., & Buchal, C. (2002). Ferroelectric BaTiO₃ thin-film optical waveguide modulators. *Applied Physics Letters*, 81(8), 1375-1377.
- [58] Li, J., Liu, Z., Tu, Y., Ho, S. T., Jung, I. W., Ocola, L. E., & Wessels, B. W. (2013). Photonic crystal waveguide electro-optic modulator with a wide bandwidth. *Journal of Lightwave Technology*, 31(10), 1601-1607.
- [59] Sun, D., Zhang, J., Chen, C., Kong, M., Wang, J., & Jiang, H. (2015). Theoretical feasibility demonstration for over 100 GHz electro-optic modulators with c-axis grown BaTiO₃ crystal thin-films. *Journal of Lightwave Technology*, 33(10), 1937-1947.

Bibliography

- [60] Girouard, P., Liu, Z., Chen, P., Jeong, Y. K., Tu, Y., Ho, S. T., & Wessels, B. W. (2016). Enhancement of the pockels effect in photonic crystal modulators through slow light. *Optics Letters*, 41(23), 5531-5534.
- [61] Tang, J., Yang, S., & Bhatranand, A. (2007, May). Strain induced waveguide electro-optic modulators in Barium Titanate crystal. In *Photonic Applications Systems Technologies Conference* (p. JTUA36). Optical Society of America.
- [62] Tang, P., Meier, A. L., Towner, D. J., & Wessels, B. W. (2005). BaTiO₃ thin-film waveguide modulator with a low voltage-length product at near-infrared wavelengths of 0.98 and 1.55 μm . *Optics letters*, 30(3), 254-256.
- [63] Tang, P., Towner, D. J., Hamano, T., Meier, A. L., & Wessels, B. W. (2004). Electrooptic modulation up to 40 GHz in a barium titanate thin film waveguide modulator. *Optics express*, 12(24), 5962-5967.
- [64] Liu, Z., Lin, P. T., Wessels, B. W., Yi, F., & Ho, S. T. (2007). Nonlinear photonic crystal waveguide structures based on barium titanate thin films and their optical properties. *Applied physics letters*, 90(20), 201104.
- [65] Lin, P. T., Yi, F., Ho, S. T., & Wessels, B. W. (2009). Two-dimensional ferroelectric photonic crystal waveguides: simulation, fabrication, and optical characterization. *Journal of Lightwave Technology*, 27(19), 4330-4337.
- [66] Dicken, M. J., Sweatlock, L. A., Pacifici, D., Lezec, H. J., Bhattacharya, K., & Atwater, H. A. (2008). Electrooptic modulation in thin film barium titanate plasmonic interferometers. *Nano letters*, 8(11), 4048-4052.
- [67] Wessels, B. W. (2007). Ferroelectric epitaxial thin films for integrated optics. *Annu. Rev. Mater. Res.*, 37, 659-679.
- [68] Gu, X., Lubyshev, D., Batzel, J., Fastenau, J. M., Liu, W. K., Pelzel, R., Magana, J. F., Ma, Q., Wang, L. P., Zhang, P., & Rao, V. R. (2009). Commercial molecular beam epitaxy production of high quality Sr Ti O 3 on large diameter Si substrates. *Journal of Vacuum Science & Technology B: Microelectronics and Nanometer Structures Processing, Measurement, and Phenomena*, 27(3), 1195-1199.
- [69] Abel, S., Stöferle, T., Marchiori, C., Caimi, D., Czornomaz, L., Rossell, M. D., Erni, R., Sousa, M., Siegart, H., Offrein, B., & Fompeyrine, J. (2015, September). Barium-titanate integrated with silicon photonics for ultra-efficient electro-optical performance. In *Optical Communication (ECOC), 2015 European Conference on* (pp. 1-3). IEEE.

- [70] Almeida, V. R., Xu, Q., Barrios, C. A., & Lipson, M. (2004). Guiding and confining light in void nanostructure. *Optics letters*, 29(11), 1209-1211.
- [71] Sanchis, P., Blasco, J., Martínez, A., & Martí, J. (2007). Design of silicon-based slot waveguide configurations for optimum nonlinear performance. *Journal of Lightwave Technology*, 25(5), 1298-1305.
- [72] COMSOL MULTIPHYSICS™.
- [73] Alferness, R. C. (1982). Waveguide electrooptic modulators. *IEEE Transactions on Microwave Theory Techniques*, 30, 1121-1137.
- [74] Sung, S. Y. (2008). Integrating magneto-optical garnet isolators on semiconductor substrates. ProQuest.
- [75] Depla, D., Mahieu, S., & Greene, J. (2010). Sputter deposition processes. In *Handbook of deposition technologies for films and coatings: science, applications and technology* (pp. 253-296). William Andrew.
- [76] Rabe, K. M., Ahn, C. H., & Triscone, J. M. (Eds.). (2007). *Physics of ferroelectrics: a modern perspective* (Vol. 105). Springer Science & Business Media.
- [77] Abel, S. (2014). *Electro-optic photonic devices based on epitaxial barium titanate thin films on silicon* (Doctoral dissertation, Université Grenoble Alpes).
- [78] Davey, J. E., & Pankey, T. (1968). Epitaxial GaAs films deposited by vacuum evaporation. *Journal of Applied Physics*, 39(4), 1941-1948.
- [79] <http://www.explainthatstuff.com/molecular-beam-epitaxy-introduction.html>
- [80] Selvaraja, S. K., Sleenckx, E., Schaekers, M., Bogaerts, W., Van Thourhout, D., Dumon, P., & Baets, R. (2009). Low-loss amorphous silicon-on-insulator technology for photonic integrated circuitry. *Optics Communications*, 282(9), 1767-1770.
- [81] Okamura, Y., Yoshinaka, S., & Yamamoto, S. (1983). Measuring mode propagation losses of integrated optical waveguides: a simple method. *Applied Optics*, 22(23), 3892-3894.
- [82] Hayashi, T., Oji, N., & Maiwa, H. (1994). Film thickness dependence of dielectric properties of BaTiO₃ thin films prepared by sol-gel method. *Japanese journal of applied physics*, 33(9S), 5277.

Bibliography

- [83] Hamano, T., Towner, D. J., & Wessels, B. W. (2003). Relative dielectric constant of epitaxial BaTiO₃ thin films in the GHz frequency range. *Applied physics letters*, 83(25), 5274-5276.
- [84] Stückelberger, M., Shah, A., Krc, J., Despeisse, M., Meillaud, F., & Ballif, C. (2010, June). Internal electric field and fill factor of amorphous silicon solar cells. In *Photovoltaic Specialists Conference (PVSC), 2010 35th IEEE* (pp. 001569-001574).

